

**PROGRAMA DE PÓS-GRADUAÇÃO EM
ENGENHARIA ELÉTRICA**

Improved Power Losses Calculation Model for Air Core Reactors

Henrique Borges Zaninelli

**Itajubá
September
2021**

**UNIVERSIDADE FEDERAL DE ITAJUBÁ
PROGRAMA DE PÓS-GRADUAÇÃO EM
ENGENHARIA ELÉTRICA**

Henrique Borges Zaninelli

Improved Power Losses Calculation Model for Air Core Reactors

**A Dissertation Presented to the Itajubá
Federal University in Fulfillment of
Requirements for the Degree of Master of
Science in Electric Engineering.**

Concentration Area: Power Systems

**Supervisor: Edson da Costa Bortoni
Co-Supervisor:**

**Itajubá
September
2021**

DEDICATION

This work is a small token dedicated to my mother Nilce, that in her entire life has shown me and taught me the real meaning of unconditional love, to my father Ataídes, who arts in heaven, which has been my professional inspiration since the beginning. If this day was anyhow possible, it was mostly because of them.

To my beloved Patricia, the giant woman who walks beside me, upholding me, teaching me, being the most candid and lovely person I have had the pleasure to meet.

To my brothers and sisters by choice which I have known for many years and for whom I nurture a very profound love.

To my brother Milton who has received the call to join the creator and that during his life was the most humble and lovely person.

To Daniel, my good friend and former manager, who summoned me to be a researcher and developer, basically changing my life upside down and now he watches over me from a higher ground, besides my father and my brother.

To Mario Fabiano, our good friend and oracle which always welcomes me with a pleasing, friendly and wise word.

Thanks to all of you that even not knowing have contributed to my personal growth, providing the most incredible moments of happiness, friendship, and love.

ACKNOWLEDGEMENTS

I would like to acknowledge the support received from GE Renewable Energy staff and management that supported the development of this work, specially to my friend the engineering manager Mr. Marcelo Moraes who has always been an enthusiastic of this project.

I would like to express my sincere gratitude to my supervisor, professor Dr. Edson da Costa Bortoni for his constructive supervision, proper direction, support, and patience.

I am thankful to Mr. Bruno Fonseca, GE's laboratory supervisor, and his staff that played an important role in the proper conduction of the prototype testing that was key to guide the results of this work.

I thank the great dedication of the operators that built the prototypes, with a special thanks to Kevin William that was always an unconditional "hands on" supporter of the project.

I acknowledge the great partnership from my colleagues Mr. Felipe Andrade and Mr. Hugo Facó on the development of this project.

I would like to deeply thank my parents, girlfriend and friends who constantly push me to take up challenges and keep moving ahead.

Finally, I sincerely acknowledge CAPES, CNPq, FAPEMIG and INERGE for their continuous support to conduct research.

ABSTRACT

Air core reactors (ACR) have been widely used in power systems in several different applications like harmonic filters, thyristor-controlled reactors (TCR) for static var compensators (SVC), mechanically switched reactors (MSR) for shunt compensation of long transmission lines, smoothing and valve reactors for line commutated converter (LCC) and for voltage sourced converted (VSC), respectively, in HVDC systems, onshore and offshore. As a global trend, the pursuit of environmentally friendly equipment has increased, leveraging the use of ACRs in ultra-high voltage (UHV) systems. Applying that equipment in such voltage levels demands very accurate calculation models to establish the proper design parameters (e.g., inductance values, power losses and audible noise levels) as well as the stresses (dielectric, thermal and mechanical) that the equipment will have to withstand during operation, for their lifecycle. One typical concern related to those calculation models is regarding the prediction of the eddy current winding losses by analytical models. Several models have been proposed for this type of calculation for transformers and electrical machines, but usually with some constraints that make those models more suitable to that equipment than to others. With the crescent demand for ACR with lower power losses levels, it makes sense to look for improvements on those calculation models. One way of supporting the enhancement of those models is using software based on finite element methods (FEM) that allows for very detailed simulation of the physical phenomena related to the air core reactors and their applications. Although the FEM is a powerful tool for complex simulations, it is usually very time consuming and may require sophisticated computational apparatus to run more complex models. Air core reactors are equipment composed by one or several concentric windings made of conductive material (aluminum or copper) and their design may vary significantly, from a few kilograms to some dozens of tons. The simulation, in a reasonable time, of that equipment with several windings and sometimes thousands of turns would require computers that are not easily found in regular industries. In this work an optimized modeling process for simulating ACR using a 2-D equivalent geometry method in a finite element-based software was developed to allow for faster simulations. The validation of the method is performed by running a full factorial design of experiments (DOE), screening four design parameters of windings: winding diameter, winding height, number of strands and strand diameter, as these parameters significantly affect the two main design characteristics of the air core reactors: inductance and winding power losses. The results of the finite element simulations are statistically compared to the results of analytical calculations. With the deployment of this process, an improvement for the calculation of the eddy current winding losses of that equipment is proposed.

Index terms – Air Core Reactors, Design of Experiments, Finite Element Analysis, Response Surface Method.

LIST OF FIGURES

Figure 1.1- Evolution of voltage and power levels for transformers. Source: [1].....	14
Figure 1.2 - Dry-type air core reactor construction. Source: [2].....	15
Figure 2.1 - Representation of a single layer winding. Source [16].....	21
Figure 2.2 - Representation of two infinitesimally thin coaxial windings. Source [21].....	23
Figure 2.3 - Circuit example for inductance calculation.....	26
Figure 2.4 - Skin effect example.....	28
Figure 2.5 - Skin effect in a single wire for DC, 50 Hz and 10 kHz currents - ANSYS® Maxwell.....	29
Figure 2.6 - Proximity effect between two conductors.....	29
Figure 2.7 – Proximity and Skin effect in two wires for DC, 50 Hz and 10 kHz currents - ANSYS® Maxwell.....	30
Figure 2.8 - Representation of a multi-layer winding. Source [27].....	31
Figure 2.9 - Representation of ACR with three windings, split into ten sections.....	32
Figure 2.10 - Representation of interturn (v) and interlayer (h) distances.....	36
Figure 2.11 - Current distribution for a 19 strands cable at high frequency.....	36
Figure 2.12 - Impedance matrix solving process - ANSYS® Maxwell.....	39
Figure 3.1 - Impacting factors on ACR design.....	42
Figure 3.2 - Design parameters and their screening levels.....	43
Figure 3.3 - 2-D representation of one turn of a FTC.....	45
Figure 3.4 - 2-D representation of a winding with 10 turns of FTC.....	46
Figure 3.5 - Simulation with finite element method flowchart.....	46
Figure 3.6 - Parallel current representation per turn.....	47
Figure 3.7 - Initial meshing for strand by stand simulation.....	47
Figure 3.8 - Equivalent geometry for a 2D turn and external setup.....	48
Figure 3.9 - Equivalent geometry for a 2-D winding with 10 turns and external setup.....	48
Figure 3.10 - Inductance variation between FEM and analytical model.....	50
Figure 3.11 - Boundary conditions setups example – ACR1.....	50
Figure 3.12 - Magnetic field distribution in space and internally to the winding – ACR79.....	51
Figure 3.13 - Winding power losses percent deviation - FEA x Analytical - ACR1.....	54
Figure 3.14 - Winding power losses percent deviation - FEA x Analytical - ACR13.....	54
Figure 3.15 - Winding power losses percent deviation - FEA x Analytical - ACR25.....	54
Figure 3.16 - Winding power losses percent deviation - FEA x Analytical - ACR28.....	55
Figure 3.17 - Winding power losses percent deviation - FEA x Analytical - ACR40.....	55
Figure 3.18 - Winding power losses percent deviation - FEA x Analytical - ACR52.....	55
Figure 3.19 - Winding power losses percent deviation - FEA x Analytical - ACR55.....	56

Figure 3.20 - Winding power losses percent deviation - FEA x Analytical - ACR67.....	56
Figure 3.21 - Winding power losses percent deviation - FEA x Analytical - ACR79.....	56
Figure 3.22 - Postprocessing panel of the Eddy Current Solver - ANSYS® Maxwell.....	57
Figure 3.23 - Fields calculator in the Eddy Current Solver - ANSYS® Maxwell.....	58
Figure 3.24 - Winding power losses percent deviation - FEA Corrected and FEA - ACR1.....	59
Figure 3.25 - Winding power losses percent deviation - FEA Corrected and FEA - ACR13.....	59
Figure 3.26 - Winding power losses percent deviation - FEA Corrected and FEA - ACR25.....	59
Figure 3.27 - Winding power losses percent deviation - FEA Corrected and FEA - ACR28.....	60
Figure 3.28 - Winding power losses percent deviation - FEA Corrected and FEA - ACR40.....	60
Figure 3.29 - Winding power losses percent deviation - FEA Corrected and FEA - ACR52.....	60
Figure 3.30 - Winding power losses percent deviation - FEA Corrected and FEA - ACR55.....	61
Figure 3.31 - Winding power losses percent deviation - FEA Corrected and FEA - ACR67.....	61
Figure 3.32 - Winding power losses percent deviation - FEA Corrected and FEA - ACR79.....	61
Figure 3.33 - Winding proximity effect losses - FEA Corrected x Analytical - ACR1.....	62
Figure 3.34 - Winding proximity effect losses - FEA Corrected x Analytical - ACR13.....	62
Figure 3.35 - Winding proximity effect losses - FEA Corrected x Analytical - ACR25.....	63
Figure 3.36 - Winding proximity effect losses - FEA Corrected x Analytical - ACR28.....	63
Figure 3.37 - Winding proximity effect losses - FEA Corrected x Analytical - ACR40.....	63
Figure 3.38 - Winding proximity effect losses - FEA Corrected x Analytical - ACR52.....	64
Figure 3.39 - Winding proximity effect losses - FEA Corrected x Analytical - ACR55.....	64
Figure 3.40 - Winding proximity effect losses - FEA Corrected x Analytical - ACR67.....	64
Figure 3.41 - Winding proximity effect losses - FEA Corrected x Analytical - ACR79.....	65
Figure 3.42 - Run chart losses - proximity effect - FEA corrected x Analytical model.....	67
Figure 3.43 - Pareto chart of the impact of the changes in the experiments.....	68
Figure 3.44 - Effect of the change of the main design characteristics on the model accuracy.....	68
Figure 3.45 - Two-way interactions - Design parameters changes effects on the model accuracy.....	69
Figure 3.46 - Magnetic field distribution - ACR1.....	70
Figure 3.47 - Magnetic field distribution - ACR55.....	70
Figure 3.48 - Response surface - Proximity effect losses x Hw, Dav.....	72
Figure 3.49 - Response surface - Proximity effect losses x Nstr, Dav.....	72
Figure 3.50 - Response surface - Proximity effect losses x Dstr, Dav.....	72
Figure 3.51 - Response surface - Proximity effect losses x Nstr, Hw.....	73
Figure 3.52 - Response surface - Proximity effect losses x Dstr, Hw.....	73
Figure 3.53 - Response surface - Proximity effect losses x Dstr, Nstr.....	73
Figure 3.54 - Run chart losses - proximity effect - Analytical Corrected x Analytical model.....	75
Figure 3.55 - Winding proximity effect losses - FEA Corrected x Analytical Corrected - ACR1.....	76
Figure 3.56 - Winding proximity effect losses - FEA Corrected x Analytical Corrected - ACR13.....	76

Figure 3.57 - Winding proximity effect losses - FEA Corrected x Analytical Corrected - ACR25.	76
Figure 3.58 - Winding proximity effect losses - FEA Corrected x Analytical Corrected - ACR28.	77
Figure 3.59 - Winding proximity effect losses - FEA Corrected x Analytical Corrected - ACR40.	77
Figure 3.60 - Winding proximity effect losses - FEA Corrected x Analytical Corrected - ACR52.	77
Figure 3.61 - Winding proximity effect losses - FEA Corrected x Analytical Corrected - ACR55.	78
Figure 3.62 - Winding proximity effect losses - FEA Corrected x Analytical Corrected - ACR67.	78
Figure 3.63 - Winding proximity effect losses - FEA Corrected x Analytical Corrected - ACR79.	78
Figure 3.64 - Winding power losses percent deviation before and after correction - ACR1.	79
Figure 3.65 - Winding power losses percent deviation before and after correction - ACR13.	79
Figure 3.66 - Winding power losses percent deviation before and after correction - ACR25.	80
Figure 3.67 - Winding power losses percent deviation before and after correction - ACR28.	80
Figure 3.68 - Winding power losses percent deviation before and after correction - ACR40.	80
Figure 3.69 - Winding power losses percent deviation before and after correction - ACR52.	81
Figure 3.70 - Winding power losses percent deviation before and after correction - ACR55.	81
Figure 3.71 - Winding power losses percent deviation before and after correction - ACR67.	81
Figure 3.72 - Winding power losses percent deviation before and after correction - ACR79.	82
Figure 3.73 - Capability analysis for inductance calculation using FEM.	84
Figure 3.74 - Before/after process capability comparison for winding total losses.	85

LIST OF TABLES

Table 2.1 - Full factorial representation of a two level, two factors DOE.	41
Table 3.1 - Experiments nomenclature and their design parameters levels.	44
Table 3.2 - Inductance deviation between FEM and analytical model.	49
Table 3.3 - DC losses percent deviation between FEM and analytical model.	52
Table 3.4 - Proximity effect losses percent deviation between FEA corrected and analytical model. ..	66
Table 3.5 - Fits and residuals for the response surface equation.	74
Table 3.6 - Total corrected winding power losses percent deviations.	83

LIST OF ACRONYMS

2-D	Two-dimensional
3-D	Three-dimensional
AC	Alternating Current
ACR	Air Core Reactor
AWG	American Wire Gauge
CTQ	Critical to Quality
DOE	Design of Experiments
DC	Direct Current
EMF	Electromotive Force
FEA	Finite Element Analysis
FEM	Finite Element Method
FTC	Flat Transposed Cable
HVDC	High Voltage Direct Current
LCC	Line Commutate Converter
LSL	Lower Spec Limit
MSR	Mechanically Switched Reactor
MSE	Minimum Square Error
RSM	Response Surface Method
SVC	Static Var Compensation
TCR	Thyristor Controlled Reactor
UHV	Ultra-High Voltage
USL	Upper Spec Limit
VSC	Voltage Sourced Converter

LIST OF SYMBOLS

L	Self-inductance
M	Mutual inductance
a_1	Average radius for winding 1 in Maxwell's equation
a_2	Average radius for winding 2 in Maxwell's equation
D	Distance between windings in Maxwell's equation
A	Average diameter of the winding for Wheeler's equation
B	Axial length of the winding for Wheeler's equation
C	Radial length of the winding for Wheeler's equation
N	Number of turns of the winding
D_{av}	Average diameter of the winding
H_w	Height of the winding
N_{str}	Number of strands
D_{str}	Diameter of the strands
k_{str}	Stranding factor
i_t	Total winding current
B	Magnetic field intensity
P-value	Level of marginal significance within a statistical hypothesis test
σ	Electrical conductivity of a conductor
ρ	Electrical resistivity of a conductor
μ_0	Magnetic permeability in vacuum
μ_r	Relative magnetic permeability
α	Ratio between winding height and winding average diameter
R_{dc}	Resistance at direct current
R_{skin}	Increased AC resistance due to skin effect
δ	Magnetic field penetration depth (skin depth)
th_n	Radial thickness of the n^{th} winding
ω	Angular frequency
f	Frequency
N_{sec}	Number of sections of a winding for losses calculation
P_{str}	Conductor total losses per unit length

A_{sec}	Cross-sectional area of a conductor
T	Period of the current waveform
P_s	Conductor skin effect losses per unit length
P_p	Proximity effect losses per unit length of a conductor
I_{str}	Peak value of the current flowing in a conductor
H_r	Magnetic field strength in radial direction
H_z	Magnetic field strength in axial direction
L	Length of a conductor
P_{dc}	Total winding DC losses
P_{skin}	Total winding losses including skin effect
$H_{j,r}$	Magnetic field strength in the section “ j ” in radial direction
$H_{j,z}$	Magnetic field strength in the section “ j ” in axial direction
n_j	Number of turns in a section “ j ”
$P_{\text{prox},j}$	Winding losses due to proximity effect in a section “ j ”
P_{prox}	Total winding losses due to proximity effect
d	Number of significant figures used in computations
J	Current density in a conductor
J^*	Current density conjugate
m	Number of levels of a variable
k	Factors (variables) that affect a CTQ
N_{exp}	Number of experiments of a full factorial DOE

SUMMARY

PROGRAMA DE PÓS-GRADUAÇÃO EM ENGENHARIA ELÉTRICA	1
DEDICATION	2
ACKNOWLEDGEMENTS	3
ABSTRACT	4
LIST OF FIGURES.....	5
LIST OF TABLES.....	8
LIST OF ACRONYMS.....	9
LIST OF SYMBOLS.....	10
SUMMARY	12
1. INTRODUCTION	14
1.1 Objective	18
1.2 Dissertation Outline	19
2. LITERATURE REVIEW	20
2.1 Inductance	20
2.1.1. Analytical model – Bartky’s Transformation	23
a) Mutual inductance	23
b) Self-Inductance.....	25
2.1.2. FEM for Inductance	25
a) Inductance from flux linkage.....	26
b) Inductance from energy in the magnetic field.....	27
2.2 Eddy current losses	28
2.2.1. Analytical model	37
a) DC losses	38
b) Skin effect	38
c) Proximity effect.....	38
2.2.2. Finite Element Model	39
a) DC losses	40

b) Skin and proximity effects	40
2.2.3. Design of experiments.....	40
2.2.4. Response Surface Method	41
3. METHODOLOGY	42
3.1 Design parameters for DOE.....	42
3.2 FEM with the 2-D equivalent geometry method.....	45
3.3 Comparison of inductance values.....	49
3.4 FEA of eddy current winding losses.....	51
3.5 Comparison between analytical and finite element models	65
3.6 Application of the response surface method.....	71
3.7 Analysis of total corrected power losses	74
4. CONCLUSIONS.....	86
4.1 Inductance evaluation.....	84
4.2 Winding power losses evaluation.....	85
5. FUTURE WORKS	87
6. BIBLIOGRAPHY.....	88

1. INTRODUCTION

The concept of inductors was part of the discovery process of the transformer principles. In 1831, Michael Faraday demonstrated the principle of electromagnetic induction, generating a voltage pulse in a secondary coil when a direct current flowing in a primary coil was interrupted. In 1832, Joseph Henry discovered the concept of self-inductance, as a rapid change in the flux induced a high voltage in the coil. However, the first commercial application of the “induction coil” is only dated of 1886, when Georges Westinghouse improved the former designs into one that would connect to AC networks, could handle high power and would be manufacturable, taking the benefit of the early discovery of Lucien Gaulard and John Dixon Gibbs that proposed the use of the iron core to link a primary to a secondary coil. In the following decades, the very high demand for power boosted the increase of the network voltage levels, therefore there were 800 kV networks in developing stage already in 1960 in North America and Venezuela. It is said that one of the drivers of this development was the improvement on the transformer technologies. The evolution along the decades of the transformers voltage and power levels can be seen in Fig. 1.1. Along this road, the transformer production technology was also applied to manufacture inductors (reactors) for applications like current limiting and neutral earthing, shunt compensation of long transmission lines and smoothing for HVDC systems.

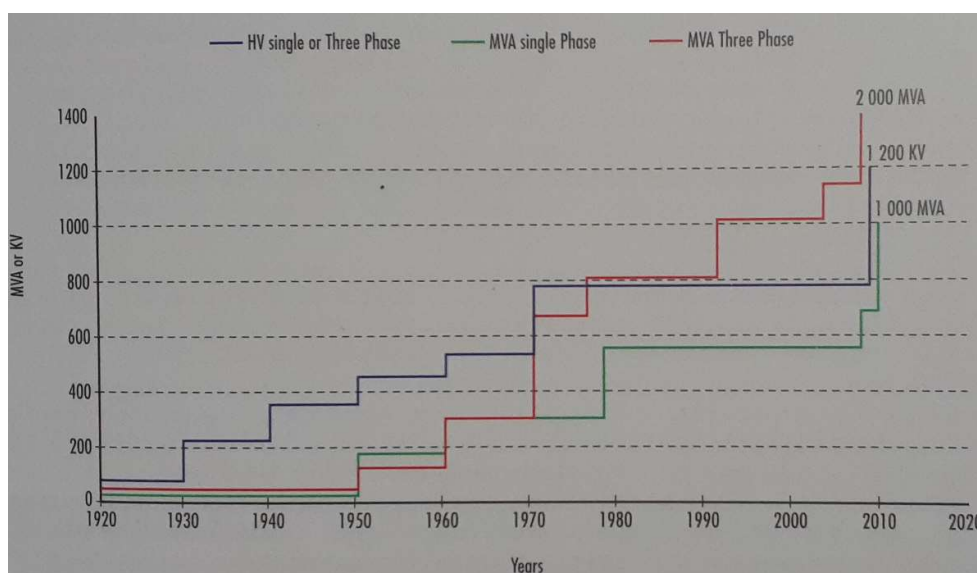


Figure 1.1- Evolution of voltage and power levels for transformers. Source: [1]

It was also in the end of the 20th century that the construction of the so called dry-type air core reactor (ACR) was conceived, being a bunch of concentric windings encapsulated in epoxy-impregnated resin, with no secondary winding and no magnetic core, as seen in Fig. 1.2.

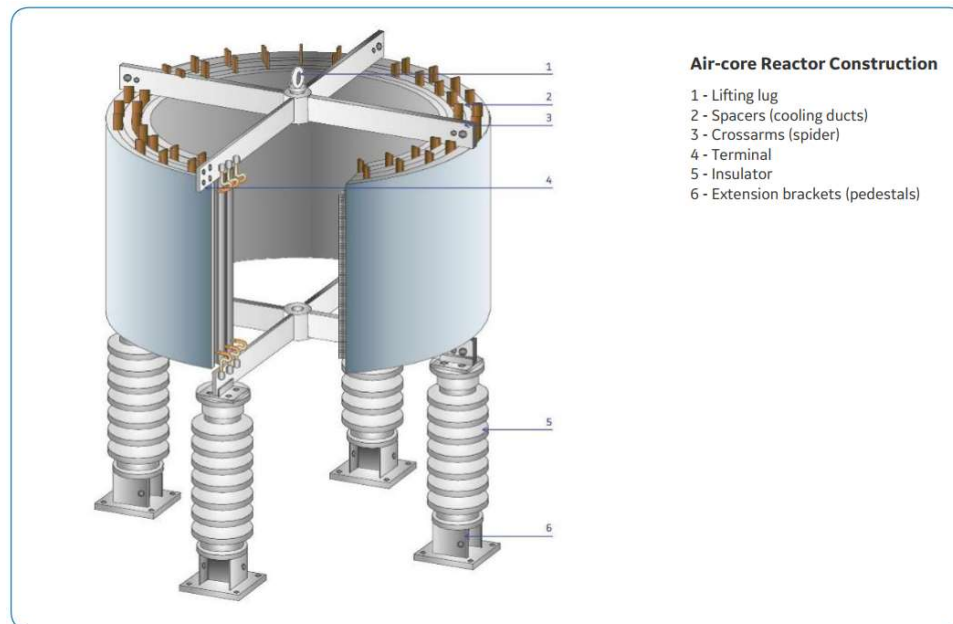


Figure 1.2 - Dry-type air core reactor construction. Source: [2]

By its construction concept, the ACRs have the benefit of linear characteristics as they are not saturable once there is no magnetic core. They have no oil insulation system, present no fire hazard concerns and are considered maintenance free. For those, among other reasons, they became the most common design deployed in applications [2, 4] which require power inductors, such as:

- Arc-furnace reactors: connected in series to provide power factor correction and limitation for currents and voltages.
- Current-limiting reactors: series connected reactors designed to reduce short-circuit current to levels that can be handled by equipment installed downstream in the electrical system.
- Damping reactors: applied to limit inrush and outrush currents during switching operations of capacitor banks.
- Discharge reactors: used in series compensation systems to limit the discharge current of the capacitors.
- Harmonic filter reactors: deployed along with power capacitors and resistors to reduce harmonic content generated by non-linear components and loads in the power systems.

- Load-flow control reactors: applied in series in transmission lines to control the load-flow by changing the line impedance characteristic.
- Motor starting reactors: connected in series with motors to limit the inrush currents.
- Neutral-earthing reactors: used to limit fault current during phase-to-ground short-circuit of three-phase networks, being connected between the neutral point of the network and the ground.
- Shunt reactors: connected in parallel to the systems, used to compensate for the capacitive reactive power of loaded transmission lines or underground cables.
- Smoothing and valve reactors: connected in series in the HVDC system, their purpose is to reduce harmonic currents in the DC system, reduce the current increase rate during fault conditions and improve the system stability.
- Thyristor-Controlled Reactor (TCR): applied in SVCs to support dynamic voltage stabilization, improve synchronous stability, and operate as steady-state voltage support.

The construction of the ACR has been evolving along the years, also driven by the crescent need for higher power transmission which requires higher levels of reactive power compensation, for example. The first encapsulated construction was mainly composed by windings made of single aluminum wires insulated with plastic films. With the increasing demand for power, the need for lower levels of power losses became more evident, promoting the use of stranded cables in the construction of the ACR. In the last two decades, aiming to minimize the power losses levels, the manufacturers of ACRs started using the concept of the completely transposed flat cables (FTC), being able to reduce the size of the equipment, still reaching high reactive power levels with lower levels of power losses.

In the first decades of existence of the ACRs their most common applications in power systems were small current limiting, harmonic filters, neutral grounding, TCRs and shunt compensation in networks with voltage levels up to 34.5 kV. As the manufacturing processes evolved, the manufacturers were able to produce bigger windings and with the deployment of new technologies it was also possible to reduce their size, comparing to past designs. That improvement allowed the ACRs to be presented as a cost-effective solution, raising the interest of the utilities on changing the former design of the reactors, made similarly to the transformers, to the dry-type air core version. That interest has provided the means to the evolution of not only the manufacturing processes but also the design calculation methods of the air core reactors, so today they can be installed in series in 800 kV networks and in shunt connection up to 500 kV networks. In 2020 the first 420 kV shunt compensation project, considering only the

air core solution for the reactors, was started in Germany.

Applying this type of equipment in UHV networks demands very accurate calculation models to establish the proper design characteristics like inductance, power losses and temperature. The proper calculation of power losses, specifically the eddy current winding losses, has been subject of several studies due to their importance and as a general analytical solution is difficult to be found considering the complexity of the distribution of the magnetic field among the windings, turns and strands of several different designs.

Studies like [5, 7], presenting the Dowell's method and [8, 10] presenting the Ferreira's method has been widely used as references for studies of losses calculation for round wires exposed to external uniform magnetic fields. However, there are not many conclusive studies related to the application of flat transposed cables in air core reactors and the simple use of the above mentioned methods on the calculation of the eddy current winding losses, for those cables, has provided results that need to be improved. Therefore, the focus of this work is on the calculation of the eddy current winding losses of air core reactors that deploy the FTC on its construction.

The study is conducted as a full factorial design of experiments [12], screening four main design parameters of the windings, winding diameter, winding height, number of strands and strand diameter, in three levels. The ACRs are modeled and simulated using ANSYS® Maxwell [13] Eddy Current solver, applying a 2-D equivalent geometry. With such a geometry equivalency there is no need of representing each strand of the many turns of the windings, therefore faster and simpler simulations can be performed. Considering this approach, the ACRs design characteristics, inductance, and eddy current winding losses, can be statistically compared to the analytical calculation and based on the results, a correction formula to the later can be provided by applying the response surface method [12].

1.1 Objective

The main objective of this dissertation is to propose an improvement for the calculation method of the winding power losses related to air core reactors by exploring the distribution of the magnetic field with the use of FEM and a 2-D equivalent geometry that makes this kind of analysis a lot faster than the usual complete simulation strand-by-strand 2-D FEM.

1.2 Dissertation Outline

This work is presented in five chapters. The first is an introduction of the history of inductors, the applications of air core reactors in power systems and the main concerns related to their design and application in UHV networks. The second is the literature review comprising the analytical calculation of inductances and power losses, FEM, design of experiments and response surface method. The third is the methodology applied in this work, which is summarized below:

- Definition of main design parameters that affect the winding power losses and set up of full factorial DOE.
- Simulation of the FEMs with the 2-D equivalent geometry method.
- Comparison between the analytical model and FEM for inductance calculation.
- Simulation of eddy current winding losses using FEM, screening the frequency up to 10 kHz.
- Comparison between the analytical model and FEM for eddy current winding losses calculation.
- Application of the response surface method.
- Comparison between the analytical model, corrected by the response surface method and the FEM for total power losses.

The fourth is the conclusion of this dissertation, where the results are analyzed and safety margins for the calculation of the winding power losses are proposed for ACRs with one cylinder.

The last brings the suggestions for future works and samples of studies already started.

2. LITERATURE REVIEW

The characteristics of the air core reactors analyzed in this study are mainly their total inductance (self and mutual) and total winding power losses. Hence the analytical calculation models of those characteristics are detailed in this chapter. The finite element method used to simulate those characteristics with the support of the FEA software are also explained here. Explanation about the statistical approach related to the design of experiments and the response surface method are presented in this chapter as well.

2.1 Inductance

Inductance can be understood as the capacity of a component to create counter EMF in opposition to changing magnetic fluxes. Its unit, H (Henry), is named after the American scientist Joseph Henry who discovered the principle of electromagnetic induction in 1832. The calculation of this parameter in windings has been subject of several studies due to the relevance in electrical applications like electrical machines, transformers, and inductors in general. Some of those studies are commented in this section as they are very often mentioned as references for the subject. One common particularity highlighted by the authors about the methods is the fact that most of the formulas, otherwise stated, are related to inductance calculation for low frequencies. Early studies provided formulas for which the solution involves elliptic integrals of all three kinds, that even if expanded in series their solution, would be very time consuming for the computers available at the time. In that sense, the first work to be commented as a very important reference is the formulae for the mutual inductance of coaxial circles given by Maxwell [13] in 1881.

$$M = 4\pi\sqrt{a_1a_2} \left[\left(\frac{2}{k} - k \right) F - \frac{2}{k} E \right] \quad (2.1)$$

where,

$$k = \frac{2\sqrt{a_1a_2}}{\sqrt{(a_1 + a_2)^2 + d^2}} = \sin \gamma \quad (2.2)$$

F and E are the complete elliptic integrals of first and second kind. That formula is applicable to coaxial circles of any size at any distance apart, except when the radii are nearly equal and are very close to each other. Cohen *et* Kirchhoff [14], in 1907, presented the calculation of the inductances of two symmetrically placed coaxial single layer solenoids with high accuracy, however requiring a great deal of work to solve the integrals. Nagaoka *et* Olshausen [15], in 1912, adapted the expressions provided in [14] so they can be computationally implementable. In 1916, Rosa [16] published a set of analysis of the previously published formulae for the calculation of mutual and self-inductances, separating the methods who provided reliable and consistent results from those who presented some intrinsic errors along the tests. Up to that point, the tradeoff had been between having very robust methods aiming for high accuracy, but being very time consuming as a counterpart, and solving the elliptic integrals using specific series that are simpler, but with the accuracy limited to their range of convergence. One good example of those simple and fast calculations is the one provided by Wheeler [17] in 1928, shown in the Equations 2.3 and 2.4, with the dimensions in millimeters as provided in Fig. 2.1

$$L = \frac{25.4 a^2 n^2}{9a + 10b} \quad (2.3)$$

$$L = \frac{a^2 n^2}{9a + 10b} \quad (2.4)$$

where a is the height of the winding, b is the average diameter of the winding, c is the thickness of the winding and n is the number of turns of the winding. Equation 2.3 provides better accuracy when $b > a$ and Equation 2.4 would present more accurate results when $a > b > 0.2a$.

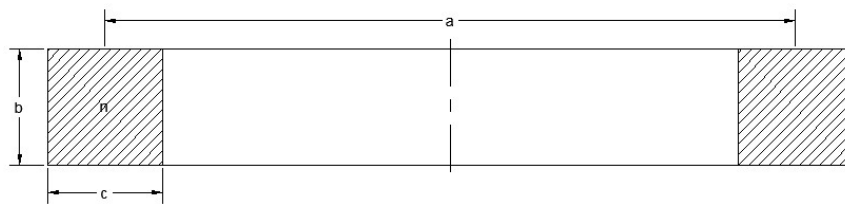


Figure 2.1 - Representation of a single layer winding. Source [16]

Considering that a single formula would not converge for all the possible pair of windings and the choice among the many available formulae would not be simple due to the number of parameters involved in the analysis, Grover [18], published in 1933, a set of tables that would allow for faster calculations of the mutual inductance for any two coaxial solenoids, used in conjunction with a single formula, providing good accuracy for almost all the types of applications, except for those who require very refined measurements. For single layer windings a practical approach was provided by Foelsch [19] as he provided a correction factor based on constant inductances with a graphic representation related to the height and average diameter of the windings. The work of Dwight [20], in 1945, provided context to the calculation of the reactance of different structures like tubular busbars and the air windings with different types of conductors (rectangular, round, and stranded). In 1946, Grover [21] contributed with the work that would become one of the most important references for the calculation of self and mutual inductances of inductors, covering scenarios like of non-coaxial non-concentric windings and windings with different types of conductors. Those two important contributions [20, 21] are well mentioned in subsequent studies about the subject as they provided substantial background with several tests and proper guidance on how to apply the many different formulas available on the proper type of inductor, so the best results in terms accuracy and applicability could be achieved. Later, in 1978, Fawzi *et* Burke [22] would publish the algorithm to the calculation of inductances, based on the Bartky's transformation, being applicable to all winding sizes, with different shapes and variable degrees of coupling, yet efficient and providing very high accuracy. This method is better detailed in the section 2.1.1 and is used as the base calculation for the purpose of this work.

2.1.1. Analytical model – Bartky's Transformation [22]

The calculation for the mutual inductance is presented first, as the one for the self-inductance would be a particular case of that. The terms of the formulas in this section are related to the dimensions represented in Fig. 2.2.

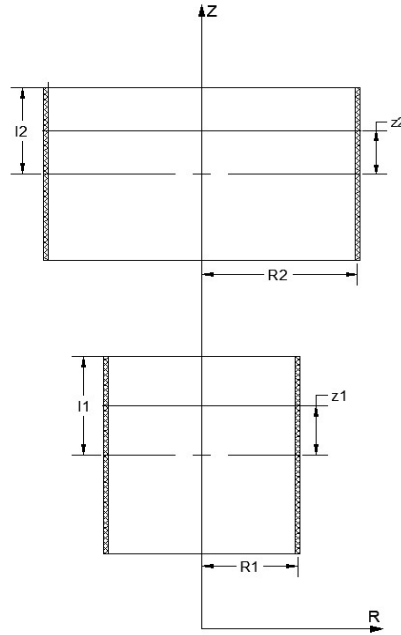


Figure 2.2 - Representation of two infinitely thin coaxial windings. Source [21]

a) Mutual inductance

The mutual inductance of two coaxial infinitely thin windings, concentric or not, can be calculated by the Equation 2.5.

$$M = \mu_0 n_1 n_2 \int_{z_2=s-l_2}^{s+l_2} \int_{z_1=-l_1}^{l_1} \int_{\varphi=0}^{\pi} \frac{R_1 R_2 \cos \varphi d\varphi}{\sqrt{R_1^2 + R_2^2 + (z_1 - z_2)^2 - 2R_1 R_2 \cos \varphi}} dz_1 dz_2 \quad (2.5)$$

Integrating by parts regarding φ , z_1 and z_2 , respectively, the Equation 2.6 is obtained.

$$M = 2\pi\mu_0 (R_1 R_2)^{3/2} n_1 n_2 [C_i(R_1, R_2, z_1) - C_i(R_1, R_2, z_2) + C_i(R_1, R_2, z_3) - C_i(R_1, R_2, z_4)] \quad (2.6)$$

Where C_i is the function defined as per Equation 2.7.

$$C_i(R_1, R_2, z) = \frac{\sqrt{R_1 R_2}}{2\pi} \int_0^{\pi} \frac{\sqrt{R_1^2 + R_2^2 + z^2 - 2R_1 R_2 \cos \varphi}}{R_1^2 + R_2^2 - 2R_1 R_2 \cos \varphi} \sin^2 \varphi d\varphi \quad (2.7)$$

and,

$$\begin{aligned}
z_1 &= l_1 + l_2 + s \\
z_2 &= l_1 - l_2 + s \\
z_3 &= -l_1 - l_2 + s \\
z_4 &= -l_1 + l_2 + s
\end{aligned}$$

The main difficulty of the implementation of the algorithm itself is the solution of the integral of the Equation 2.7. This problem is solved by the successive application of the Bartky's transformation to reduce the integrand to a constant.

$$C_i(R_1, R_2, z) = \frac{2}{\pi} \int_0^{\pi/2} \left(A' \sin^2 \theta + B' \cos^2 \theta + C \frac{\sin^2 \theta}{q^2 \cos^2 \theta + \sin^2 \theta} \right) \frac{1}{\sqrt{k^2 \cos^2 \theta + \sin^2 \theta}} \sin^2 \theta d\theta \quad (2.8)$$

where,

$$\theta = \frac{\varphi}{2} \quad (2.9)$$

$$q = \frac{R_1 - R_2}{R_1 + R_2} \quad 0 < |q| < 1 \quad (2.10)$$

$$k^2 = \frac{(R_1 - R_2)^2 + z^2}{(R_1 + R_2)^2 + z^2} \quad 0 < k^2 < 1 \quad (2.11)$$

$$\gamma = \frac{z^2}{4R_1R_2} \quad (2.12)$$

$$A = \sqrt{1 - k^2} \left[-\gamma + \frac{1}{3(1 - k^2)} \right] \quad (2.13)$$

$$B = -\frac{k^2}{3\sqrt{1 - k^2}} \quad (2.14)$$

$$C = \gamma\sqrt{1 - k^2} \quad (2.15)$$

Some special cases of the calculation of the mutual inductance can be seen when the windings have the same radii and when they are concentric. For windings with the same radii, the Equation 2.8 needs to be rewritten as Equation 2.16 once there is a failure in the computation of the function C_i in that case, when $q = 0$.

$$C_i(R, R, z) = \frac{2}{\pi} \int_0^{\pi/2} \frac{A' \sin^2 \theta + B' \cos^2 \theta}{\sqrt{k^2 \cos^2 \theta + \sin^2 \theta}} d\theta \quad (2.16)$$

For concentric windings, there is a simplification of Equation 2.6 as the C_i function needs to be computed only twice, as shown in the Equation 2.17.

$$M = 4\pi\mu_0(R_1R_2)^{3/2}n_1n_2[C_i(R_1, R_2, z_1) - C_i(R_1, R_2, z_2)] \quad (2.17)$$

b) Self-Inductance

The self-inductance of an infinitesimally thin winding can be calculated as a simplification of the Equation 2.8 where $R_1 = R_2 = R$, $2l_1 = 2l_2 = h$ and $n_1 = n_2 = n$, as provided in Equation 2.18.

$$L = 4\pi\mu_0n^2(R)^3[C_i(R, R, h) - C_i(R, R, 0)] \quad (2.18)$$

The Equation 2.18 is solved by using Equation 2.16 for $z = 0$, providing the Equation 2.19.

$$L = 4\pi\mu_0n^2R^3 \left[C_i(R, R, h) - \frac{2}{3\pi} \right] \quad (2.19)$$

2.1.2. FEM for Inductance

The finite element method for the calculation of inductances is of simple application for linear cases, where there is no saturation, as its concept is unambiguous. This computation is either done by the flux linkage, which would be applicable when there is a uniform current density distribution, or from the energy in the magnetic field, that would compensate for the nonuniform current density distribution. Comprehensive explanation of the application of those methods is provided in [23] and is summarized as follows. One remark is that the solutions are provided in terms of permeance and not inductance, which would represent geometry and material properties only. In finite element software this analysis is extended to represent the actual windings, considering for example the number of turns of each winding.

a) Inductance from flux linkage

The self-inductance of a circuit, a winding for example, can be calculated by the ratio of the flux linkage and the current in that loop, when all the other sources nearby have no current flowing (open circuit). The mutual inductance would be the ratio of the flux which links the circuit i to another circuit j , considering all the other neighbor sources as open circuits. The circuit presented in Fig. 2.3 is taken to illustrate concepts explained below.

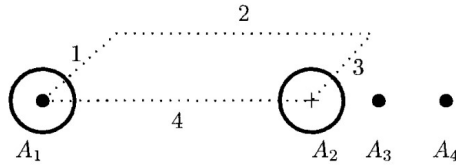


Figure 2.3 - Circuit example for inductance calculation.

The line integral of the vector potential in a closed path is equal to the magnetic flux linking that path, as shown in Equation 2.20.

$$\oint \vec{A} \cdot d\vec{l} = \psi_m \quad (2.20)$$

For the path indicated in Fig. 2.3, having a unit length the flux linkage would be

$$\psi_m = A_1 - A_2 \quad (2.21)$$

The permeance would then be

$$\mathcal{P}_1 = \frac{\psi_m}{I} \quad (2.22)$$

where I is the total current per turn in the conductor.

$$I = \iint_S \vec{j} \cdot d\vec{S} \quad (2.23)$$

As mentioned before, a correction is necessary for the calculation of the winding inductance. Therefore, the number of turns should be added as in Equation 2.24.

$$L_1 = N_1^2 P_1 \quad (2.24)$$

The same approach is used to calculate the mutual inductance, by exciting circuit 1 and finding the vector potential. The flux linkage for the circuit 2 will be the difference of the vector potential between points A_3 and A_4 . The permeance would be as per Equation 2.25.

$$P_{12} = \frac{A_3 - A_4}{I} \quad (2.25)$$

The correction to include winding information should also be done by multiplying this value by the number of turns in the circuit 2, which results in:

$$M_{12} = N_1 N_2 P_{12} \quad (2.26)$$

If there are other neighbor circuits of interest, the mutual inductances to circuit 1 can be calculated using the same field solution. For a case where there are N circuits, this will lead to a $N \times N$ matrix and N separate computations are necessary to obtain the complete solution. This is the case, for example, in air core reactors where there can be several circuits to be solved to compute the total inductance of the equipment.

b) Inductance from energy in the magnetic field

From the energy stored in the magnetic field, the permeance can also be calculated. In linear cases for example, that value can be taken from Equation 2.27.

$$W = \frac{1}{2} \int_V \vec{B} \cdot \vec{H} d\vec{v} \quad (2.27)$$

For 2-D simulations the one-meter depth is considered so the integration is performed over the surface area. By the definition of vector potential in the Equation 2.28 and the vector identity in the Equation 2.29, it is possible to describe the energy in the magnetic field as per Equation 2.30.

$$\nabla \times \mathbf{A} = \mathbf{B} \quad (2.28)$$

$$(2.29)$$

$$\nabla \cdot (A \times H) = (\nabla \times A) \cdot H - (\nabla \times H) \cdot A$$

$$W = \frac{1}{2} \int_v J \cdot A dv \quad (2.30)$$

The inductance is then obtained by:

$$L = \frac{2W}{I^2} \quad (2.31)$$

2.2 Eddy current losses

The credit for the discovery of the eddy currents (1855) was given to the French physicist Léon Foucault with the induced heating of the copper disc between the poles of a magnetic. Following Maxwell's theory of Electricity [13], the British mathematician Dr. Horace Lamb [25] discovered the skin effect in 1883, by determining the current distribution within a metal sphere. This effect is evidenced in Fig. 2.4 where the currents flowing in the center of the conductor are cancelled by the opposing currents generated by the alternating magnetic field. Those currents tend to reinforce the currents flowing in the outer part of the conductor while diminishing the ones circulating in the inner part of the conductor.

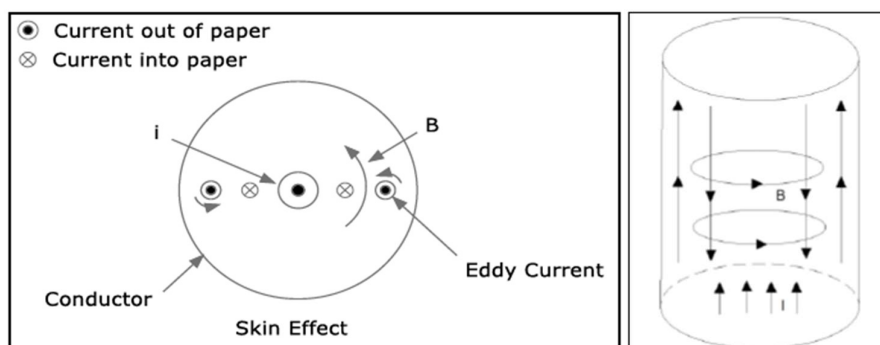


Figure 2.4 - Skin effect example.

The non-uniform distribution of the current density results in an increase of the AC resistance, consequently in the Joule losses as well. In Fig. 2.5, the current density distribution in a single wire of 5.2 mm is shown for a DC current and currents with 50 Hz and 10 kHz, respectively, evidencing the non-uniform distribution with the change of the frequency.

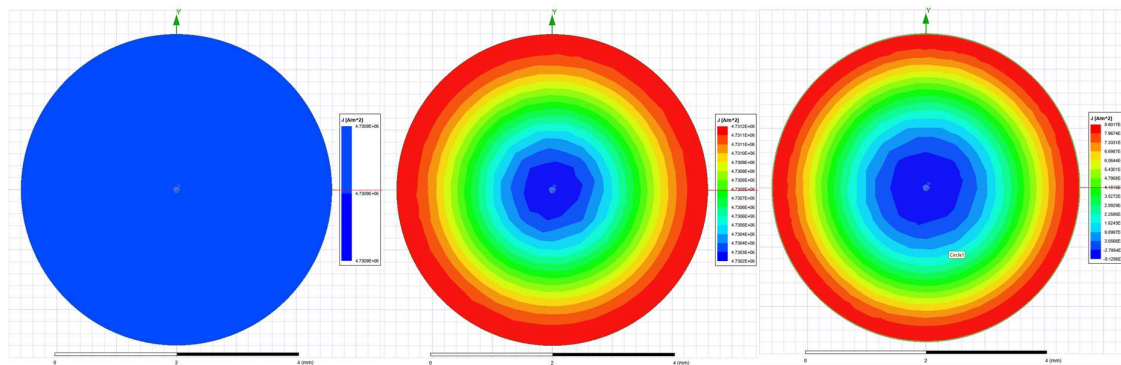


Figure 2.5 - Skin effect in a single wire for DC, 50 Hz and 10 kHz currents - ANSYS® Maxwell.

Analogously, when a conductor is exposed to a time-varying magnetic field, an eddy current is induced in the conductor, promoting the crowding of the current distribution as can be seen in Fig. 2.6 that represents two conductors carrying currents I in the same direction, subjected to the magnetic field intensity B , generated by each of those conductors.

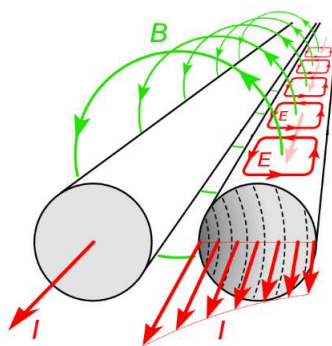


Figure 2.6 - Proximity effect between two conductors.

As the frequency increases so does the crowding of the current distribution, being mainly related to the magnetic field “penetration depth” or “skin depth” (δ). The effects of the skin and proximity effect in two round wires carrying DC, 50 Hz and 10 kHz currents can be seen in Fig. 2.7.

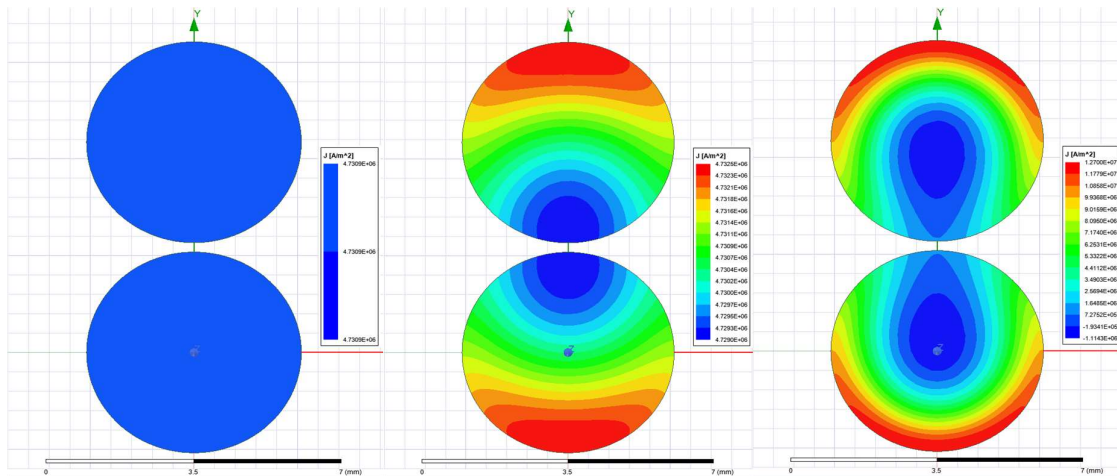


Figure 2.7 – Proximity and Skin effect in two wires for DC, 50 Hz and 10 kHz currents - ANSYS® Maxwell.

The effects of the eddy currents in most of the references are studied in the region of quasi-static fields, where the conductive currents are considered and the displacement currents are neglected, which is true even for high frequencies, as the conductors are usually made of materials with high electric conductivity [5]. This means that, as the dimensions of the typical power system are negligible compared to the speed of propagation of the electromagnetic waves, leading to very short times of wave propagation, it can be assumed that the magnetic fields are instantaneously established in all the points of the system under analysis.

In the same relevant work about inductance calculation methods, Dwight [20], in 1945, has also provided important contribution for the calculation of eddy currents in transformer windings and electrical machines, covering their effects (skin and proximity) on round wires, using modified Bessel's functions of order zero and of first and second kinds [26]. Dowell, in 1966, contributed with his work [6] which concerns the eddy current calculation for transformer windings, splitting them into winding portions, turning the round cross-sections into approximated square ones, and then using trigonometric functions instead of Bessel's functions.

In the same year, Lammeraner *et* Stafl published their vast and significant work [5] entitled "Eddy Currents" which has a tremendous contribution to the subject, being one of the most cited references in the literature. They provided calculations for the eddy effects for different types of conductors (e.g., round and square), using both trigonometric and Bessel functions in the solution of the problem.

So far, the previously mentioned works presented solutions considering the problem for sinusoidal excitations and in one-dimension, assuming foil windings. Assuming that the eddy currents flow close to the surface of the conductors and their depth of penetration depends on the conductivity and magnetic permeability of the material and the frequency of excitation,

different conductor configurations could be satisfactorily approximated as one-dimension problems, as the penetration distance is small compared to the conductor and overall dimensions of the equipment. However, there are cases that would require a two-dimension analysis.

Stoll [7], in 1974, reviewed the one-dimensional case, analogously to Dowell's proposal, and added important explanation about the two-dimensional analytical method. It also covers the use of the numerical method of finite-differences for the solution of one and two-dimensional problems with magnetic conductors and nonlinear properties. This approach is also used for problems involving system excitations with complicated functions of time, that may be not periodic. By that time, the authors had already started talking about the use of finite-element method for the solution of the eddy currents problem in windings, but with limitations related to the computational resources available.

In 1979, Perry [27] extended Dowell's work, focusing on the current density for the layers of a single winding, looking for the power dissipation per unit area. Examining those values, it would be possible to determine the optimum height and thickness for each layer to reduce total power losses. Although different layer thicknesses are considered in that work, the author emphasizes that the results are more reliable when the coils are long compared to their thickness. The schematic of a coil with several layer is presented in Fig. 2.8, where th_n is the thickness of the n^{th} layer and d_n is the outer diameter of the n^{th} layer. The different layers carry the same current I A/m.

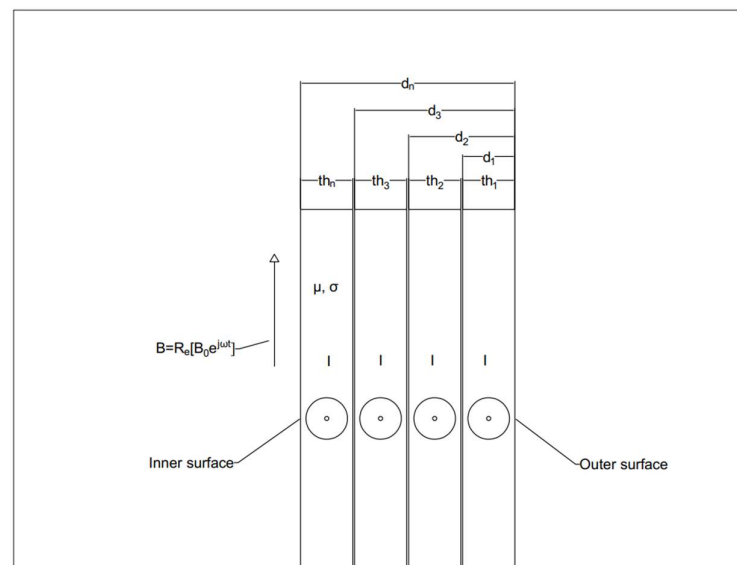


Figure 2.8 - Representation of a multi-layer winding. Source [27]

Urling *et al.* [8] published, in 1989, a comprehensive comparison among some of the previous works mentioned before, summarizing the theories, and the pros and cons of each of them, providing good guidance for the understanding of the developments available so far.

Burke *et Fawzi* [28], in 1991, contributed with a specific work about the proximity losses calculation for air core reactors using the proximity impedance matrix. As for the previous works, this one would be valid for quasistatic magnetic fields, where the capacitances and the dielectric losses can be neglected. The proximity loss in a turn would be the summation of the transverse magnetic losses, caused by the axial and radial magnetic fields created by all turns, where the curvature of the turn is neglected and transverse losses are assumed to be the same as the one for a long isolated straight conducting cylinder immerse in a uniform magnetic field. In that work, the author also proposed a methodology to split the windings into smaller sections in way that the magnetic field distribution could be considered uniform in those sections. Then the losses would be calculated for each section and the total losses of the winding would be the algebraic summation of section losses. Fig. 2.9 is a representation of a ACR with three concentric windings split into ten sections.

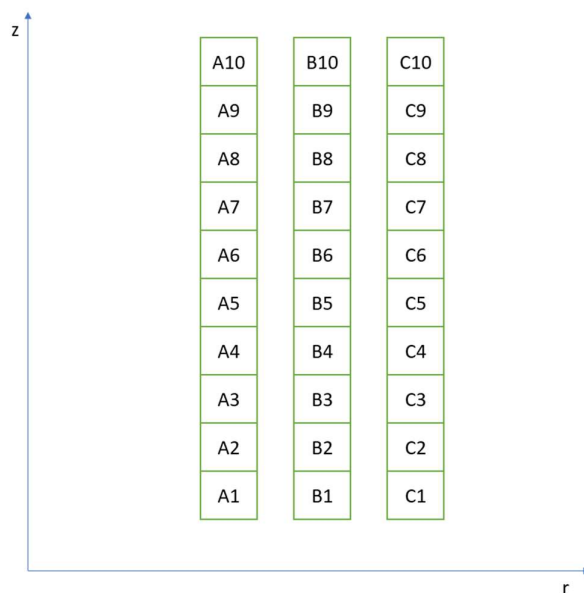


Figure 2.9 - Representation of ACR with three windings, split into ten sections.

In 1994, Ferreira [9], exploring the orthogonality between the skin effect and the proximity effect in multilayer windings, provided a more generalized approach for the analytical model of those effects on round conductors, allowing for more accurate results once exact equations for those conductors could be used instead of approximations of round to square

shapes as provided by the previous authors. The method was intended to mitigate errors caused by approximations like the introduction of square-shaped conductors with equivalent cross-sectional areas of the round conductors and the skin depth, that was previously presented as a function of geometries.

The increase in the AC resistance due to the skin effect can be accurately calculated by the Equation 2.32, discussed in [7], where γ is the ratio between the strand diameter and the skin depth and ber , bei , ber' and bei' are Kelvin functions [26].

$$R_{skin} = R_{dc} \frac{\gamma}{2} \left[\frac{ber(\gamma)bei'(\gamma) - bei(\gamma)ber'(\gamma)}{ber'^2(\gamma) + bei'^2(\gamma)} \right] \quad (2.32)$$

$$\gamma = \frac{d}{\delta\sqrt{2}} \quad (2.33)$$

$$\delta = \sqrt{\frac{2}{\omega\sigma\mu_0\mu_r}} \quad (2.34)$$

The orthogonality between the skin and proximity effect is explained to be valid when the magnetic field produced by the conductors is assumed to be uniformly distributed over the cross-section of the conductor under analysis, which simplifies the calculations. Assuming the current flowing in a winding conductor in the z direction, the current density distribution per unit length will be then a function dependent on the distribution in the x, y axis, and time, as per Equation 2.35.

$$J(x, y, t) = J(x, y)\cos(\omega t) \quad (2.35)$$

The total loss of a single strand for a sinusoidal current can be written following Equation 2.36.

$$P_{str} = \frac{1}{T\sigma} \int_{A_{sec}} \int_0^T |J(x, y)|^2 dt dA \quad (2.36)$$

Where A is the cross-sectional area of the conductor, T the period of the current waveform. Due to the radial symmetry of the current distribution in the wires of the winding and the assumption that the external magnetic field is transverse to the conductors and uniform,

Equation 2.36 can be written as

$$P_{str} = \frac{1}{2\sigma} \int_A (J_s J_s^* + J_p J_p^*) dA = P_s + P_p \quad (2.37)$$

where P_s is the loss per unit length due to the skin effect of a conductor, and P_p is the proximity effect loss per unit length induced on a conductor due to the equivalent magnetic field generated by all the remaining conductors of the winding(s). Those losses can be calculated by Equations 2.38 and 2.39 respectively

$$P_s = \frac{1}{2} R_{skin} I_{str}^2 \quad (2.38)$$

where I_{str} is the peak value of the current flowing in a conductor and R_{skin} is given by Equation 2.32 and

$$P_p = \frac{2\pi}{\sigma} \gamma (H_r^2 + H_z^2) F_x \quad (2.39)$$

where H_r and H_z are the total equivalent magnetic field strength in the radial and axial direction respectively, generated by the surrounding conductors, and F_x is here presented in the Equation 2.40.

$$F_x = \left[\frac{ber_2(\gamma)ber'(\gamma) + bei_2(\gamma)bei'(\gamma)}{ber^2(\gamma) + bei^2(\gamma)} \right] \quad (2.40)$$

Sullivan [29] proposed, in 2001 a study to calculate the eddy current losses by using the *Square-Field-Derivative Method*, which was supposed to present a reliable and fast solution to compute those losses for equipment with multiple windings, turns and even several strands by using the Equation 2.41, that represents the average power dissipation in a conductor with a length l .

$$P = \frac{\pi n l D_{str}^4}{64\rho} \overline{\left\langle \left(\frac{dB}{dt} \right)^2 \right\rangle} \quad (2.41)$$

where ρ is the resistivity of the conductor and $\overline{\langle \cdot \rangle}$ is the time average of the square derivative of the field. The method has one main restriction emphasized by the author, which is its

applicability only when the strand diameter is less or equal to twice the skin depth, implying to say that the method should be applied for frequencies that follow that criteria. Another point to be commented is that the proposed calculation method does not consider the skin effect, which may have a major impact for thicker conductors being exposed to currents with certain frequencies.

Later, in 2003 and 2004, the author presented two very comprehensive and dense studies [30, 31] using 2-D FEM simulations over a wide range of winding configurations to propose corrections to Dowell's and Ferreira's method of calculation for the proximity effect losses, provided that those methods would have their embedded lack of accuracy when accounting for this effect in higher frequencies. The presented idea was to consider the skin effect as per Equation 2.32 and add correction factors to the proximity effect based on the FEM simulations using curve-fitting, as explained below

$$P_p = \frac{\hat{G}H^2}{\sigma} \quad (2.42)$$

where \hat{G} is the normalized unitless proximity-effect loss correction factor which allows fitting different shapes of strand constructions, being a weighted average of two functions as per Equation 2.43

$$\hat{G} = (1 - w)\hat{G}_1(X) + w\hat{G}_2(X) \quad (2.43)$$

where \hat{G}_1 is the so-called modified Dowell function and \hat{G}_2 the dual slope function,

$$\hat{G}_1(X) = \frac{3\pi}{16} k^{-3} X \frac{\sinh kX - \sin kX}{\cosh kX + \cos kX} \quad (2.44)$$

where k is a function of strands spacing v/D_{str} and h/D_{str} and X can be defined as per Equation 2.45. Fig. 2.10 represents the interturn distance (v) and the interlayer distance (h) of the strands.

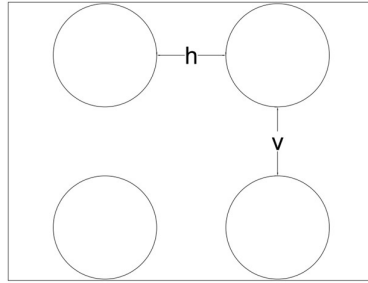


Figure 2.10 - Representation of interturn (v) and interlayer (h) distances.

$$X = \frac{D_{str}}{\delta} \quad (2.45)$$

$$\hat{G}_2(X) = \frac{\pi}{32} \frac{X}{(X^{-3} + m^3)} \quad (2.46)$$

In 2007, Acero *et al.* provided a detailed work [32] related to the calculation of power losses on twisted multistranded cables using a mixed approach taking advantage of the methods previously discussed in this study and 2-D finite element simulations. The study covered comparisons between the power losses for the twisted cable and those for the equivalent solid wire, emphasizing that treating the stranded cables by using equivalent solid geometries would lead to mistakes, as the proximity effect internal to the cable would not be properly addressed. Fig. 2.11 shows the current distribution due to the proximity and skin effect for a 19 strands cable.

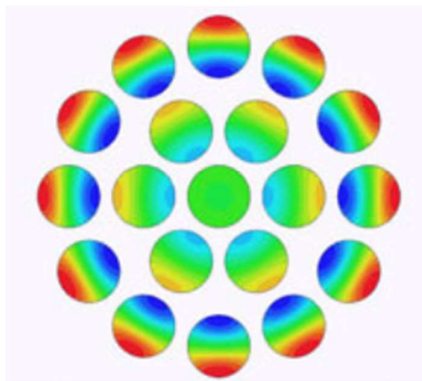


Figure 2.11 - Current distribution for a 19 strands cable at high frequency.

More recently, with the outbreak of superconducting materials, the use of flat transposed cables (Rutherford cables) became more evident and many studies have been published in the sense of providing improved calculation models for the power losses and heating of those cables which, in general, will be subjected to very high currents and magnetic fields. Although their

composition is not the same of the ACRs, using special high conductivity alloys instead of aluminum or copper, the efforts applied on the research for those improved models would also be applicable to other types of conductors. The studies provided for *Litz* wires is also a good source of understandings that could be applied to the calculation of the winding power losses of the ACRs as the application of this type of conductor is intended to reduce eddy currents losses as well. Roßkopf *et al.* showed in their work [33] a way to simulate the twisting effect of a stranded cable instead of assuming the same initial current distribution for all the strands, allowing this distribution to change according to the position of the strands in the cable. Information was also provided about the relevance of the number of edges considered in the 2-D and 3-D simulation of round conductors using FEA software, which is a relevant information considering that when round geometries are used in FEM, the software will tend to approximate them to polygons for a better meshing and this would lead to slightly different DC resistances, affecting the losses calculation as well.

Islam, in his work [34], reviewed a wide range of studies related to the power losses calculation for electrical machines, also covering many topics for the proper simulation of windings using FEA software, being a very comprehensive source for the development of this study.

2.2.1. Analytical model

The analytical method for the calculation of the total power winding losses considered in this work is a mixture of the Ferreira's method [9] and the proposition of Burke and Fawzi [28]. Which means that the windings are split into smaller sections where the magnetic field is assumed to be uniform and calculated only in the geometric center of each section. The losses are calculated for each section considering their amount of turns and strands. Skin and proximity effect losses are calculated separately and superposed later in the process. The total winding power losses (P_{tot}) can be calculated by the Equation 2.47. The steps of the process for the calculation of the total power losses for a single winding using flat transposed cables are described below.

$$P_{tot} = P_{dc} + P_{skin} + P_{prox} \quad (2.47)$$

a) DC losses

The DC resistance (R_{dc}) for a winding with a flat transposed cable can be calculated by Equation 2.48

$$R_{dc} = \frac{4\pi \cdot D_{av} \cdot n}{N_{str} \cdot \pi \cdot D_{str}^2} k_{str} \quad (2.48)$$

where D_{av} is the average diameter of the winding, n is the number of turns, N_{str} is the number of strands and D_{str} the strand diameter. For those cables the DC resistance shall be corrected due to the longer length of the strands when compared to the total length of the cable (stranding factor), so the factor k_{str} is added to represent that increase. The losses can be then calculated by Equation 2.49.

$$P_{dc} = R_{dc} \cdot i_t^2 \quad (2.49)$$

where i_t is the total current of flowing through the winding.

b) Skin effect

The skin effect will be reflected as an increase in the AC resistance and can be written as follows.

$$\frac{R_{skin}}{R_{dc}} = \frac{\gamma}{2} \left[\frac{ber(\gamma)bei'(\gamma) - bei(\gamma)ber'(\gamma)}{ber'^2(\gamma) + bei'^2(\gamma)} \right] - 1 \quad (2.50)$$

The losses due to skin effect can be now calculated by Equation 2.51.

$$P_{skin} = R_{skin} \cdot i_t^2 \quad (2.51)$$

c) Proximity effect

As the different sections of the winding will be exposed to different levels of magnetic fields, the contribution of the proximity effect to the total power losses in each one of them will be different. The winding losses due to the proximity effect can be calculated by Equation 2.39. Applying that equation to one section “ j ” from N_{sec} would lead to

$$P_{prox,j} = \frac{2\pi}{\sigma} \gamma (H_{j,r}^2 + H_{j,z}^2) F_x \pi D_{av} n_j N_{str} \quad (2.52)$$

where $H_{j,r}$ is the magnetic field strength in the radial direction, $H_{j,z}$ is the magnetic field strength axial direction and n_j is the number of turns, being the three of them referred to the section “j”. The total losses due to the proximity effect can be then calculated by Equation 2.53.

$$P_{prox} = \sum_j^{N_{sec}} P_{prox,j} \quad (2.53)$$

2.2.2. Finite Element Model

The Eddy Current solver [24] available in ANSYS® Maxwell is the tool used in this study for the calculation of the total winding power losses. In general, the solution will account for the distribution of the current density inside the geometry of the conductors, interlacing with the frequency of the current flowing through the conductor and the induced currents generated by the remaining conductors of the system. This calculation is done internally in the software by solving the Equation 2.54, in each volume, which, in this case, corresponds to the area of the 2-D geometry multiplied by its perimeter, when dealing with RZ coordinates.

$$P_{tot} = \int_{Vol} \frac{J \cdot J^*}{2\sigma} dVol \quad (2.54)$$

The solver interprets each conductor as a separate circuit, injecting a 1 A_{peak} current in each one of those circuits separately, “opening” the others (zero current condition). Using the field solutions, the solver creates the impedance matrix, being solved primarily for the inductances, followed by the resistances, as summarized in Fig. 2.12.

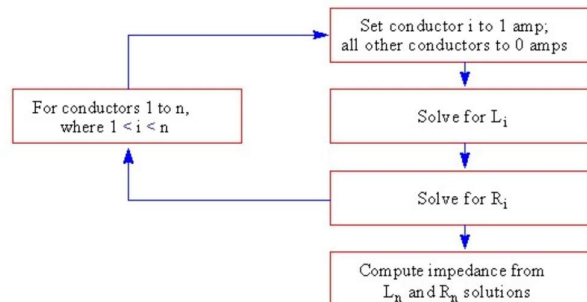


Figure 2.12 - Impedance matrix solving process - ANSYS® Maxwell.

a) DC losses

In the Eddy Current solver only currents with their related frequencies can be considered in the simulation. For that reason, considering a winding current with a frequency of 10^{-8} Hz could be an artifice to solve Equation 2.54 as if it was related to DC currents.

b) Skin and proximity effects

Eddy current effects are computed in the Eddy Current solver by solving Equation 2.54, following the steps described above and considering the proper frequencies for the desired input currents. This is applicable for all solid conductors.

For the *Litz cable* feature, available in the same solver and later detailed in this work, the approach would be different as only the proximity effect losses are calculated (postprocessing) based on Equation 2.55

$$P_{prox} = \frac{\sigma \pi^3 D_{str}^4 f^2 B_p^2}{32} \quad (2.55)$$

where B_p is the peak flux density. The approach is said to be valid for sinusoidal excitations and only when the thicknesses of the strands are smaller or equal to the skin depth, as explained in [29].

2.2.3. Design of experiments

To understand the behavior of a system, being either at the design stage or an already implemented process, one possible approach would be to run some experiments on real products or computational simulations, for example, acquiring the relevant measurement data and treating them statistically. By doing that it would be possible to establish the correlations between the process or design variables and their characteristics that would be critical to quality (CTQ), or just variables of interest, evaluate the performance of the system in terms of probability of failure, compare different solutions and even propose adjustment to existing models based on their behavior when compared to similar solutions (benchmarking). This set of experiments would be called design of experiments (DOE) [12]. A DOE can be set in a way to provide reliable information about a whole process or design by running just a few experiments. This would be done in several different ways. The chosen format for this work is

the application of the full factorial design [12], which in this case means to say that if a desired characteristic y is a function of the variables x_1 and x_2 , and those variables have their own limits of variability, a DOE can be set by screening the variables in their lower and upper limits (-1 and 1) and the set of experiments can be drawn as per Table 2.1.

Table 2.1 - Full factorial representation of a two level, two factors DOE.

x_1	x_2	y
-1	-1	Data1
1	-1	Data2
-1	1	Data3
1	1	Data4

The number of experiments in a full factorial design can be calculated by Equation 2.56.

$$N_{exp} = m^k \quad (2.56)$$

where m is the number of levels of the variables and k is the number of variables (factors) that affect the CTQ characteristic.

2.2.4. Response Surface Method

After the experiments are run, the behavior of the measured data can be described by an equation that represents the fitted curve over those data points. In case the DOE has three or more levels for the variables, a response surface method (RSM) can be applied to provide that equation [35]. This method will also provide information about the correlation between the variables and the CTQ. That correlation is usually expressed in terms of the P-value [35], which describes the probability of significance in a hypothesis test. A common P-value is 0.05, which means a confidence interval of 95 %. For the RSM, the null hypothesis (H_0) is that the variable has no impact on the CTQ. In case the P-value for a certain variable becomes lower than 0.05, this would mean a great probability of contradiction of the null hypothesis, meaning that the change on the variable under analysis has a significant impact on the results of the CTQ.

3. METHODOLOGY

The high variability of the design of ACRs is mainly driven by the different requirements of the pair inductance \times current, which are related to the different types of application of inductors in power systems. The design constraints will be imposed mainly by manufacturing limitations and design criteria limits inherent to the developed technologies and deployed by each manufacturer. To cover for that variability, it is necessary to identify the main variables that affect the design of the ACRs. The methodology deployed in this study was to first confirm the equivalence between the analytical model and the FEM concerning the total inductance (self and mutual) of the windings as that would be the indicative that their geometry and magnetic field distribution are appropriately comparable. Once the equivalency is verified, the simulations of the power losses take place, aiming firstly to stablish a good agreement for the DC losses with subsequent analysis of the winding eddy current losses. Both set of results, for the inductance and for the power losses, are statistically compared and improvements for the analytical method shall be proposed based on that.

3.1 Design parameters for DOE

Considering a given inductance and current values, a designer can almost freely choose the design of an air core reactor that will fit into those values. In that choice there are several factors that would impact the design. Factors like the diameter and the height of the winding, its number of turns, the number of strands in a turn and their diameter are some of the most impactful characteristics on the design of the ACRs, among others provided in Fig. 3.1.

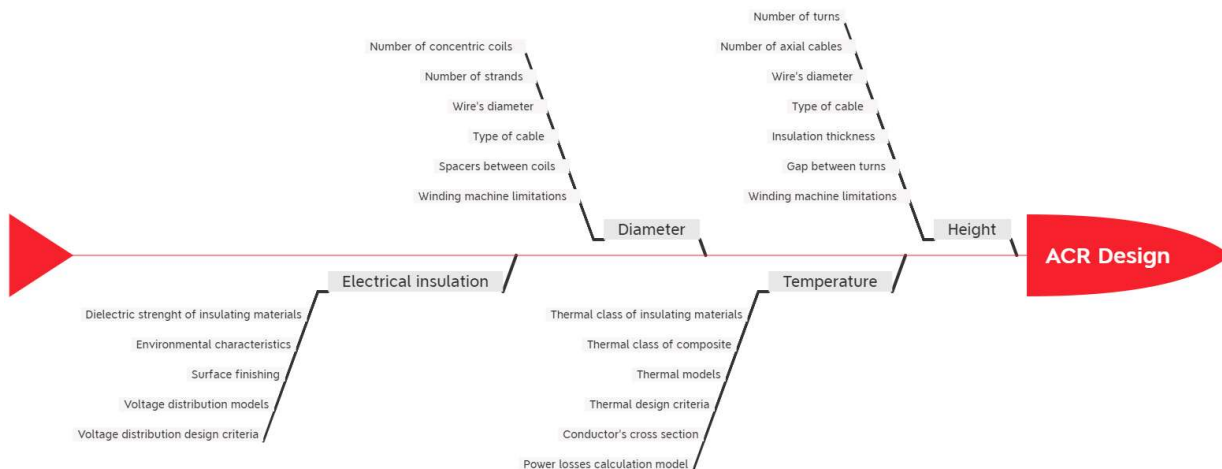


Figure 3.1 - Impacting factors on ACR design.

The choice made for the current study was to work with ACRs composed by only one cylinder (winding), made of aluminum flat transposed cables. The four main design parameters, average winding diameter (D_{av}), winding height (H_w), number of strands of the winding (N_{str}) and diameter of the strands (D_{str}) are chosen and screened in three different levels, low (L), medium (M) and high (H), each parameter having its own set of levels corresponding to the magnitude of the design characteristics. Those levels shall be used to represent the complete manufacturing capability of a manufacturer, for example, or just a range of interest for a certain study. All the design characteristic levels are crescent from low to high, which corresponds to a lower value of the characteristic for L and a higher for H. Fig. 3.2 provides the correspondence of the design parameters and their screening levels. The results of this kind of approach would be valid only for levels of the design characteristics contained between their low and high levels.

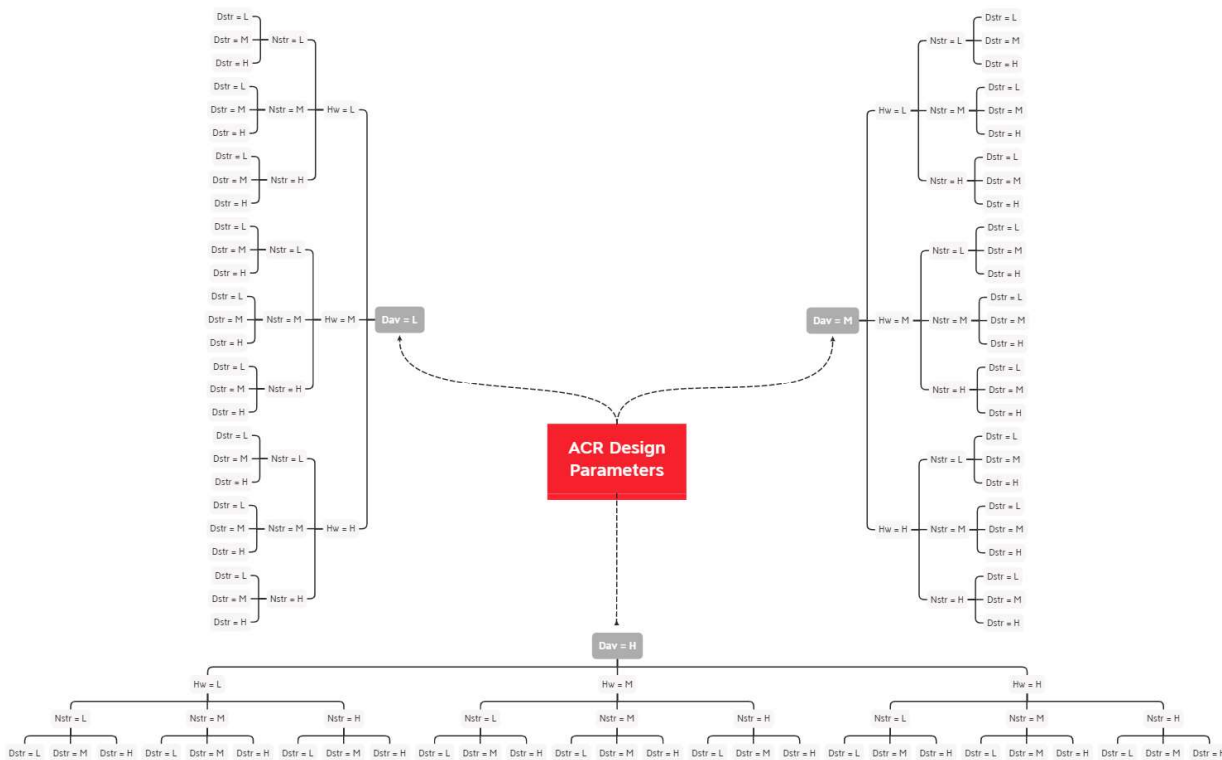


Figure 3.2 - Design parameters and their screening levels.

The three-level screening is considered to have an intermediate level so a curve can be fit rather than a straight line, that would be the only possible solution if there were two levels. When considering four factors at three different levels, this results in a full factorial design of experiments of 81 combinations by following Equation 2.56, which are referred here as ACR1 to ACR81, as shown in Table 3.1.

Table 3.1 - Experiments nomenclature and their design parameters levels.

Reference	Design parameter levels				Reference	Design parameter levels			
	D _{av}	H _w	N _{str}	D _{str}		D _{av}	H _w	N _{str}	D _{str}
ACR1	L	L	L	L	ACR42	M	M	M	H
ACR2	L	L	L	M	ACR43	M	M	H	L
ACR3	L	L	L	H	ACR44	M	M	H	M
ACR4	L	L	M	L	ACR45	M	M	H	H
ACR5	L	L	M	M	ACR46	M	H	L	L
ACR6	L	L	M	H	ACR47	M	H	L	M
ACR7	L	L	H	L	ACR48	M	H	L	H
ACR8	L	L	H	M	ACR49	M	H	M	L
ACR9	L	L	H	H	ACR50	M	H	M	M
ACR10	L	M	L	L	ACR51	M	H	M	H
ACR11	L	M	L	M	ACR52	M	H	H	L
ACR12	L	M	L	H	ACR53	M	H	H	M
ACR13	L	M	M	L	ACR54	M	H	H	H
ACR14	L	M	M	M	ACR55	H	L	L	L
ACR15	L	M	M	H	ACR56	H	L	L	M
ACR16	L	M	H	L	ACR57	H	L	L	H
ACR17	L	M	H	M	ACR58	H	L	M	L
ACR18	L	M	H	H	ACR59	H	L	M	M
ACR19	L	H	L	L	ACR60	H	L	M	H
ACR20	L	H	L	M	ACR61	H	L	H	L
ACR21	L	H	L	H	ACR62	H	L	H	M
ACR22	L	H	M	L	ACR63	H	L	H	H
ACR23	L	H	M	M	ACR64	H	M	L	L
ACR24	L	H	M	H	ACR65	H	M	L	M
ACR25	L	H	H	L	ACR66	H	M	L	H
ACR26	L	H	H	M	ACR67	H	M	M	L
ACR27	L	H	H	H	ACR68	H	M	M	M
ACR28	M	L	L	L	ACR69	H	M	M	H
ACR29	M	L	L	M	ACR70	H	M	H	L
ACR30	M	L	L	H	ACR71	H	M	H	M
ACR31	M	L	M	L	ACR72	H	M	H	H
ACR32	M	L	M	M	ACR73	H	H	L	L
ACR33	M	L	M	H	ACR74	H	H	L	M
ACR34	M	L	H	L	ACR75	H	H	L	H
ACR35	M	L	H	M	ACR76	H	H	M	L
ACR36	M	L	H	H	ACR77	H	H	M	M
ACR37	M	M	L	L	ACR78	H	H	M	H
ACR38	M	M	L	M	ACR79	H	H	H	L
ACR39	M	M	L	H	ACR80	H	H	H	M
ACR40	M	M	M	L	ACR81	H	H	H	H
ACR41	M	M	M	M					

3.2 FEM with the 2-D equivalent geometry method

In software based on finite element methods, it is usually possible to simulate many physical phenomena. In this work, the software *ANSYS® Maxwell, Release 20.1* [24] was used, more specifically, the *Eddy Current Solver* that allows for detailed calculation of the distribution of AC magnetic fields and its effects. As the idea of the current work is to present an improved, fast and reliable process for the modeling of ACRs, setting the baseline for further developments, it is reasonable to expect that the type of solution analyzed would be based on 2-D geometries, where there would be significantly lower computational demand. To take advantage of 2-D simulations, only geometries which present radial symmetry can be considered. In the assembly of the ACRs the windings are the only structures that may present such a symmetry and therefore they were the ones considered for the simulations. When representing the 2-D geometry of the windings it would be necessary, in a regular approach, to draw all the winding turns and the cable strands that compose the turns. In Fig. 3.3, the representation of wires of one turn of a FTC with 20 strands can be seen.

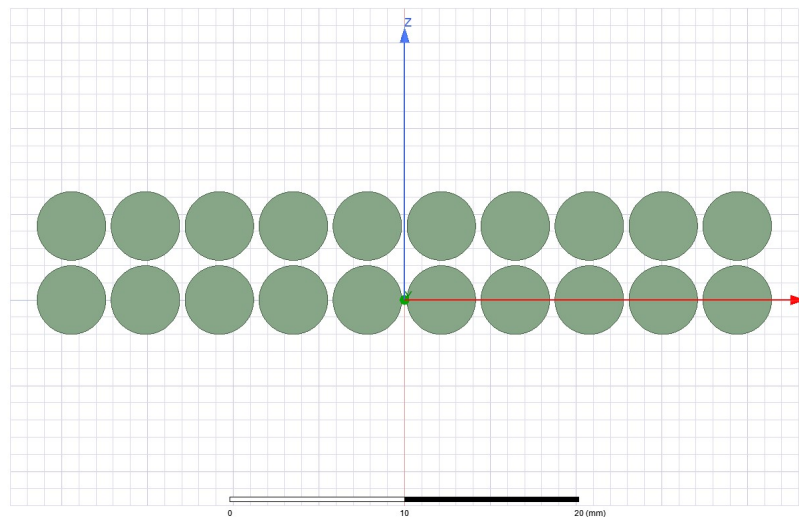


Figure 3.3 - 2-D representation of one turn of a FTC.

A 2-D representation of a winding with 10 turns, composed by one FTC with 20 strands can be seen in Fig. 3.4. When representing the winding in such a way it is necessary to pay attention to the distance between the wires and between the turns, the average winding diameter, its height and the diameter of the strands, as those would be the most impactful characteristics on inductance values.

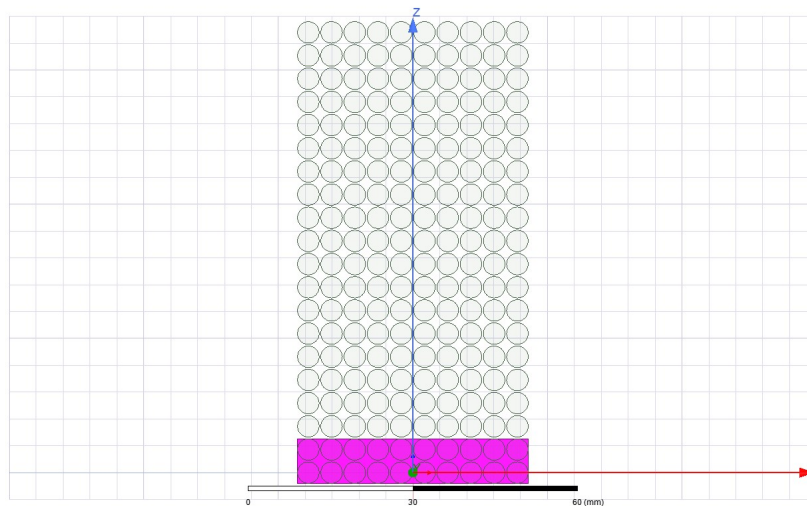


Figure 3.4 - 2-D representation of a winding with 10 turns of FTC.

Simulations in software based on FEM usually go through the following steps: selection of the proper solver for the physical phenomena to be analyzed; drawing or importing the geometry of the object to be studied; assigning material properties and boundary conditions of the region of simulation; assigning the proper excitations of the system (e.g. electrical current, voltages, mechanical loads); performing the meshing generation and refinement; setting up the solution parameters and solving the system accordingly; postprocessing the data (flux density evaluation) to obtain the desired characteristics of the system, as summarized in Fig. 3.5.

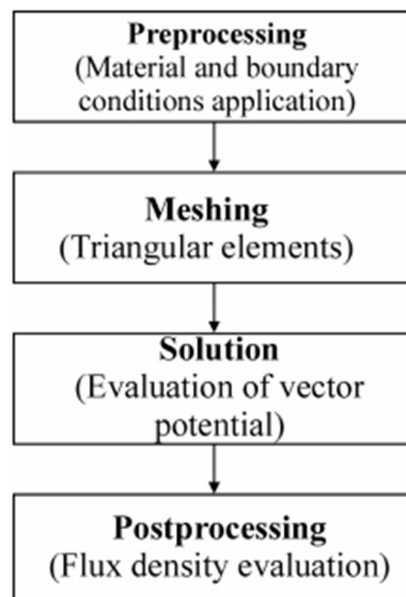


Figure 3.5 - Simulation with finite element method flowchart.

For the case of the transposed cables, aiming to solve for either the winding total inductance or the winding power losses it is necessary to impose a condition of parallel current for each turn of the winding, Fig. 3.6, meaning that each wire would be subjected to a fraction of the total current, otherwise the software would interpret that each strand should be analyzed independently which would increase the inductance matrix and would also not be representative of the real problem. This increases the preprocessing time and the risk of inserting wrong information.

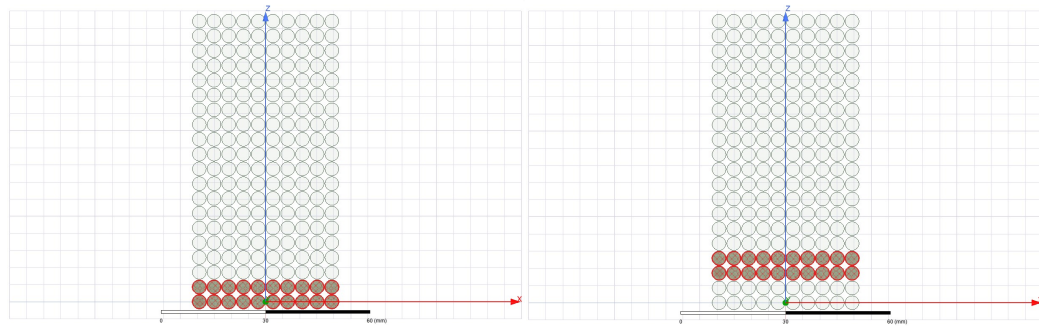


Figure 3.6 - Parallel current representation per turn.

Besides the need in the preprocessing step, another issue of simulating strand by strand would be the high computational time to find a proper mesh refinement for all the strands. For the ACRs, the magnitude of the number of strands may be of hundreds of thousands. Also, in this case the interactions of the magnetic fields between the strands would be high, requiring a better mesh refinement of those regions as well, which will also contribute to the increase in the simulation time. An example of mesh refinement is provided in Fig. 3.7.

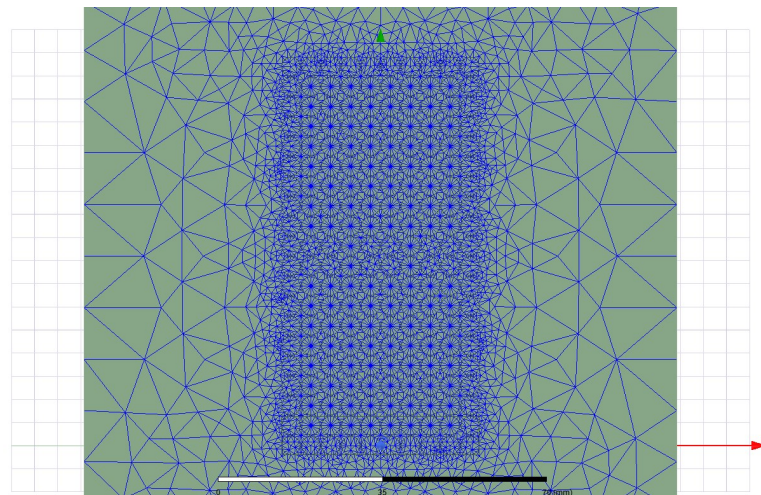


Figure 3.7 - Initial meshing for strand by strand simulation.

One possible improvement to that type of simulation has been proposed in [24], which explores the possibility of drawing an equivalent contour around a complete cable of a turn and providing its characteristics externally to describe what is the type of strand (round or rectangular), the number of strands and its dimensions (diameter), as shown in Fig. 3.8. As the inductance of a winding is affected by its diameter, the number of turns and their height, it can be expected that this approach would be appropriate, assuming that the general geometry of the winding would be respected.

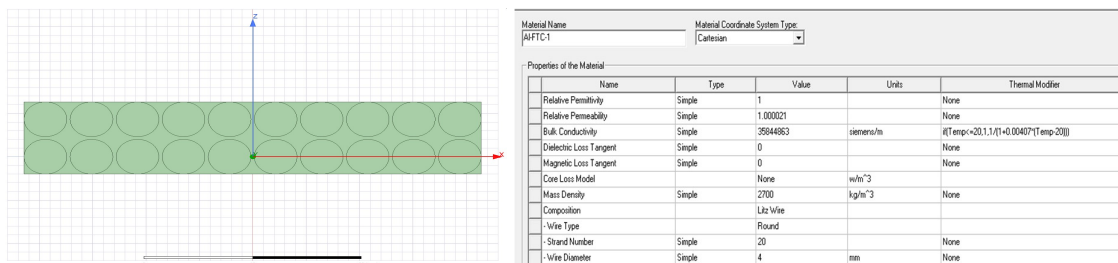


Figure 3.8 - Equivalent geometry for a 2D turn and external setup.

Although the problem would now be significantly reduced, it can be still related to some dozens of thousands of turns, which will also require the assignment of current sources to each one of them, as well as the proper postprocessing for the series and parallel arrangement of the turns and the windings.

The approach proposed in this work is to consider a 2-D equivalent geometry for the whole winding so the software will recognize that all the turns are in series and each turn will be interpreted in terms of its number of strands and strand diameter. This could be achieved by drawing the geometry to cover the width and the height of the windings completely. By doing that, only one parallel current needs to be assigned by winding and no additional operation needs to be done to properly set the turns assembly, as shown in Fig. 3.9.

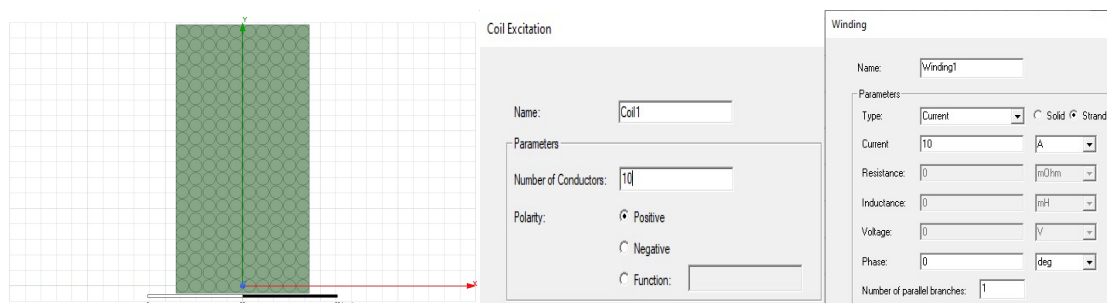


Figure 3.9 - Equivalent geometry for a 2-D winding with 10 turns and external setup.

3.3 Comparison of inductance values

The total inductance values for the 81 experiments were captured for both the analytical and the finite element models and the percent deviation of these values related to the formers are captured in Table 3.2.

Table 3.2 - Inductance deviation between FEM and analytical model.

Reference	% Inductance variation	Reference	% Inductance variation	Reference	% Inductance variation
ACR1	-0.072	ACR28	-0.044	ACR55	-0.030
ACR2	-0.070	ACR29	-0.050	ACR56	-0.044
ACR3	-0.060	ACR30	-0.034	ACR57	-0.043
ACR4	-0.085	ACR31	-0.032	ACR58	-0.022
ACR5	-0.077	ACR32	-0.041	ACR59	-0.045
ACR6	-0.067	ACR33	-0.044	ACR60	-0.046
ACR7	-0.021	ACR34	0.047	ACR61	0.060
ACR8	-0.071	ACR35	-0.014	ACR62	-0.008
ACR9	-0.082	ACR36	-0.044	ACR63	-0.030
ACR10	-0.067	ACR37	-0.030	ACR64	-0.033
ACR11	-0.062	ACR38	-0.027	ACR65	-0.024
ACR12	-0.042	ACR39	-0.030	ACR66	-0.021
ACR13	-0.118	ACR40	-0.047	ACR67	-0.039
ACR14	-0.086	ACR41	-0.043	ACR68	-0.035
ACR15	-0.056	ACR42	-0.034	ACR69	-0.023
ACR16	-0.186	ACR43	-0.066	ACR70	-0.050
ACR17	-0.158	ACR44	-0.061	ACR71	-0.048
ACR18	-0.096	ACR45	-0.043	ACR72	-0.040
ACR19	-0.063	ACR46	-0.026	ACR73	-0.025
ACR20	-0.057	ACR47	-0.026	ACR74	-0.020
ACR21	-0.037	ACR48	-0.023	ACR75	-0.025
ACR22	-0.122	ACR49	-0.047	ACR76	-0.040
ACR23	-0.088	ACR50	-0.036	ACR77	-0.030
ACR24	-0.051	ACR51	-0.025	ACR78	-0.024
ACR25	-0.212	ACR52	-0.075	ACR79	-0.054
ACR26	-0.169	ACR53	-0.064	ACR80	-0.050
ACR27	-0.099	ACR54	-0.039	ACR81	-0.032

The analytical model for the calculation of self and mutual inductances deployed in this study, as explained in [22], would present the errors in the order of 10^{-d} , where d is the number of significant figures used in the computations. Therefore, the method can be used as a very reliable reference for comparison with other proposed approaches.

Displaying the observed variation of total inductance between the FEM and the analytical model in a run chart would be a reasonable way of looking for possible outliers, as can be seen in Fig. 3.10. A major cluster is formed around of -0.05 % and almost all the inductance values provided by the FEM are lower than the ones from the analytical model.

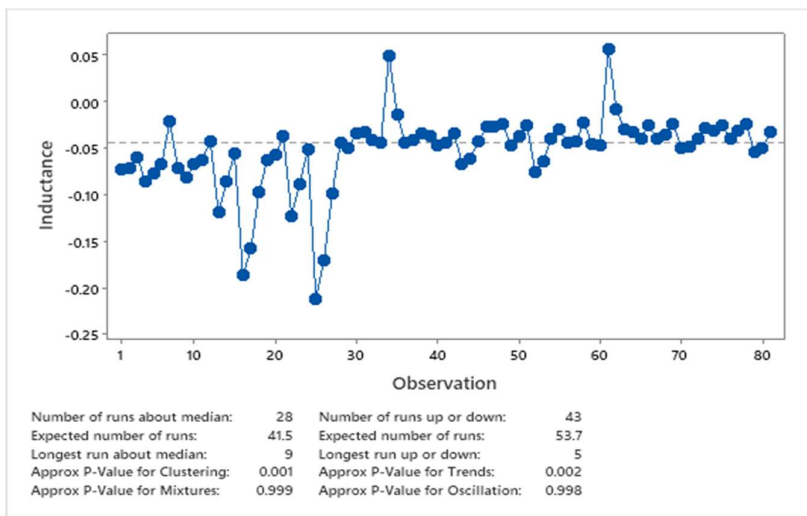


Figure 3.10 - Inductance variation between FEM and analytical model.

During the preparation of the experiments in the FEM software the run chart was an important tool to identify mistakes. One example to be mentioned is the proper setting of the boundary conditions dimensions, that may have a significant impact on the inductance calculation as they may alter the distribution of the flux lines, as exemplified in Fig. 3.11.

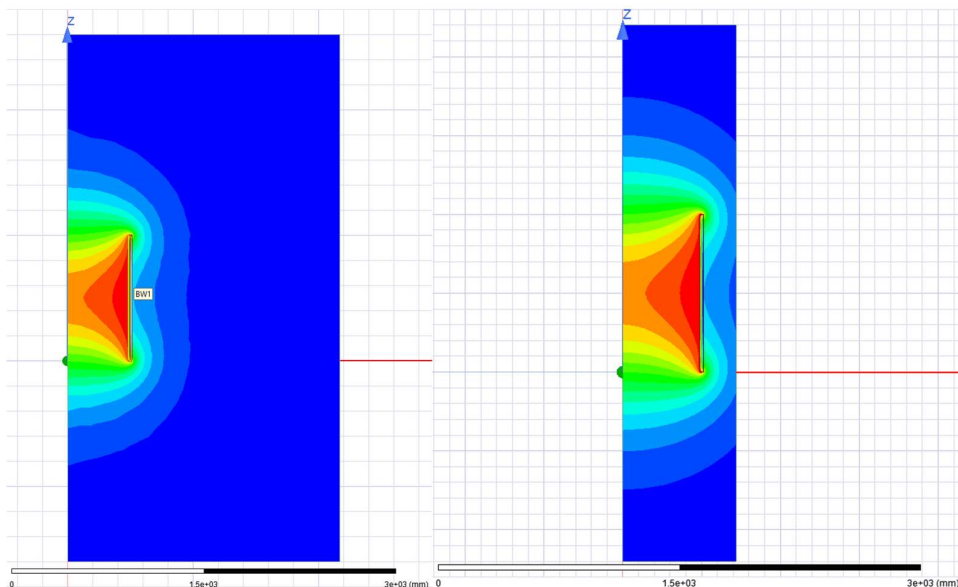


Figure 3.11 - Boundary conditions setups example – ACR1.

3.4 FEA of eddy current winding losses

At this point it is possible to infer that the flux linkage resulting from the integration of the magnetic field is equivalent for both methods. Local discrepancies in the distribution of the magnetic field between both models might still exist, that is mitigated by using a fine meshing in the cross-section of the winding so the analysis of winding losses can be performed with a minor chance of having lurking variables generated by uncertainty related to geometry and the assembly of the model. In Fig. 3.12, the distribution of the magnetic field is evidenced, also showing its distribution internally to the winding.

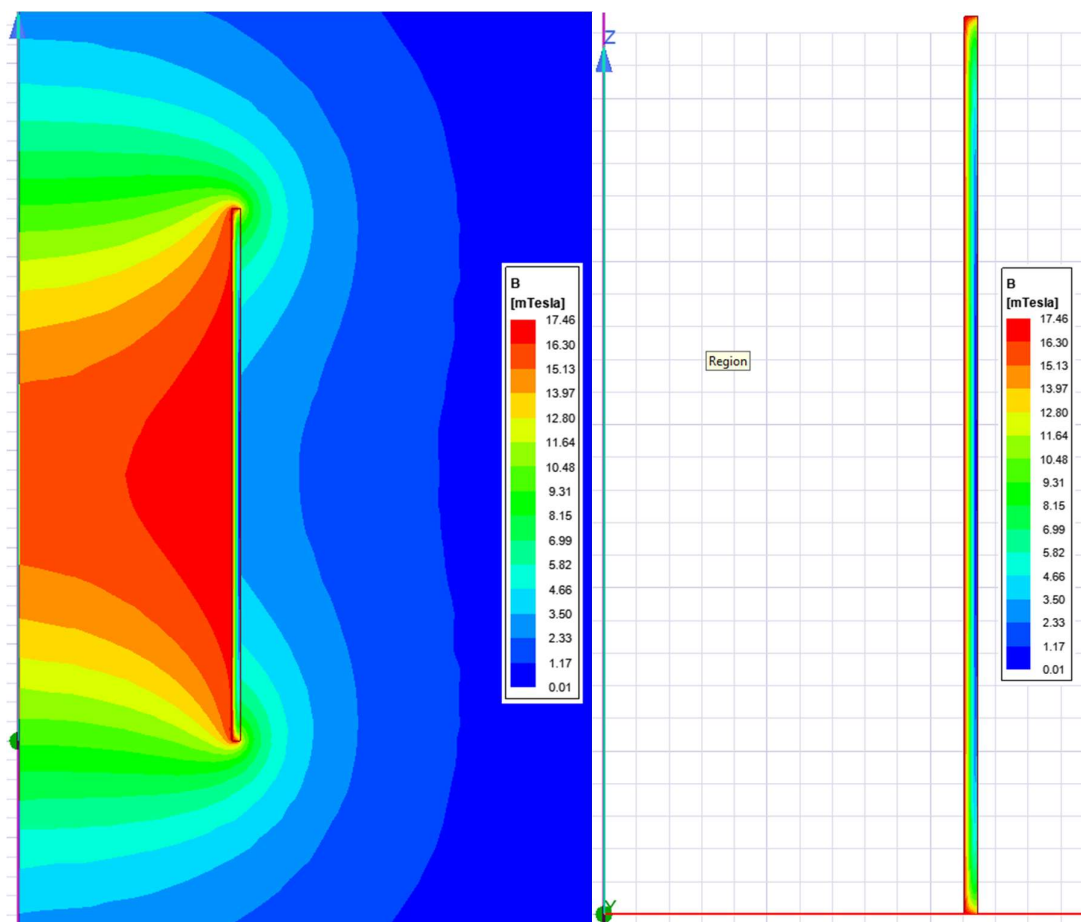


Figure 3.12 - Magnetic field distribution in space and internally to the winding – ACR79.

The same approach was considered for the 81 experiments, providing analogous results.

As explained in 2.2.2, *ANSYS® Maxwell* has its own embedded calculation methods for postprocessing power losses. The Eddy Current solver present in the FEM software computes electromagnetic fields in the frequency domain in 2-D or 3-D.

The first sanity check was to verify whether the DC winding losses would have a good agreement between both models (analytical and FEM). To represent the calculation of the DC winding power losses in the FEM software a current with a frequency of 10^{-8} Hz is injected in the winding, therefore mitigating the skin and proximity effects. The percent deviations between the DC losses obtained by the Eddy Current solver and the analytical calculation are presented in Table 3.3.

Table 3.3 - DC losses percent deviation between FEM and analytical model.

Reference	% DC losses variation	Reference	% DC losses variation	Reference	% DC losses variation
ACR1	-1.747	ACR28	-1.747	ACR55	-1.747
ACR2	-1.498	ACR29	-1.498	ACR56	-1.498
ACR3	-1.870	ACR30	-1.870	ACR57	-1.870
ACR4	-1.747	ACR31	-1.747	ACR58	-1.747
ACR5	-1.498	ACR32	-1.498	ACR59	-1.498
ACR6	-1.870	ACR33	-1.870	ACR60	-1.870
ACR7	-1.747	ACR34	-1.747	ACR61	-1.747
ACR8	-1.498	ACR35	-1.498	ACR62	-1.498
ACR9	-1.870	ACR36	-1.870	ACR63	-1.870
ACR10	-1.747	ACR37	-1.747	ACR64	-1.747
ACR11	-1.858	ACR38	-1.858	ACR65	-1.858
ACR12	-1.930	ACR39	-1.930	ACR66	-1.930
ACR13	-1.747	ACR40	-1.747	ACR67	-1.747
ACR14	-1.858	ACR41	-1.858	ACR68	-1.858
ACR15	-1.930	ACR42	-1.930	ACR69	-1.930
ACR16	-1.747	ACR43	-1.747	ACR70	-1.747
ACR17	-1.858	ACR44	-1.858	ACR71	-1.858
ACR18	-1.930	ACR45	-1.930	ACR72	-1.930
ACR19	-1.960	ACR46	-1.960	ACR73	-1.960
ACR20	-1.960	ACR47	-1.960	ACR74	-1.960
ACR21	-1.911	ACR48	-1.911	ACR75	-1.911
ACR22	-1.960	ACR49	-1.960	ACR76	-1.960
ACR23	-1.960	ACR50	-1.960	ACR77	-1.960
ACR24	-1.911	ACR51	-1.911	ACR78	-1.911
ACR25	-1.960	ACR52	-1.960	ACR79	-1.960
ACR26	-1.960	ACR53	-1.960	ACR80	-1.960
ACR27	-1.911	ACR54	-1.911	ACR81	-1.911

The material of the conductor was set to be aluminum with an electrical conductivity (σ) of 35,844,863 S/m. The reference temperature for all experiments was set to be 20 °C which matches with the reference temperature for the mentioned electrical conductivity, therefore it does not require any additional correction. The relative magnetic permeability (μ_r) of the aluminum conductors in the experiments was considered as 1.000021.

When dealing with stranded or flat transposed cable it is important to have in mind that the total length of the strands will be longer than the length of the cable itself (stranding effect), resulting in a higher DC resistance as this one increases with the length of a conductor. That effect is considered in the analytical model but it is not applied in the same way in the FEM, when considering the 2D equivalent geometry proposed in this study. That would have a major impact in the calculation of the winding power losses for lower frequencies, where DC component of the losses would be very significant.

The typical range of applications for air core reactors in power systems, where the calculation of winding power losses is of interest (sometimes mandatory), would be related to a range from DC and power frequencies up to a few thousands of Hertz. For this study the range selected was from 10^{-8} Hz, representing the DC component and 50 Hz for as the power frequency, up to 10000 Hz, with a frequency step of 50 Hz from the fundamental frequency up to the 60th harmonic order and with a frequency step of 500 Hz from 3000 to 10000 Hz. The calculation of the losses was performed using both analytical and the *ANSYS*[®] *Maxwell* embedded Eddy Current calculation method, here called FEA.

As explained in the item 2.2.2, the postprocessing of the losses calculation when using the *Litz Cable* feature of the FEA software is done considering the Equation 2.55, that is valid for low frequencies and when the magnetic field penetration is higher than the radius of the strand, which happens for very thin strands that is usually the case of that kind of cables (*Litz*).

For air core reactors, the thickness of the strands is usually higher than the ones found in *Litz Cable* and therefore it is expected that the calculation model mentioned above would not be proper for this study.

The 81 experiments were run and the percent deviations of the values of power losses between both methods are evidenced in Fig. 3.13 – 3.21. Nine experiments were chosen to be representative of the behavior of the total set of experiments, namely ACR1, ACR13, ACR25, ACR28, ACR40, ACR52, ACR55, ACR67 and ACR79. For lower frequencies, below 1 kHz the percent deviation of the winding power losses goes up to 50 % while for the higher ones, around 10 kHz, the percent deviation can reach up to 700 %.

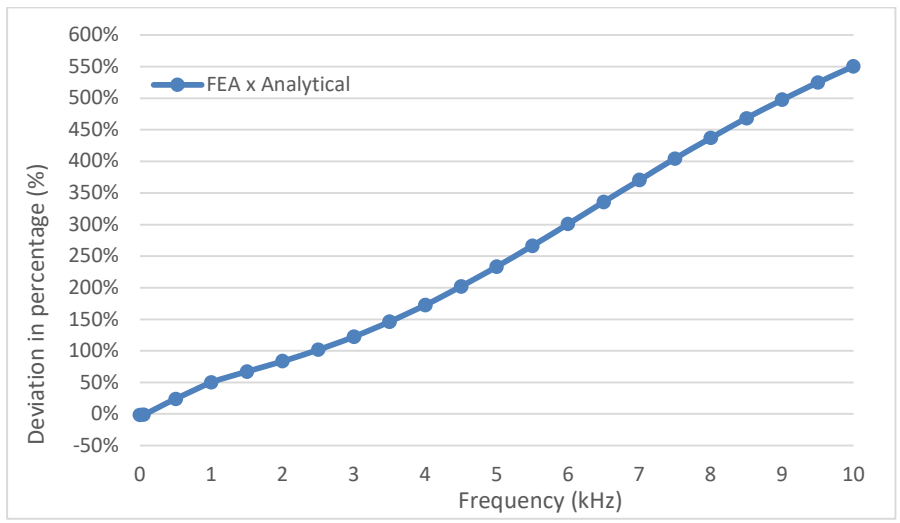


Figure 3.13 - Winding power losses percent deviation - FEA x Analytical - ACRI.

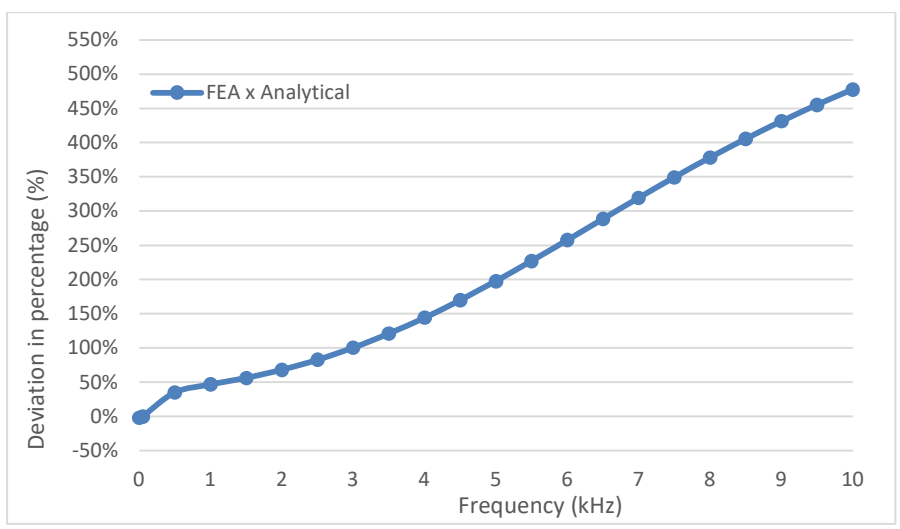


Figure 3.14 - Winding power losses percent deviation - FEA x Analytical - ACR13.

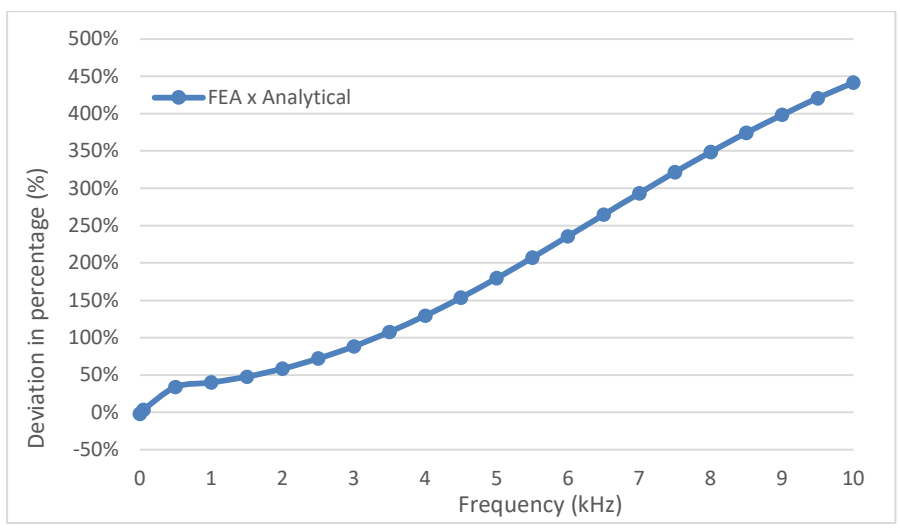


Figure 3.15 - Winding power losses percent deviation - FEA x Analytical - ACR25.

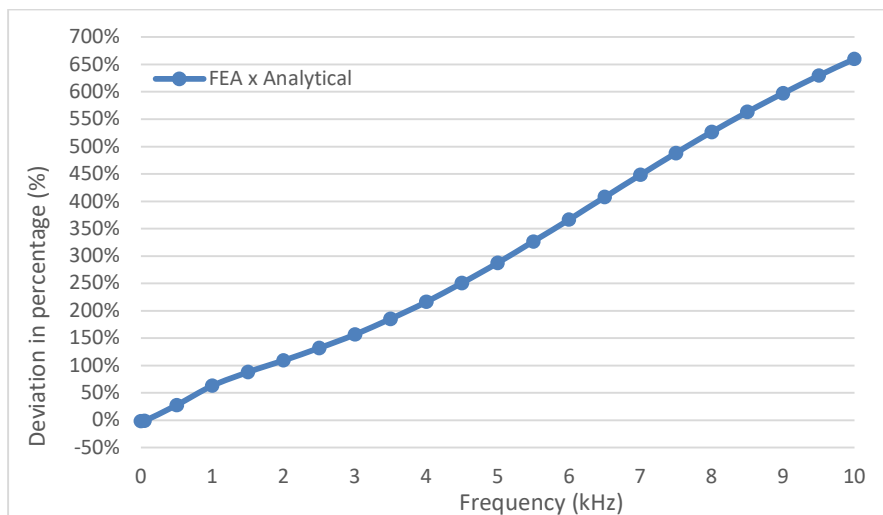


Figure 3.16 - Winding power losses percent deviation - FEA x Analytical - ACR28.

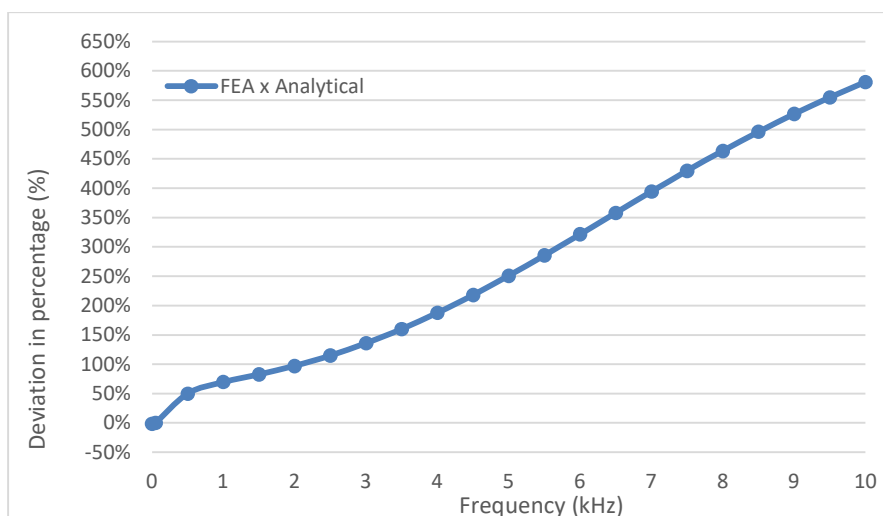


Figure 3.17 - Winding power losses percent deviation - FEA x Analytical - ACR40.

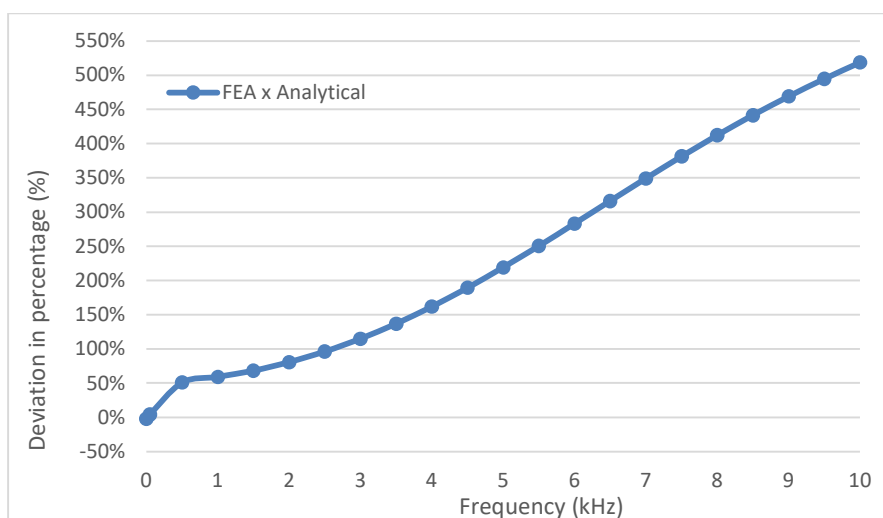


Figure 3.18 - Winding power losses percent deviation - FEA x Analytical - ACR52.

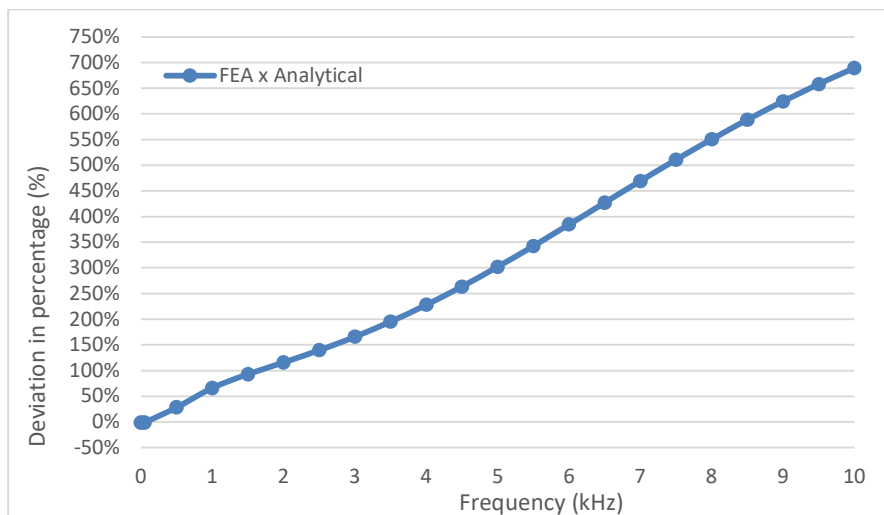


Figure 3.19 - Winding power losses percent deviation - FEA x Analytical - ACR55.

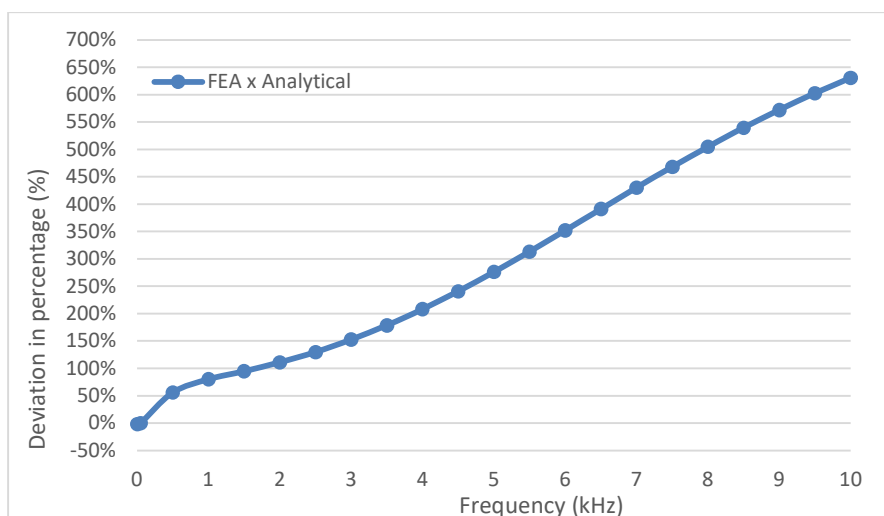


Figure 3.20 - Winding power losses percent deviation - FEA x Analytical - ACR67.

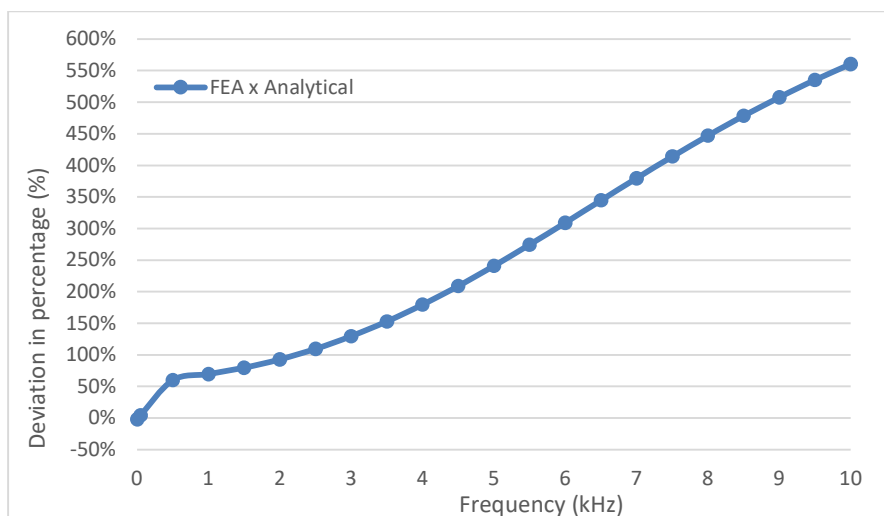


Figure 3.21 - Winding power losses percent deviation - FEA x Analytical - ACR79.

In the FEM software it is possible to add any type of mathematical operation to postprocess the results of the simulations. In other words, formulas could be added for example to calculate the DC losses, the skin, and the proximity effects, using the available geometries and the magnetic field distribution. To correct the DC losses to consider the stranding factor, the operator k_{str} was added in the Equation 3.1, which corresponds to the increase in the losses due to the longer length of the cable strands in comparison to the length of the cable.

$$P_{dc} = k_{str} \cdot \frac{4\pi \cdot D_{av} \cdot n}{N_{str} \cdot \pi \cdot D_{str}} \cdot i_t^2 \quad (3.1)$$

The formulas proposed by Ferreira for the calculation of the skin and proximity effect were also implemented in the postprocessing of the FEM software to correct the calculation of the total winding losses. The postprocessing panel of the Eddy Current solver of the ANSYS® Maxwell was adjusted to accommodate the formulas for the calculation of the total winding losses, accordingly, as can be seen in Fig. 3.22.

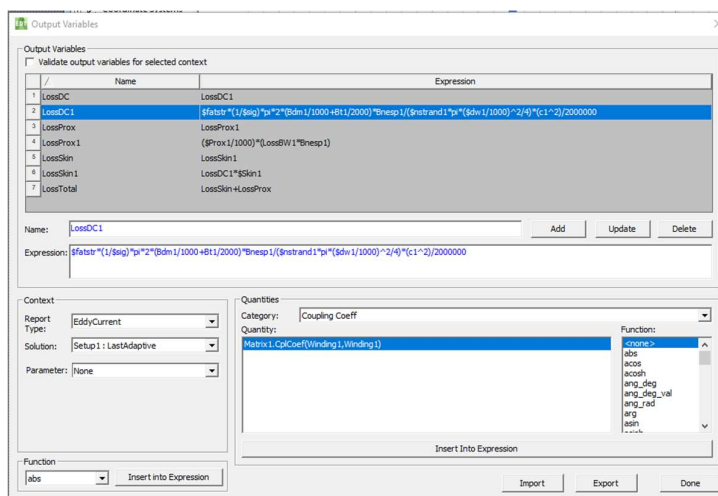


Figure 3.22 - Postprocessing panel of the Eddy Current Solver - ANSYS® Maxwell.

To obtain the information about the magnetic field distribution along the surface of the winding, to properly estimate the proximity effect on the losses, the postprocessing of the magnetic field strength H was performed by using the fields calculator available in the software as can be seen in Fig. 3.23. That information is later added to the postprocessing panel of the Eddy Current solver.

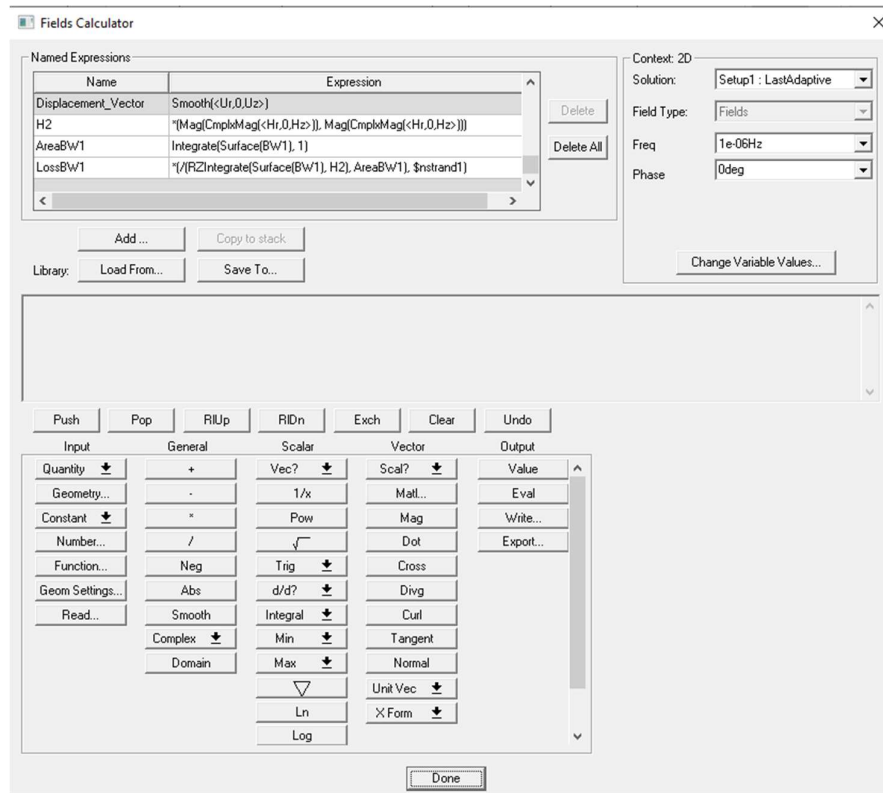


Figure 3.23 - Fields calculator in the Eddy Current Solver - ANSYS® Maxwell.

By doing this, the Ferreira's method would be completely simulated using the FEA software, also considering the stranding factor, here called FEA corrected. The comparison between the values of power losses obtained by the embedded losses calculation of the solver (FEA) and the corrected one, using the analytical model as the base reference, is illustrated in Fig. 3.24 - 32.

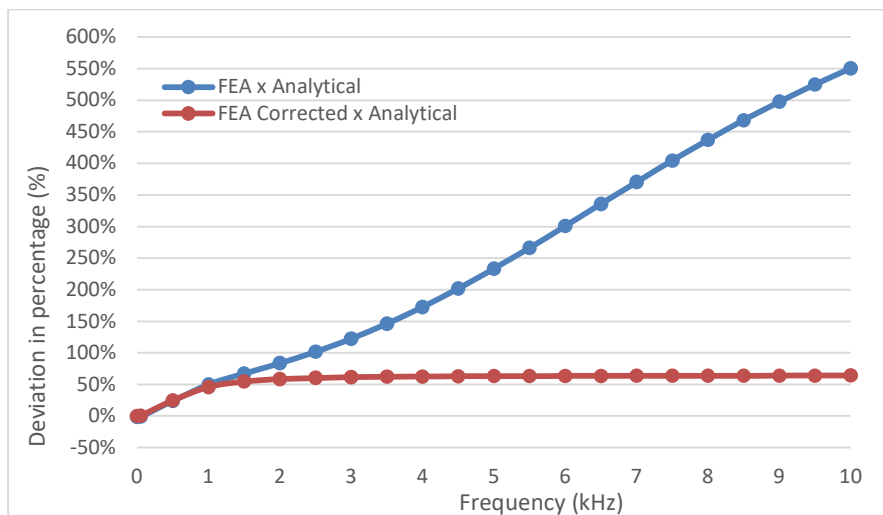


Figure 3.24 - Winding power losses percent deviation - FEA Corrected and FEA - ACRI1.

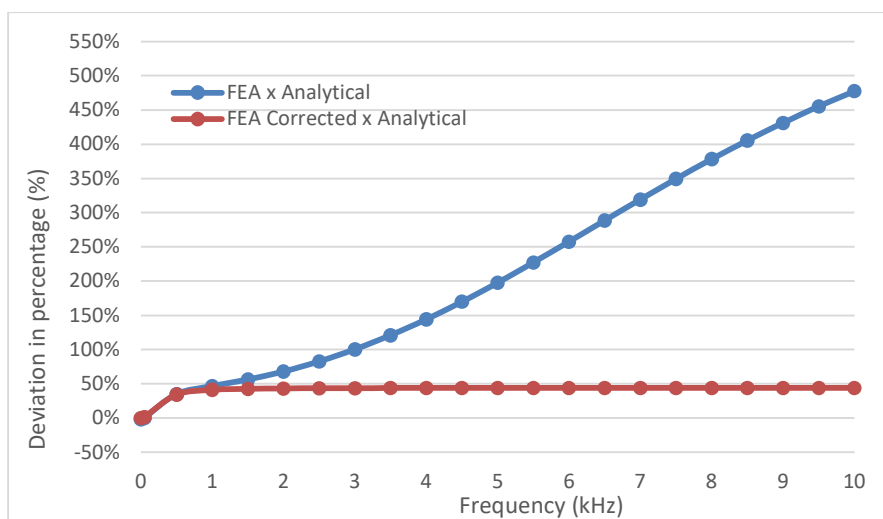


Figure 3.25 - Winding power losses percent deviation - FEA Corrected and FEA - ACR13.

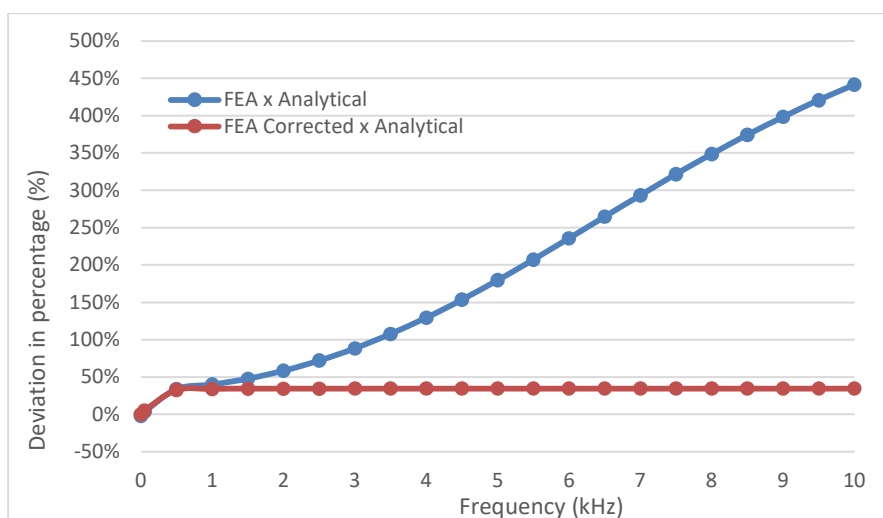


Figure 3.26 - Winding power losses percent deviation - FEA Corrected and FEA - ACR25.

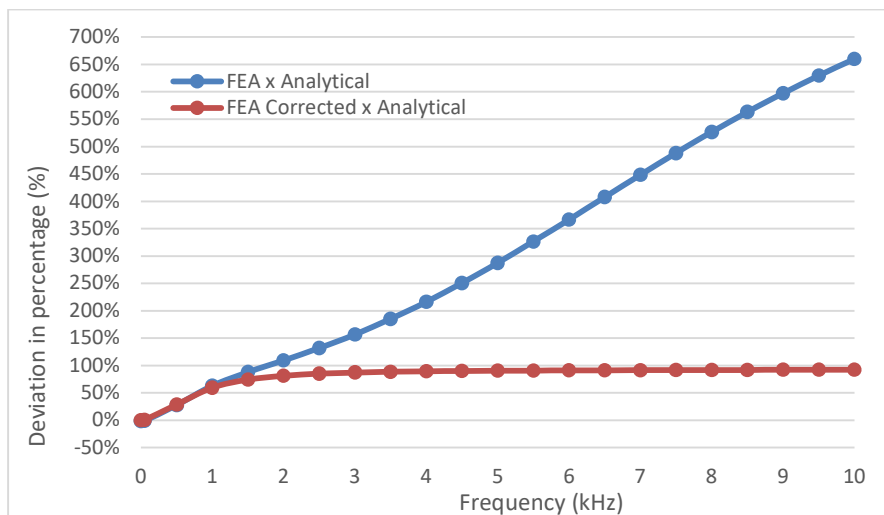


Figure 3.27 - Winding power losses percent deviation - FEA Corrected and FEA - ACR28.

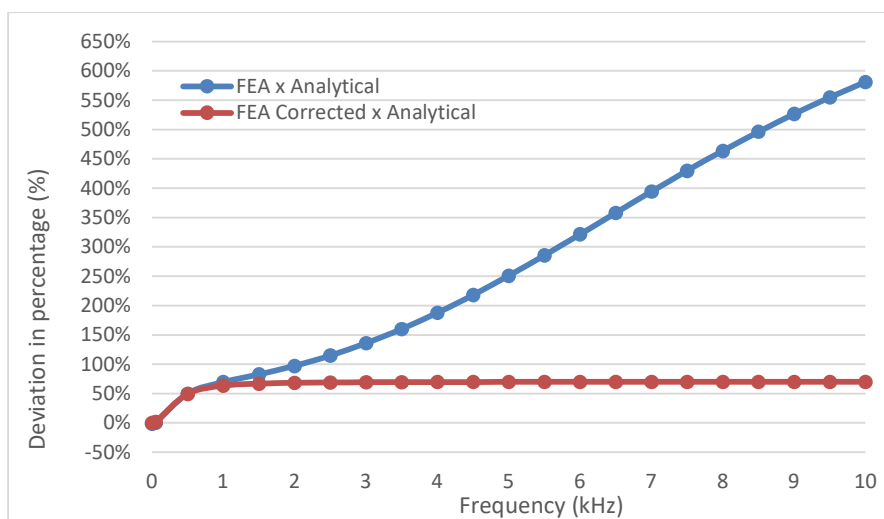


Figure 3.28 - Winding power losses percent deviation - FEA Corrected and FEA - ACR40.

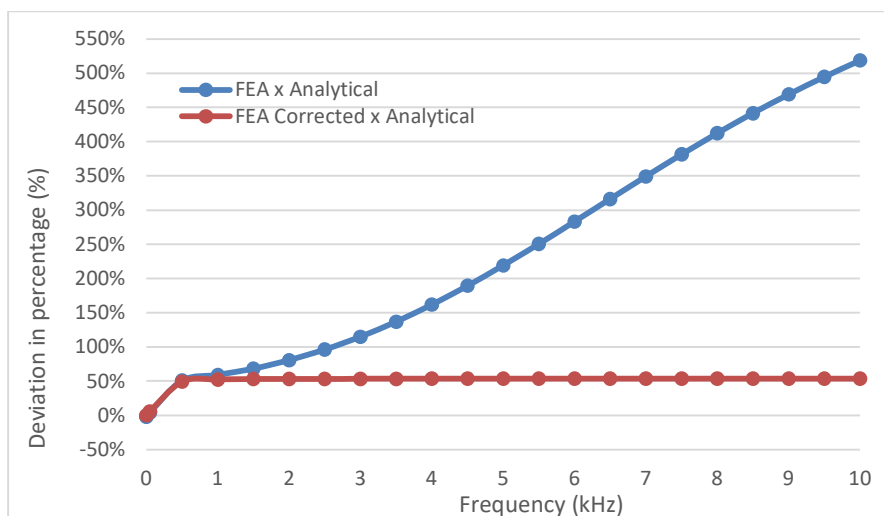


Figure 3.29 - Winding power losses percent deviation - FEA Corrected and FEA - ACR52.

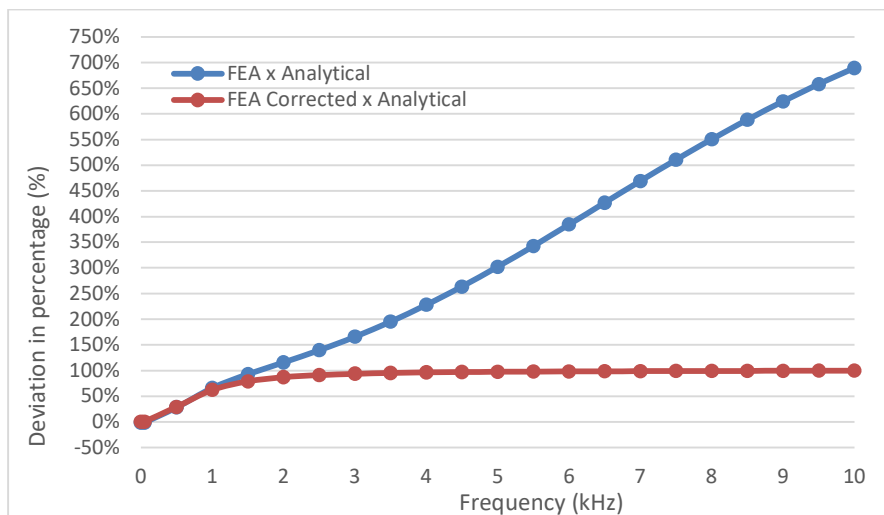


Figure 3.30 - Winding power losses percent deviation - FEA Corrected and FEA - ACR55.

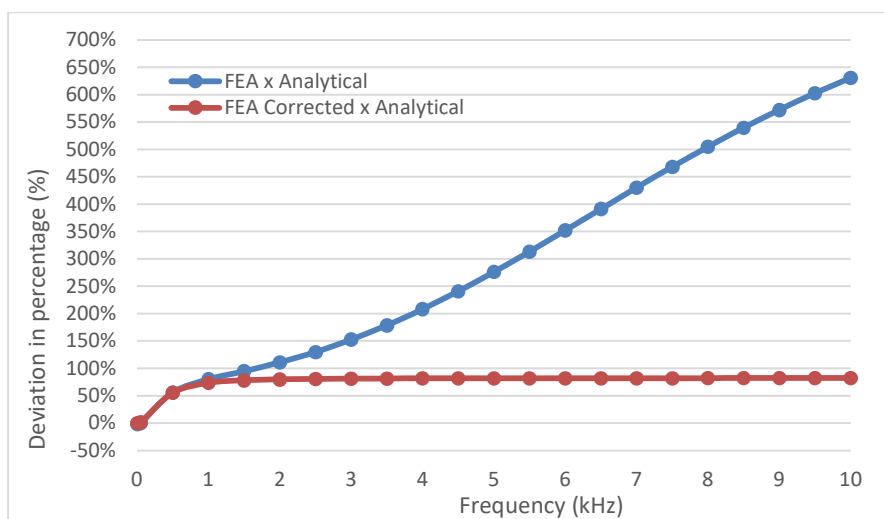


Figure 3.31 - Winding power losses percent deviation - FEA Corrected and FEA - ACR67.

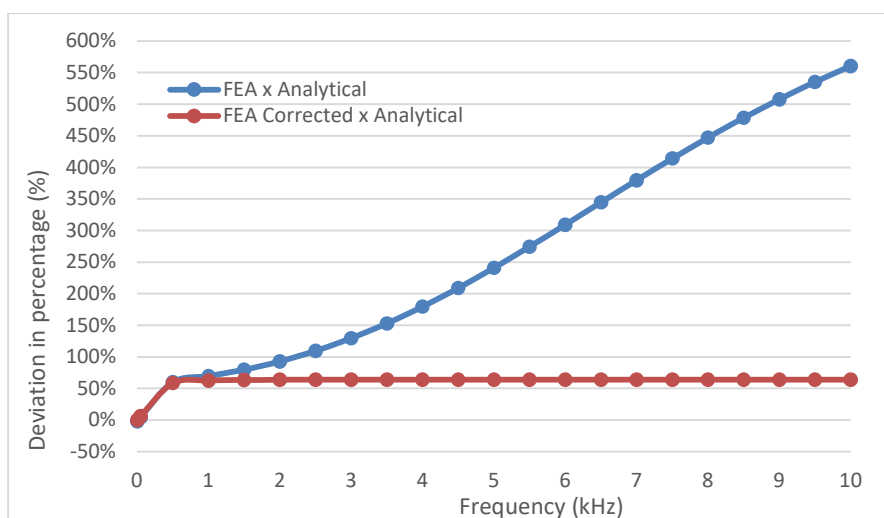


Figure 3.32 - Winding power losses percent deviation - FEA Corrected and FEA - ACR79.

When the correction was applied to the calculation of the winding power losses the error in the higher frequencies was mitigated as expected from the Ferreira's method. The behavior of the percent deviations changed significantly as well. Before, the percent deviation increased with the increase of the frequency. Now, the percent deviation increases for frequencies up to 1 kHz and remain constant beyond that point. Considering that the winding power losses generated by the proximity effect prevails among the others as the frequency increases, it would be possible to infer that the discrepancies between the analytical model, which also applies the Ferreira's method, and the FEA corrected would be mostly related to the proximity effect. For that reason, a split was done, and the losses related to the proximity effect were extracted from the FEA corrected model, as shown in Fig. 3.33 – 3.41.

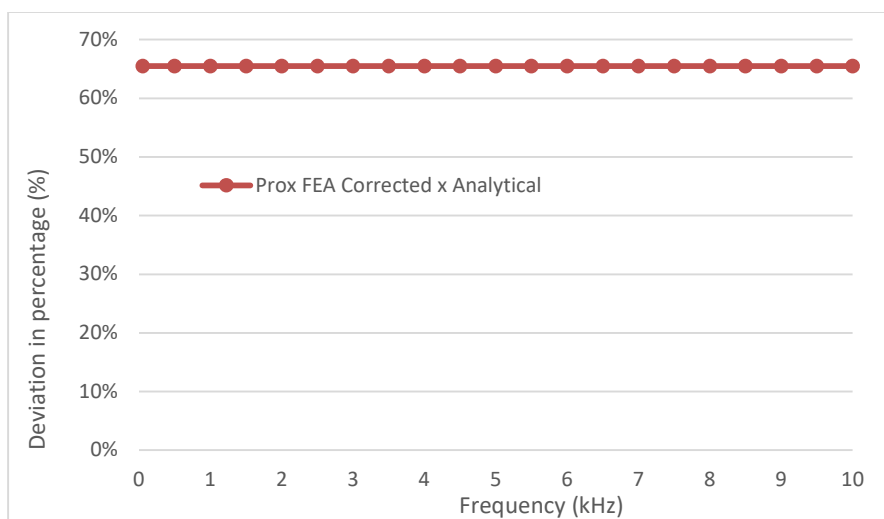


Figure 3.33 - Winding proximity effect losses - FEA Corrected x Analytical - ACR1.

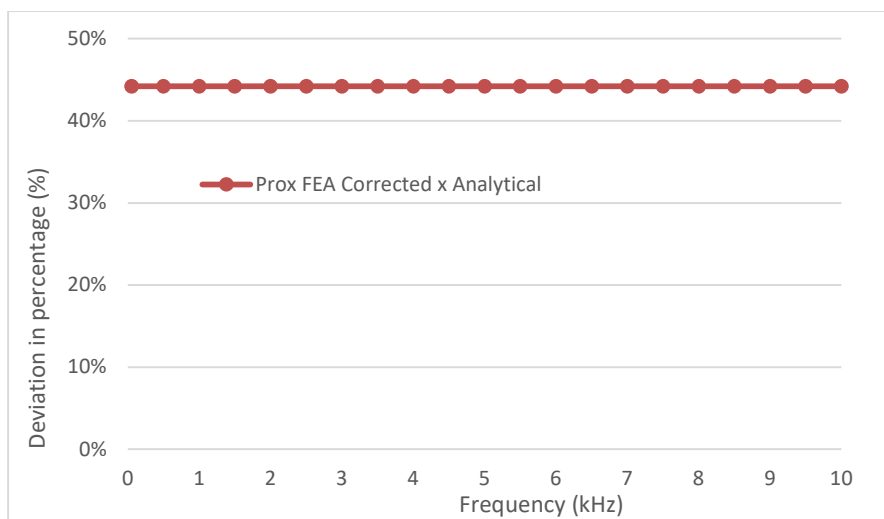


Figure 3.34 - Winding proximity effect losses - FEA Corrected x Analytical - ACR13.

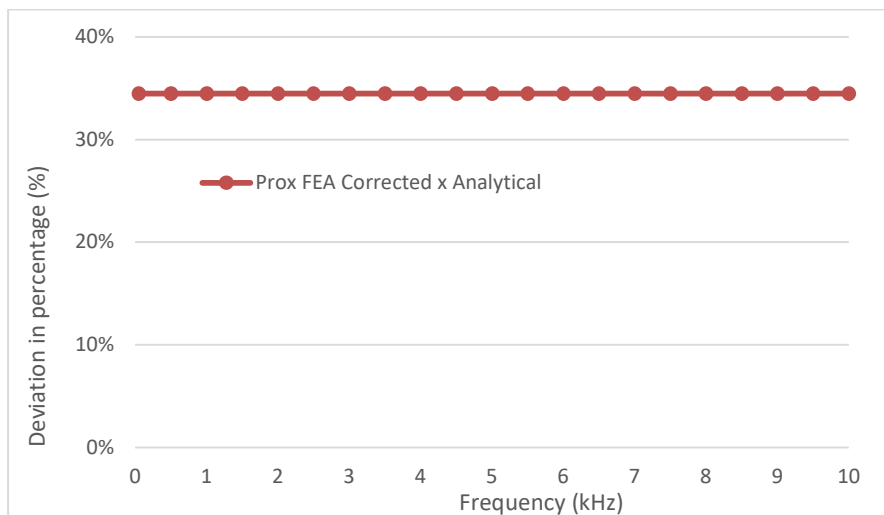


Figure 3.35 - Winding proximity effect losses - FEA Corrected x Analytical - ACR25.

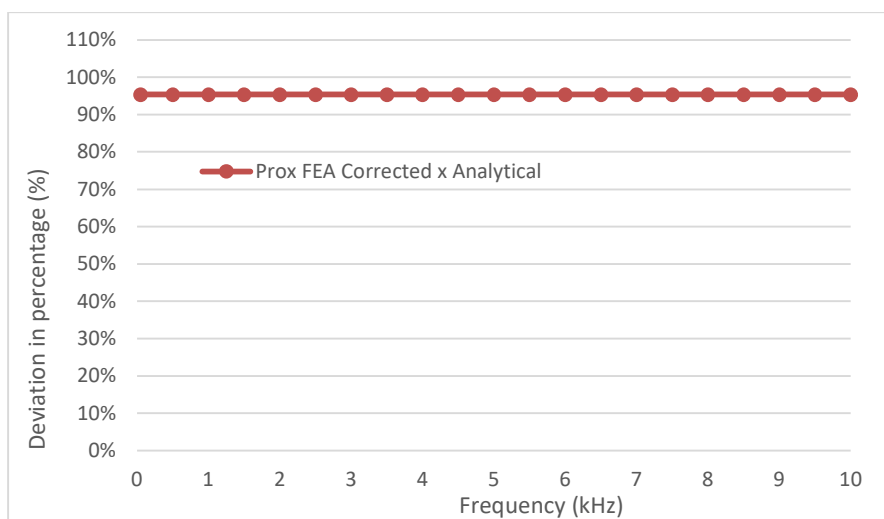


Figure 3.36 - Winding proximity effect losses - FEA Corrected x Analytical - ACR28.

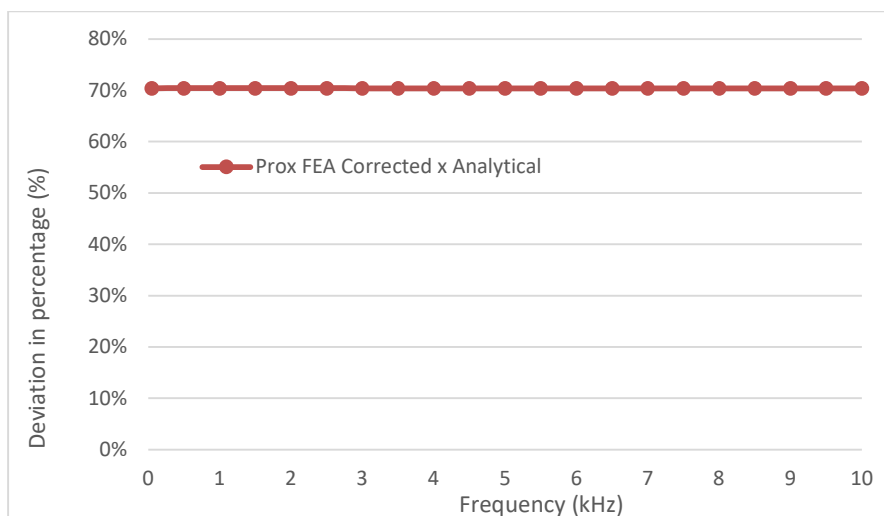


Figure 3.37 - Winding proximity effect losses - FEA Corrected x Analytical - ACR40.

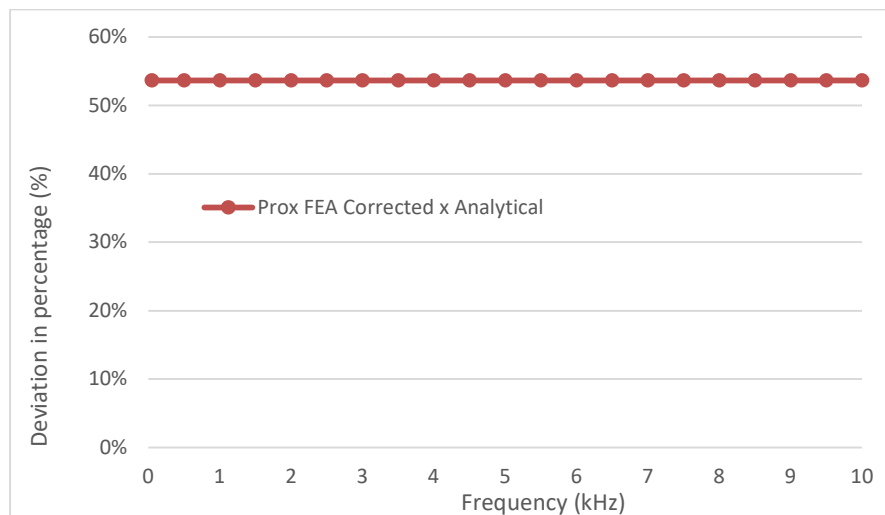


Figure 3.38 - Winding proximity effect losses - FEA Corrected x Analytical - ACR52.

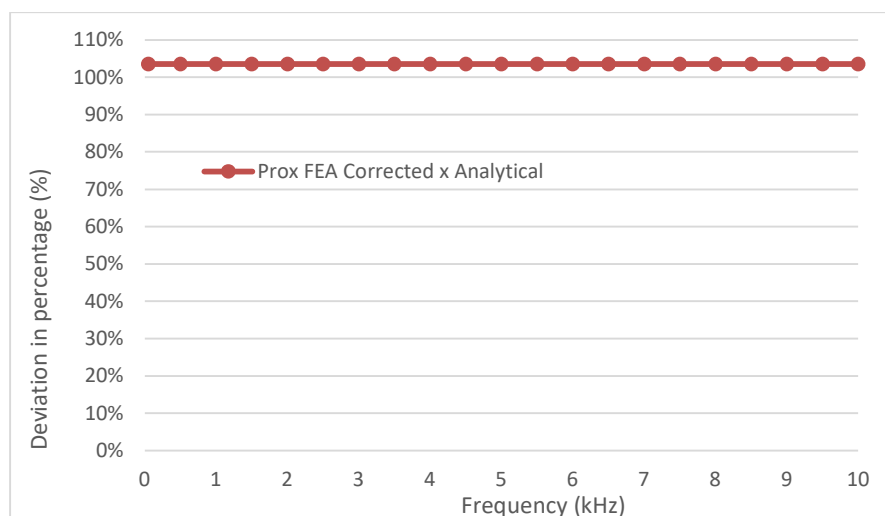


Figure 3.39 - Winding proximity effect losses - FEA Corrected x Analytical - ACR55.

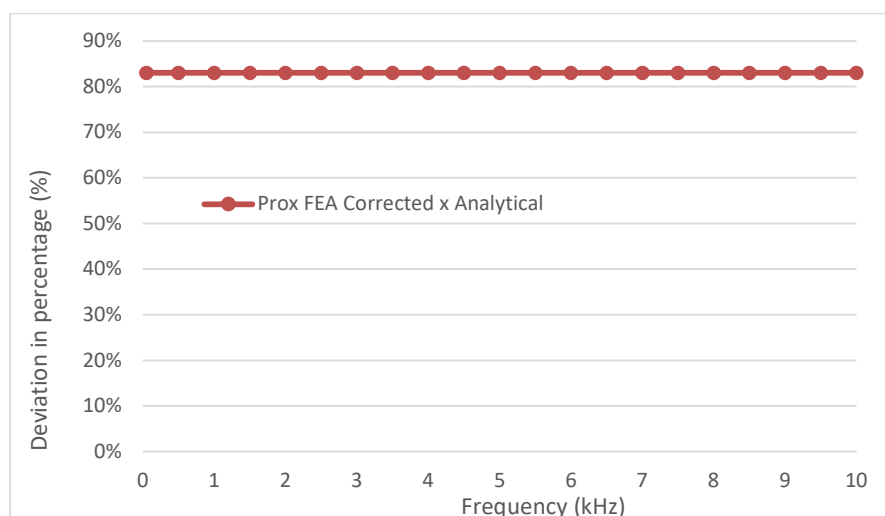


Figure 3.40 - Winding proximity effect losses - FEA Corrected x Analytical - ACR67.

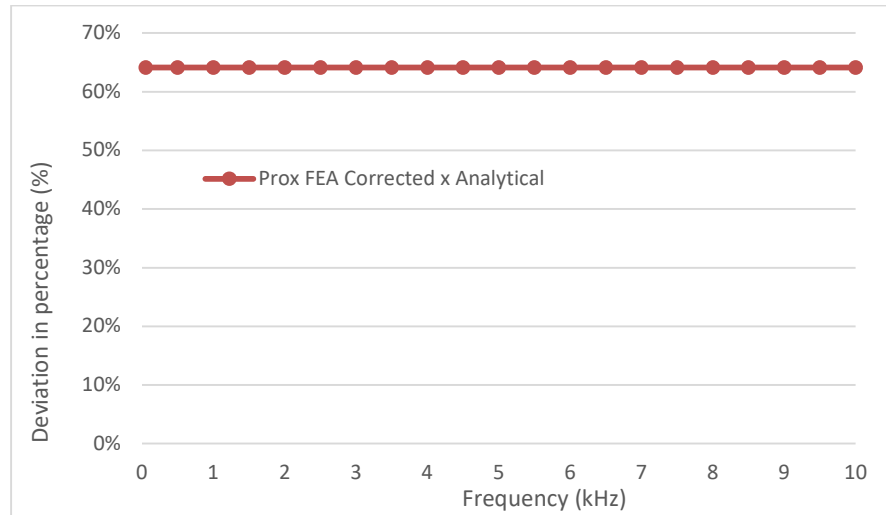


Figure 3.41 - Winding proximity effect losses - FEA Corrected x Analytical - ACR79.

Analyzing only the winding losses generated by the proximity effect calculated by the FEA corrected model in comparison to the analytical model, it is evidenced that the percent deviations in the total power losses values, previously shown in Fig. 3.24 – 3.32, are basically related to that effect. That behavior was also noticed in the remaining experiments.

3.5 Comparison between analytical and finite element models

From the information available in Fig. 3.24 – 3.32 it is possible to infer that there is an intrinsic and constant percent deviation in the calculation of the losses generated by the proximity effect, coming from FEA corrected model and the analytical model. That percent deviation shifts when the design parameters of the ACRs are changed, suggesting that those changes affect the accuracy of the analytical model. The percent deviations of the winding losses related to the proximity effect, between the FEA corrected model and the analytical model for the 81 experiments are summarized in Table 3.4. To statistically deal with the data, it is a good practice to avoid large discrepancies in the magnitude of the variable under analysis. For that reason, the effects are analyzed in terms of the percentage of their deviation.

Table 3.4 - Proximity effect losses percent deviation between FEA corrected and analytical model.

Reference	% Proximity effect losses deviation	Reference	% Proximity effect losses deviation	Reference	% Proximity effect losses deviation
ACR1	65.5	ACR28	95.4	ACR55	103.6
ACR2	67.7	ACR29	98.3	ACR56	106.3
ACR3	70.4	ACR30	100.9	ACR57	109.3
ACR4	58.6	ACR31	86.1	ACR58	93.5
ACR5	62.4	ACR32	91.3	ACR59	99.0
ACR6	67.0	ACR33	97.3	ACR60	105.5
ACR7	47.2	ACR34	71.0	ACR61	77.2
ACR8	53.5	ACR35	79.3	ACR62	86.1
ACR9	61.1	ACR36	89.6	ACR63	97.3
ACR10	47.0	ACR37	73.4	ACR64	86.4
ACR11	47.8	ACR38	74.3	ACR65	87.5
ACR12	48.9	ACR39	74.0	ACR66	87.0
ACR13	44.2	ACR40	70.4	ACR67	83.0
ACR14	45.7	ACR41	71.9	ACR68	84.8
ACR15	47.5	ACR42	73.9	ACR69	86.9
ACR16	39.1	ACR43	65.2	ACR70	77.2
ACR17	42.0	ACR44	68.1	ACR71	80.5
ACR18	45.3	ACR45	71.5	ACR72	84.3
ACR19	40.5	ACR46	58.1	ACR73	68.8
ACR20	41.1	ACR47	58.5	ACR74	69.3
ACR21	41.7	ACR48	58.6	ACR75	69.1
ACR22	38.4	ACR49	56.5	ACR76	67.1
ACR23	39.6	ACR50	57.4	ACR77	68.1
ACR24	40.9	ACR51	58.4	ACR78	69.1
ACR25	34.5	ACR52	53.6	ACR79	64.1
ACR26	36.7	ACR53	55.3	ACR80	65.8
ACR27	39.2	ACR54	57.1	ACR81	67.8

A graphical analysis can be applied to the results of the experiments to verify the existence of possible lurking variables that may be introducing errors in the analysis, to check if there is any formation of clusters, mixtures, oscillations, and trends. That grouped information is available in the run chart in Fig. 3.42

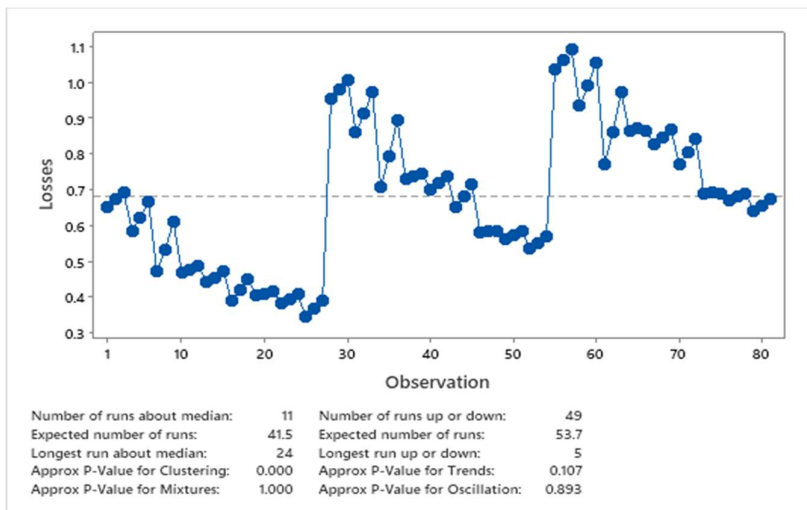


Figure 3.42 - Run chart losses - proximity effect - FEA corrected x Analytical model.

From the evaluation of the run chart and the P-values presented in Fig. 3.42 three major clusters can be observed, each one presenting similar trend, which would explain the low P-value (below 0.05) for clustering and for trends, as the null hypothesis would be that there are no clusters, no trends, no mixtures and no oscillations.

Observing the data from Table 3.4 and Fig. 3.42 it is possible to say that the error between the models increase as the average diameter of the winding increases, considering that the first cluster goes from the experiment 1 to 27, that are related to the low level of the D_{av} design parameter, the second cluster goes from 28 to 54, being related to the medium level of the D_{av} and the remaining experiments would be linked to the high level of the D_{av} . Analogously, the height of the winding also seems to have a big impact on the agreement between the models, however in this case the effect seems to be in order to reduce the susceptibility of the accuracy of the model to vary significantly when other design parameters change. This can be observed in the experiments from ACR7 to ACR9 and ACR10 to ACR12, where the difference between ACR7 and ACR10, ACR8 and ACR11, and ACR9 and ACR12 is basically the height of the winding (H_w that shifts from the low level to the medium and high levels).

To verify those assumptions and look for other possible understandings, the pareto chart provided in Fig. 3.43 would be a proper tool to quantitatively represent the impact of the changes of the design parameters on the accuracy between the models.

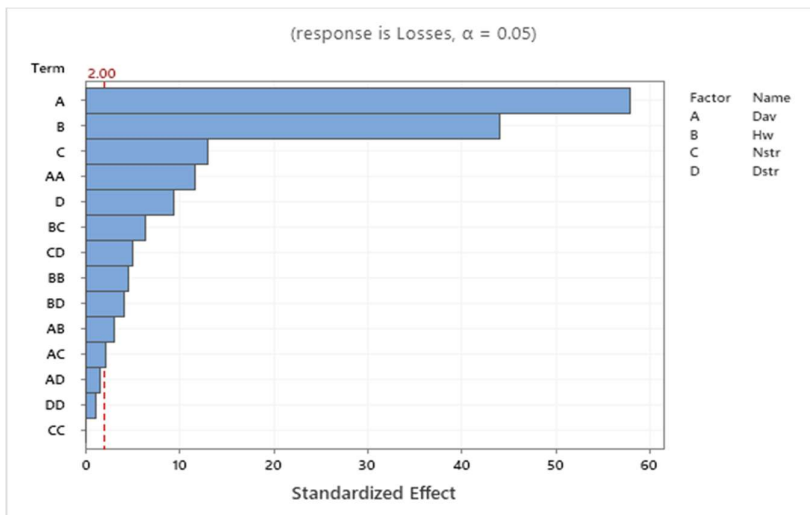


Figure 3.43 - Pareto chart of the impact of the changes in the experiments.

The chart evidences the influence of the change of the design parameters of the windings on the accuracy of the FEA corrected to the analytical model. Where, as expected, the winding diameter has a major contribution to that effect, as well as the winding height followed by the number of strands and the diameter of the strands. The effects of the square (e.g. AA, BB) and two-way (e.g. AB, AC) interactions of changes in the design parameters are in general of a minor relevance compared to the main effects. From that is also expected that the cubic and three-way interactions, which means evaluating the change of three design parameters simultaneously would not be significant to the study. The main effects plot can be seen in Fig. 3.44.

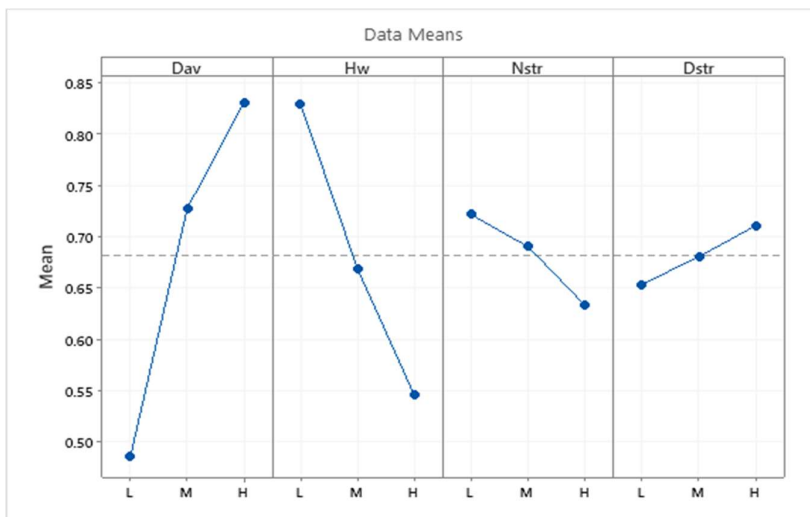


Figure 3.44 - Effect of the change of the main design characteristics on the model accuracy.

The two-way interactions effects of the design parameters changes can be observed in Fig. 3.45. In the early stages of the development of this study the main effects and the interaction plots were used as a sanity check for the suitability of the approach. Once some specific behaviors are expected for each change on the experiments, it would be easier to identify the outliers and that would help when looking for lurking variables.

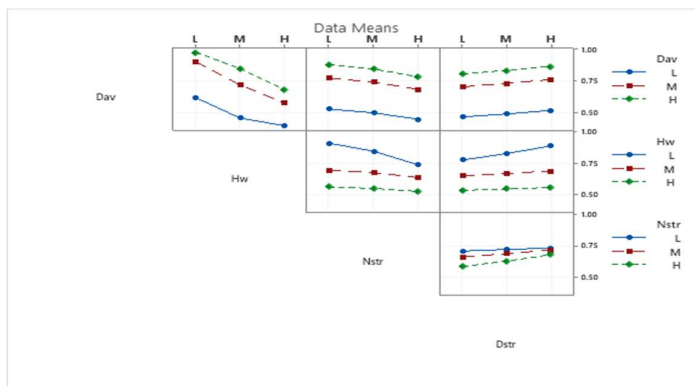


Figure 3.45 - Two-way interactions - Design parameters changes effects on the model accuracy.

It is known from the literature that the ratio between the winding height and the winding average diameter, called α ratio, is an important parameter in the distribution of the flux lines for windings with no magnetic core. That ratio also has influence on the direction of the magnetic field intensity vector. To exemplify that behavior, it would be possible to consider the experiments ACR1 and ACR55, for which the design parameters are the same except the D_{av} . The ACR1 is set for a low level of D_{av} , while the ACR55 is at a high level for the same parameter. In other words, the α ratio of the first is higher than the second. Fig. 3.46 and 3.47 provide information about the vectorial distribution of the magnetic field for the two experiments mentioned earlier. For the ACR1, the direction of distribution of the magnetic field is mostly concentrated in the Z axis, while for the ACR55 there is an important portion of that distribution pointing in the direction of the X axis. That will lead to a more uniform distribution of the magnetic field inside the winding of ACR1 than of the ACR55. Remembering from section 2.2.2 that the known analytical models for the calculation of the eddy currents usually consider an infinitesimally thin coil with uniform distribution of the magnetic field, it is expected that bigger discrepancies would be found when those models are applied for that type of calculation in windings where this distribution may not be uniform. That understanding agrees with the results of the percent discrepancies between the FEA corrected and the analytical model for the calculation of the proximity effect losses, once that discrepancy was around 63 % for ACR1 and 108 % for ACR55.

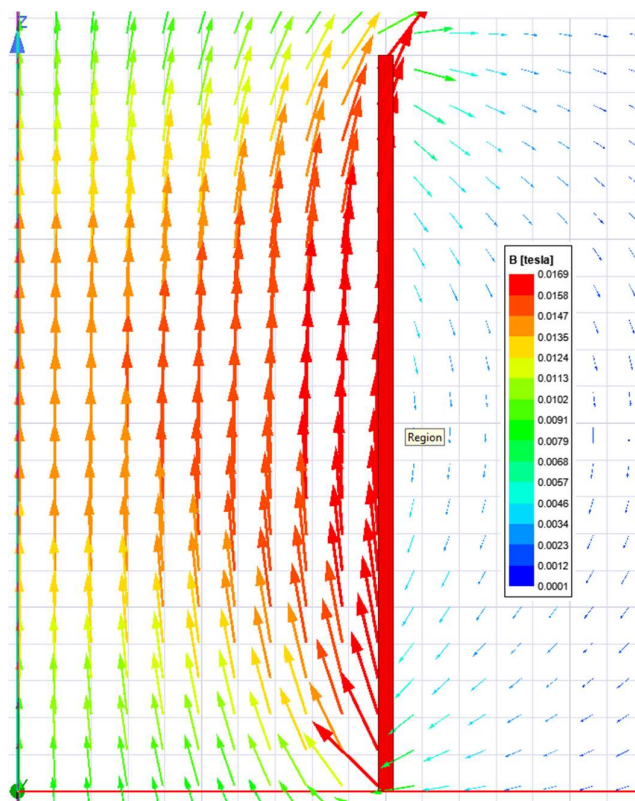


Figure 3.46 - Magnetic field distribution - ACR1.

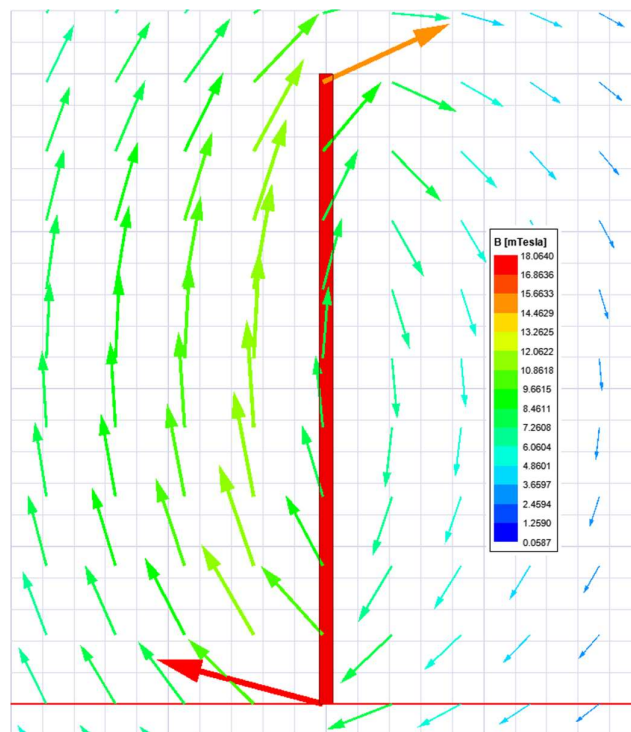


Figure 3.47 - Magnetic field distribution - ACR55.

3.6 Application of the response surface method

Once the differences between the models are identified as being mainly related to the distribution of the magnetic field through the sections of the windings and its uneven distribution within the winding cross section, this means that to increase the accuracy of the analytical model, it would be necessary to add more sections to the axial distribution of the losses and explore alternative corrections as mentioned in the literature to translate the effect of the magnetic field penetration in the radial direction of the cross section. For small windings that may be feasible and applicable. On the other hand, for large windings with thousands of turns, many concentric windings, and several harmonic currents to be analyzed, that may represent a significant computational effort, being sometimes also prevented by the numerical inconsistencies due to the discretization of the sections (numerical oscillations).

Considering the good agreement between the FEM and the analytical model for the inductance calculation, the more detailed distribution of the magnetic field provided by the FEM would also provide the proper correction to the analytical power losses calculation model, so this one would be improved without the cons mentioned earlier. That is possible by correcting the calculation of the winding losses due to the proximity effect with correction factors extracted from the response surface that best represent the percent discrepancies between the two models for the calculation of the losses due to the proximity effect. The response surface can be described by the Equation 3.2, which was extracted from the software *Minitab*[®] 19.2020.1.

$$\begin{aligned}
 l_n(Losses_{prox}) = & -0.6084 + 0.3150D_{av} - 0.1539H_w - 0.02662N_{str} + 0.0239D_{av} \\
 & - 0.03144D_{av} \cdot D_{av} + 0.00745H_w \cdot H_w - 0.000003N_{str} \cdot N_{str} \\
 & - 0.000627D_{str} \cdot D_{str} + 0.00454D_{av} \cdot H_w + 0.000943D_{av} \cdot N_{str} \\
 & - 0.001243D_{av} \cdot D_{str} + 0.002092H_w \cdot N_{str} - 0.002569H_w \cdot D_{str} \\
 & + 0.000919N_{str} \cdot D_{str}
 \end{aligned} \tag{3.2}$$

The best fit for the response surface was found by using the Box-Cox transformation with $\lambda = 0$, which leads the dataset to be transformed by the natural logarithm aiming for a normalization of the data. The R-squared value obtained is 98.93 %, indicating that almost all the data points can be described by the equation of the response surface.

In Fig. 3.48 – 3.53 the surface response of the two-way interactions of the design parameters are shown.

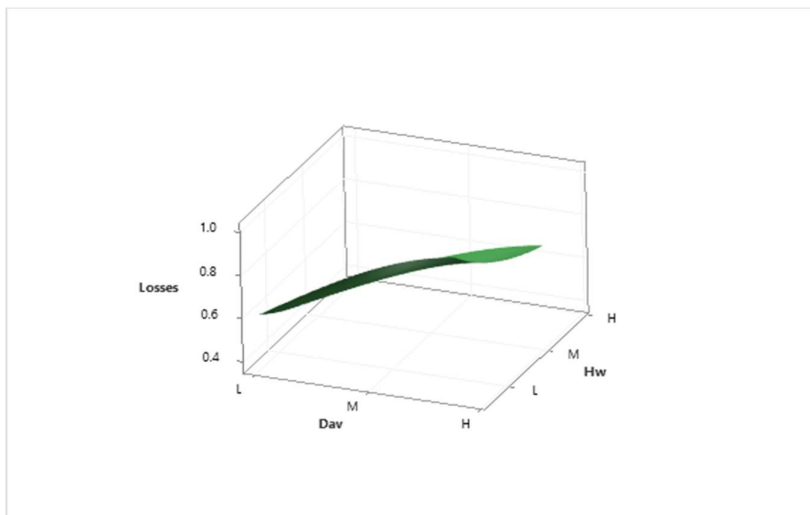


Figure 3.48 - Response surface - Proximity effect losses x Hw, Dav.

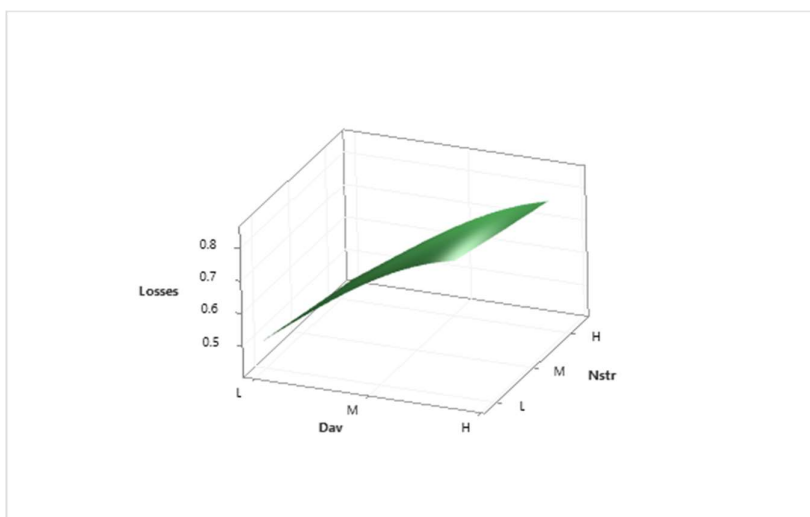


Figure 3.49 - Response surface - Proximity effect losses x Nstr, Dav.

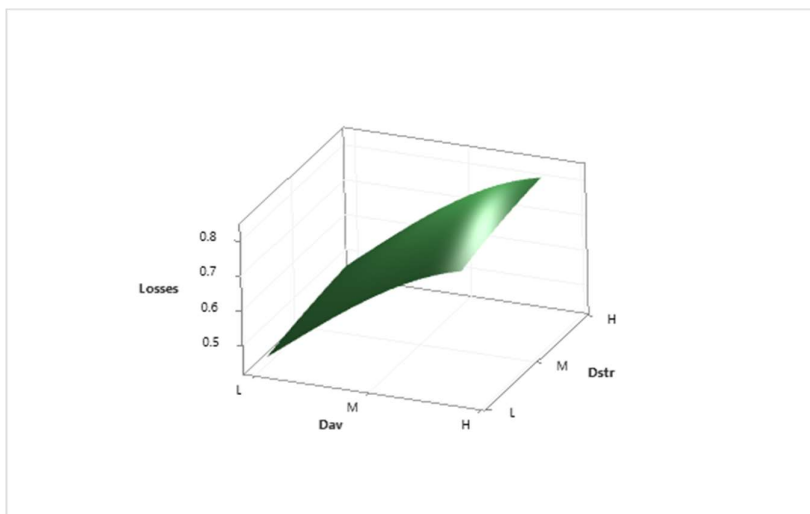


Figure 3.50 - Response surface - Proximity effect losses x Dstr, Dav.

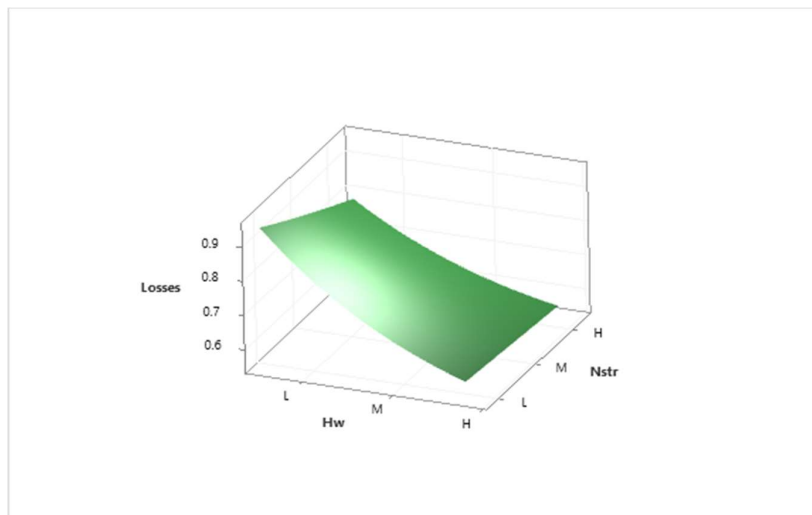


Figure 3.51 - Response surface - Proximity effect losses x Nstr, Hw.

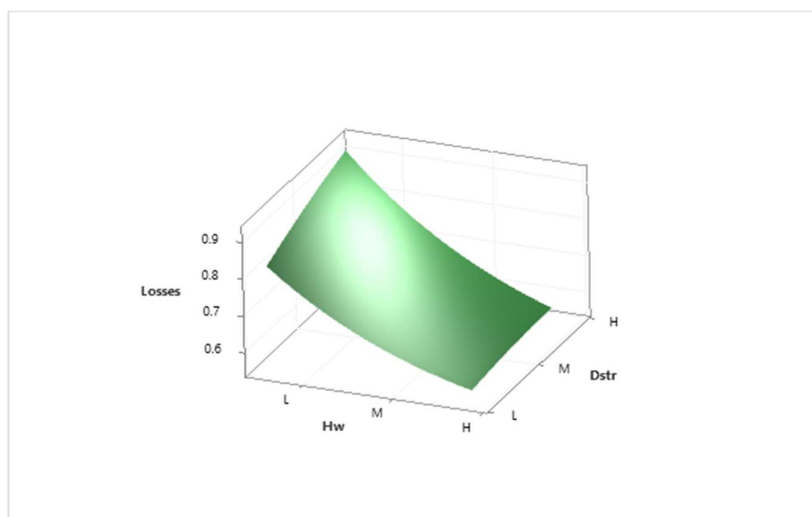


Figure 3.52 - Response surface - Proximity effect losses x Dstr, Hw.

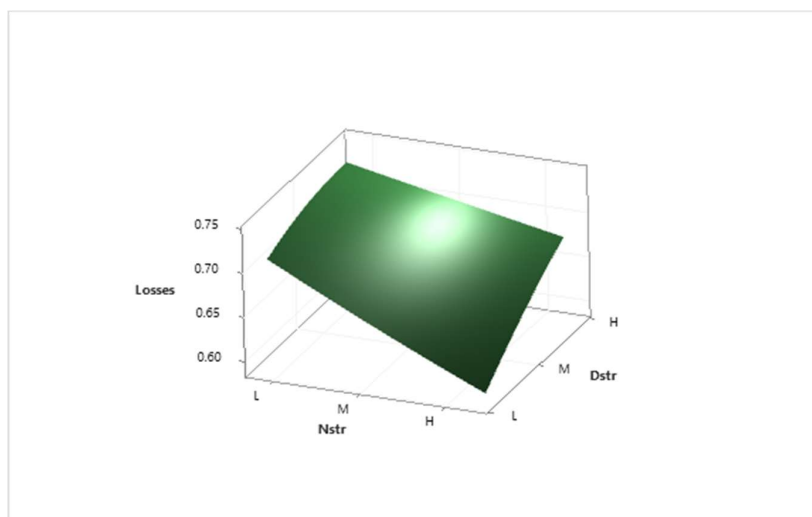


Figure 3.53 - Response surface - Proximity effect losses x Dstr, Nstr.

3.7 Analysis of total corrected power losses

The Equation 3.2 can be applied as a correction factor directly on the calculated values of the winding proximity effect losses, considering the main four design parameters of the ACRs. Table 3.5 provides the fitted values of the equation to the dataset and the residuals that would be the percent deviation between the results provided by the equation and the original values.

Table 3.5 - Fits and residuals for the response surface equation.

Reference	% Loss _{prox}	% Loss _{prox} - Fit	% Residual	Reference	% Loss _{prox}	% Loss _{prox} - Fit	% Residual
ACR1	65.5	63.2	-3.5	ACR42	73.9	74.4	0.6
ACR2	67.7	66.1	-2.3	ACR43	65.2	61.3	-6.0
ACR3	70.4	69.6	-1.2	ACR44	68.1	65.4	-4.0
ACR4	58.6	57.7	-1.5	ACR45	71.5	71.0	-0.8
ACR5	62.4	61.2	-1.9	ACR46	58.1	59.9	3.0
ACR6	67.0	65.9	-1.6	ACR47	58.5	60.1	2.8
ACR7	47.2	48.1	1.9	ACR48	58.6	59.0	0.7
ACR8	53.5	52.5	-1.9	ACR49	56.5	57.9	2.4
ACR9	61.1	59.2	-3.2	ACR50	57.4	58.9	2.5
ACR10	47.0	49.2	4.8	ACR51	58.4	59.1	1.3
ACR11	47.8	50.8	6.3	ACR52	53.6	54.1	0.8
ACR12	48.9	52.1	6.6	ACR53	55.3	56.5	2.3
ACR13	44.2	45.9	3.9	ACR54	57.1	59.4	4.0
ACR14	45.7	48.0	5.0	ACR55	103.6	104.5	0.9
ACR15	47.5	50.4	6.0	ACR56	106.3	108.0	1.6
ACR16	39.1	39.9	2.1	ACR57	109.3	111.2	1.8
ACR17	42.0	42.9	2.2	ACR58	93.5	97.1	3.8
ACR18	45.3	47.2	4.2	ACR59	99.0	101.7	2.7
ACR19	40.5	39.2	-3.1	ACR60	105.5	107.2	1.5
ACR20	41.1	39.7	-3.4	ACR61	77.2	83.7	8.4
ACR21	41.7	39.4	-5.5	ACR62	86.1	90.1	4.6
ACR22	38.4	37.6	-2.2	ACR63	97.3	99.4	2.2
ACR23	39.6	38.5	-2.8	ACR64	86.4	84.1	-2.6
ACR24	40.9	39.1	-4.3	ACR65	87.5	85.6	-2.2
ACR25	34.5	34.4	-0.2	ACR66	87.0	85.9	-1.3
ACR26	36.7	36.3	-1.2	ACR67	83.0	79.8	-3.9
ACR27	39.2	38.6	-1.5	ACR68	84.8	82.3	-2.9
ACR28	95.4	92.6	-2.9	ACR69	86.9	84.5	-2.8
ACR29	98.3	96.2	-2.1	ACR70	77.2	71.7	-7.1
ACR30	100.9	100.0	-1.0	ACR71	80.5	76.0	-5.5
ACR31	86.1	85.4	-0.8	ACR72	84.3	81.8	-3.0
ACR32	91.3	89.9	-1.5	ACR73	68.8	69.7	1.3
ACR33	97.3	95.6	-1.7	ACR74	69.3	69.6	0.4
ACR34	71.0	72.5	2.1	ACR75	69.1	67.7	-2.1
ACR35	79.3	78.6	-1.0	ACR76	67.1	67.9	1.2
ACR36	89.6	87.5	-2.3	ACR77	68.1	68.7	0.9
ACR37	73.4	73.5	0.1	ACR78	69.1	68.3	-1.2

ACR38	74.3	75.2	1.2	ACR79	64.1	64.3	0.3
ACR39	74.0	76.2	2.9	ACR80	65.8	66.9	1.6
ACR40	70.4	69.2	-1.7	ACR81	67.8	69.6	2.7
ACR41	71.9	71.8	-0.2				

Proceeding analogously to the analysis of Fig. 3.42, the run chart of the best fits of the Equation 3.2 can be plotted, Fig. 3.54. The behavior is very similar to the former from section 3.3, evidencing that there are still well marked clusters and trends for the same reasons earlier explained.

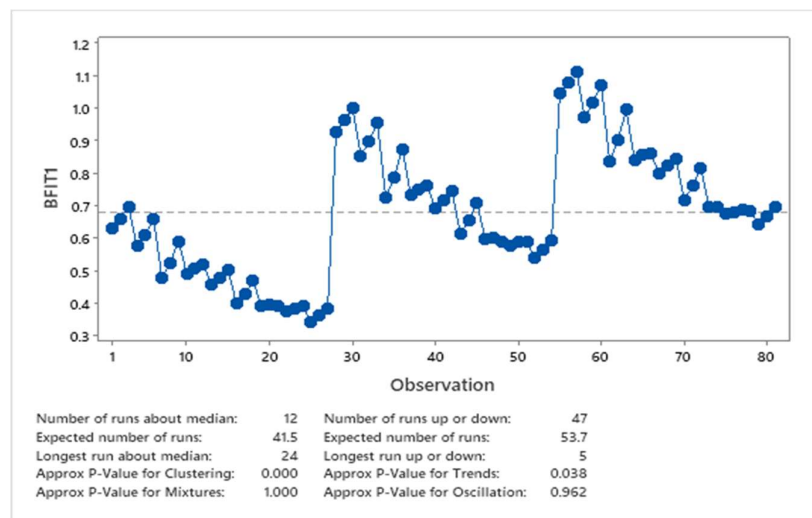


Figure 3.54 - Run chart losses - proximity effect - Analytical Corrected x Analytical model.

Applying the correction factors to the calculation of the winding proximity effect losses in the analytical model would bring the results of both models to be very similar. This can be seen throughout Fig. 3.55 – 3.63.

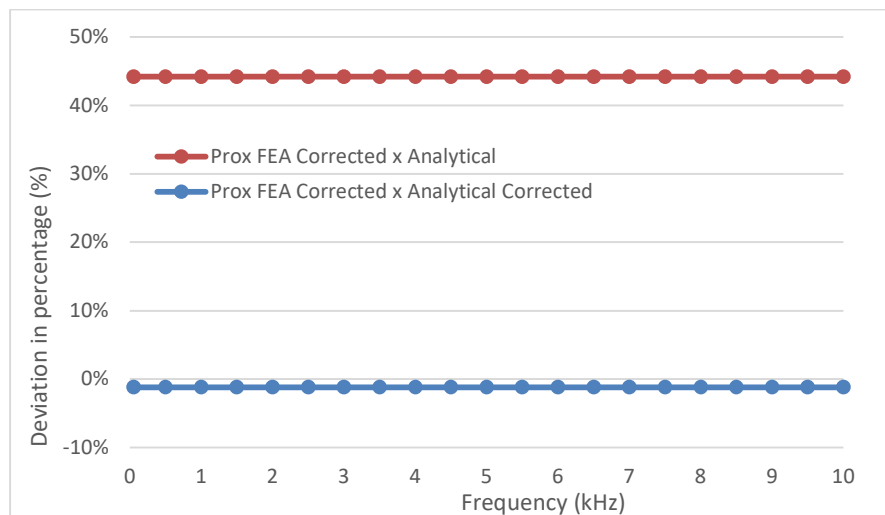


Figure 3.55 - Winding proximity effect losses - FEA Corrected x Analytical Corrected - ACRI.

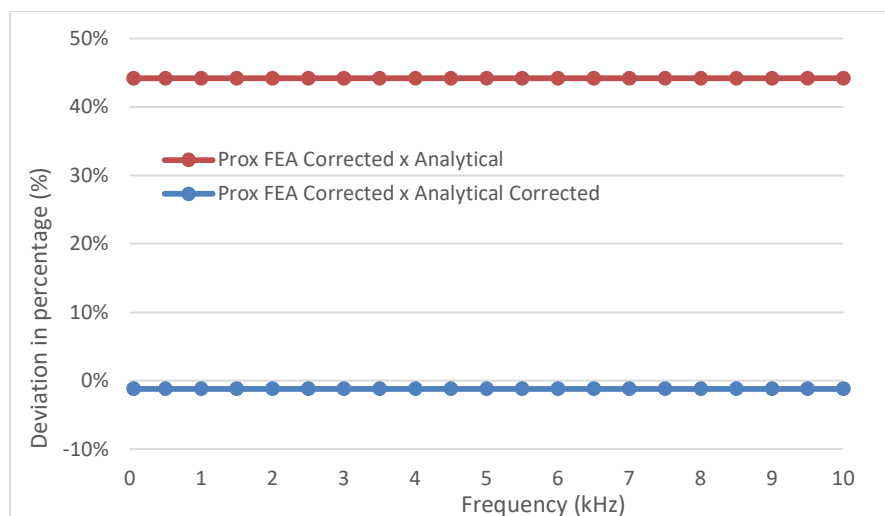


Figure 3.56 - Winding proximity effect losses - FEA Corrected x Analytical Corrected - ACR13.

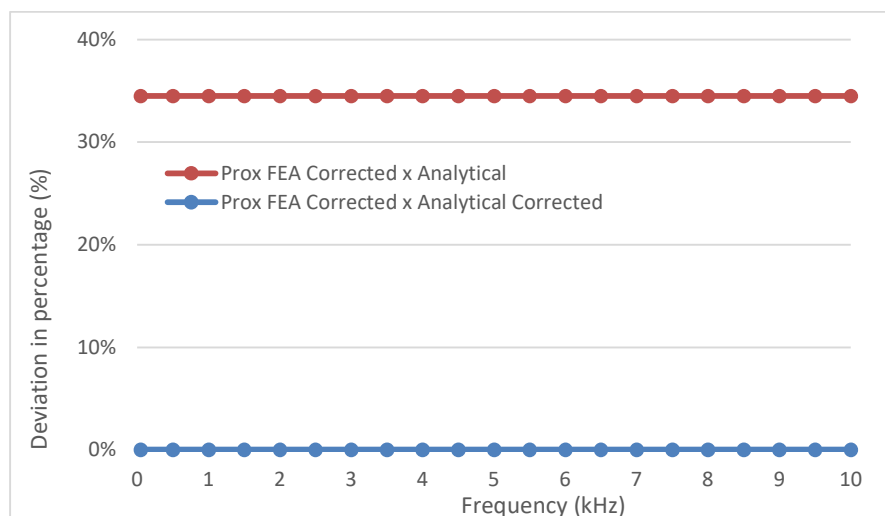


Figure 3.57 - Winding proximity effect losses - FEA Corrected x Analytical Corrected - ACR25.

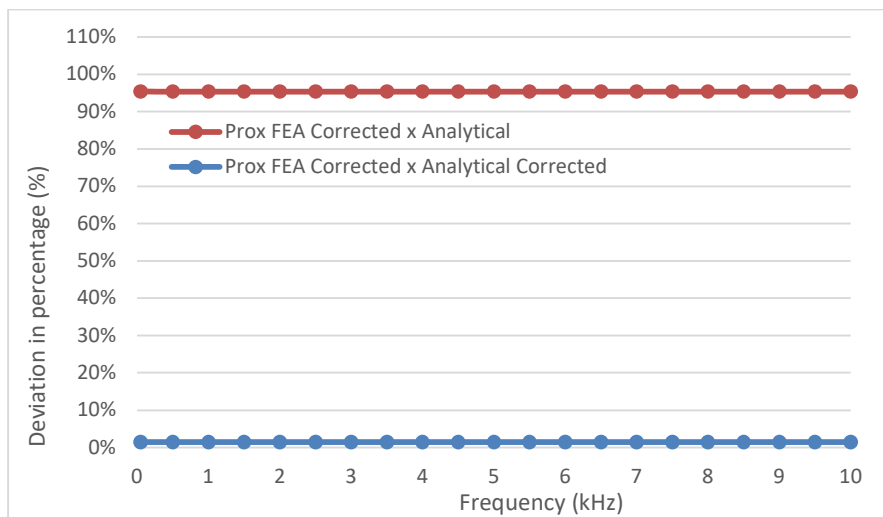


Figure 3.58 - Winding proximity effect losses - FEA Corrected x Analytical Corrected - ACR28.

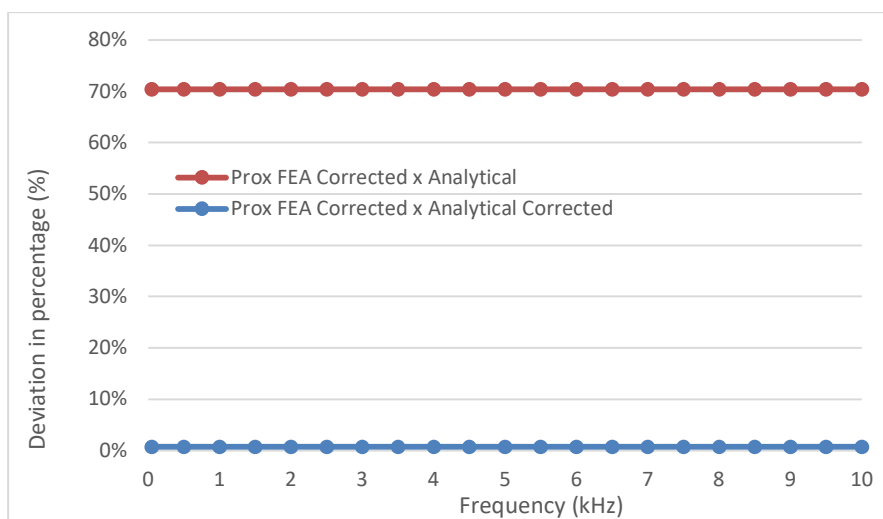


Figure 3.59 - Winding proximity effect losses - FEA Corrected x Analytical Corrected - ACR40.

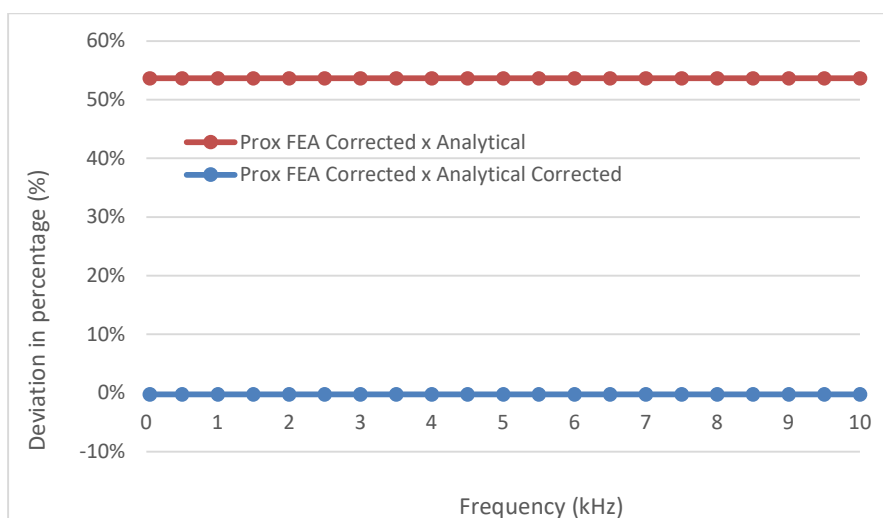


Figure 3.60 - Winding proximity effect losses - FEA Corrected x Analytical Corrected - ACR52.

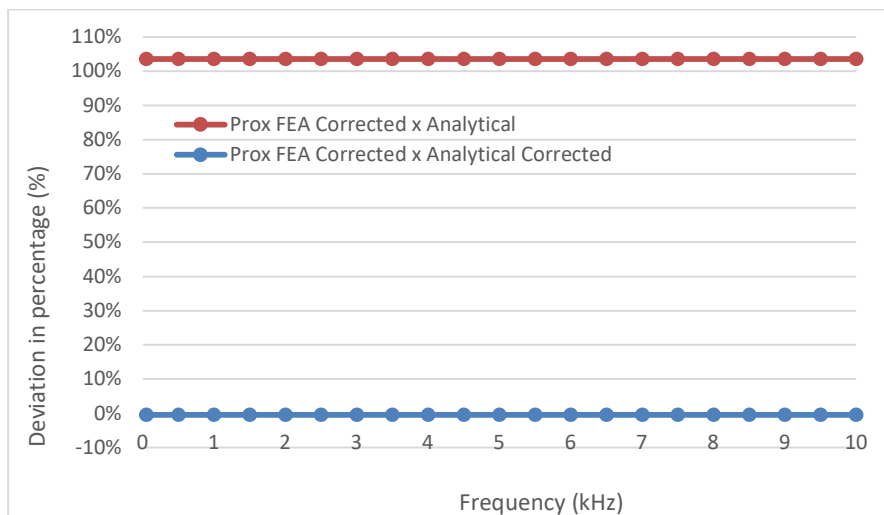


Figure 3.61 - Winding proximity effect losses - FEA Corrected x Analytical Corrected - ACR55.

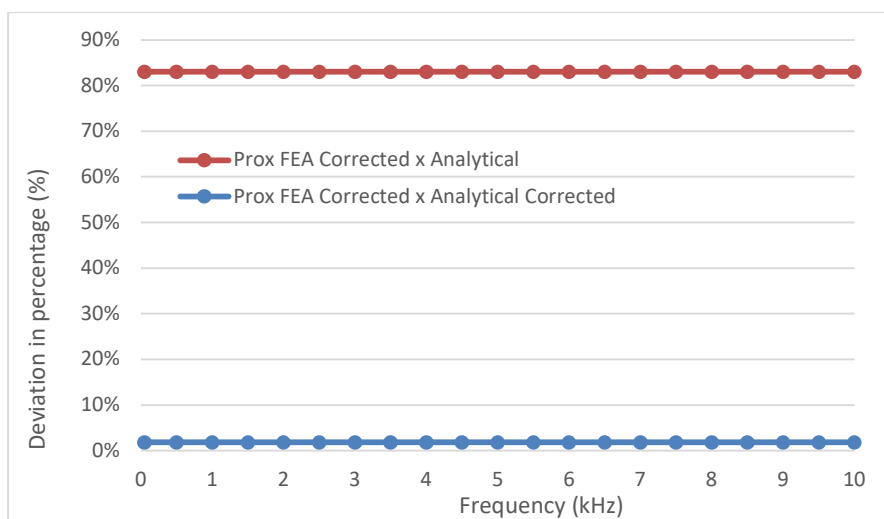


Figure 3.62 - Winding proximity effect losses - FEA Corrected x Analytical Corrected - ACR67.

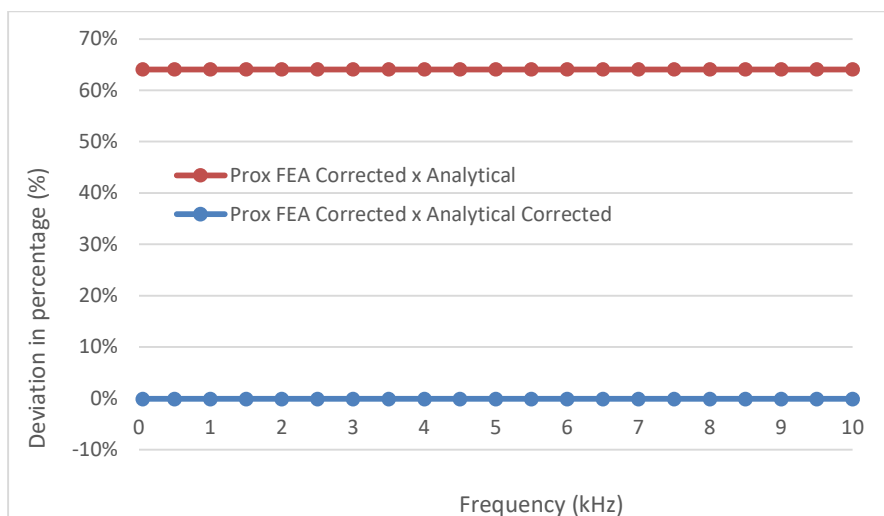


Figure 3.63 - Winding proximity effect losses - FEA Corrected x Analytical Corrected - ACR79.

Bringing back the concept that the losses stemming from the proximity effect have a major impact on the total AC winding power losses when the currents are composed by higher harmonic orders, it would be natural to look over that contribution again now that the correction factors have been applied to the analytical model. The comparison of the models before and after the correction is provided in Fig. 3.64 – 3.72.

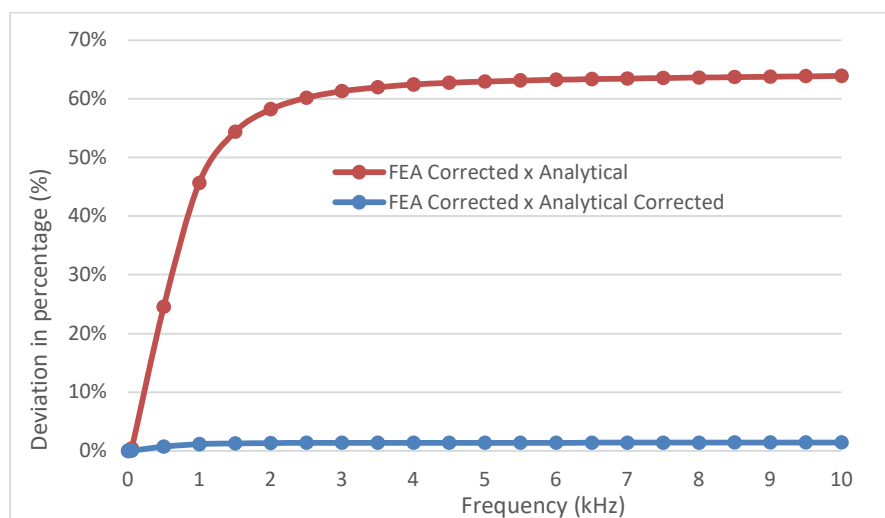


Figure 3.64 - Winding power losses percent deviation before and after correction - ACR1.

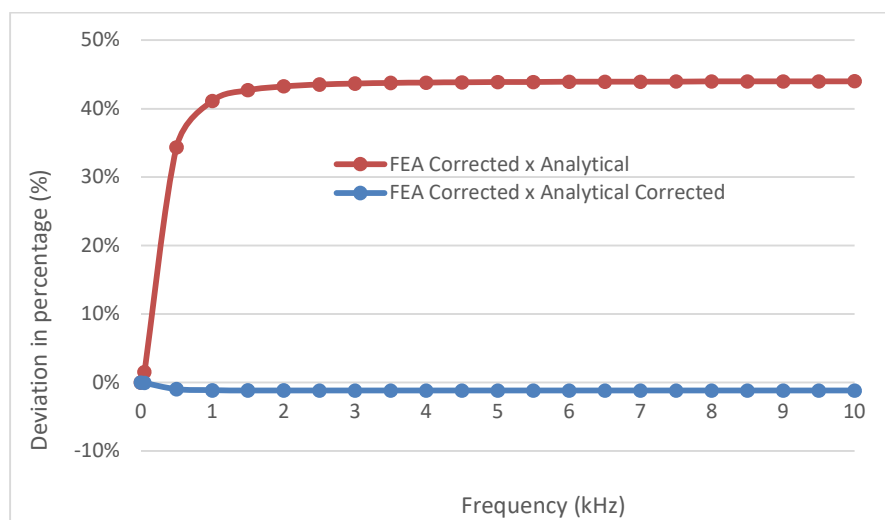


Figure 3.65 - Winding power losses percent deviation before and after correction - ACR13.

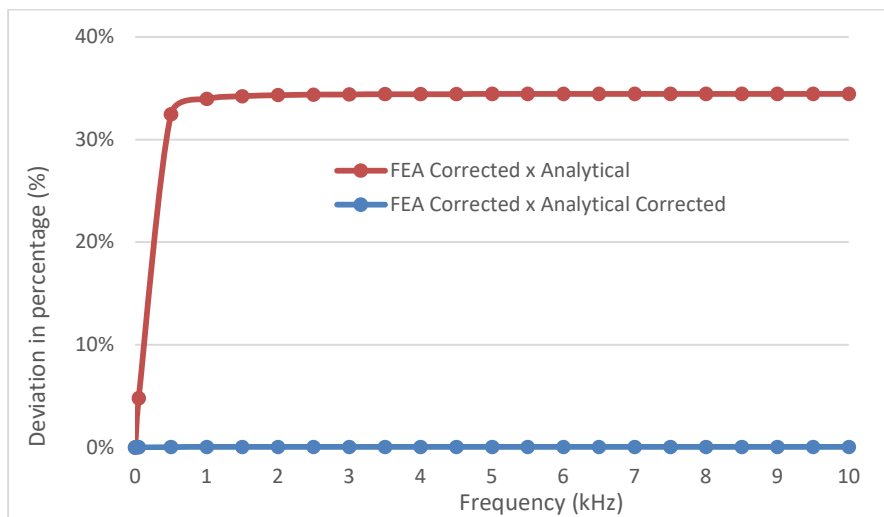


Figure 3.66 - Winding power losses percent deviation before and after correction - ACR25.

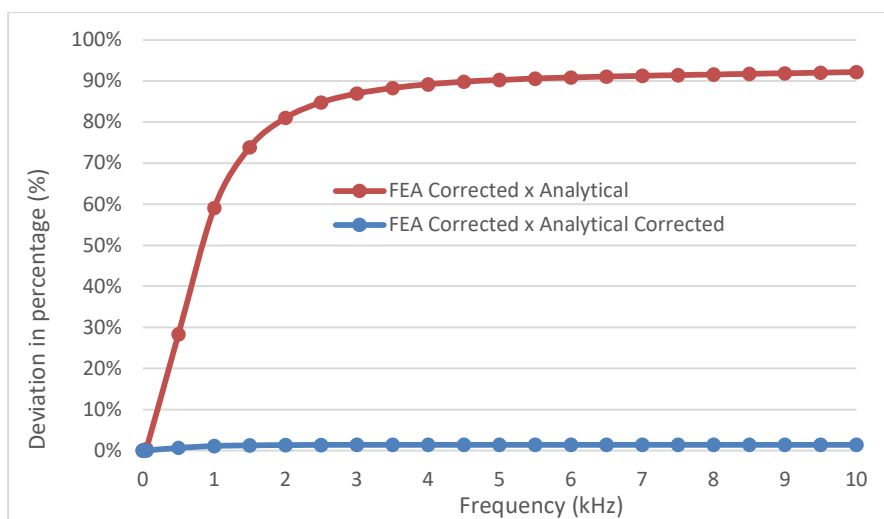


Figure 3.67 - Winding power losses percent deviation before and after correction - ACR28.

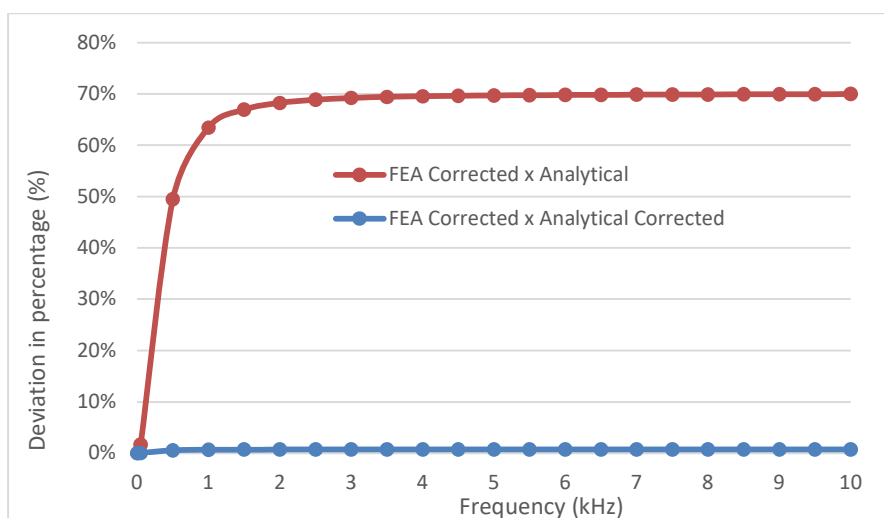


Figure 3.68 - Winding power losses percent deviation before and after correction - ACR40.

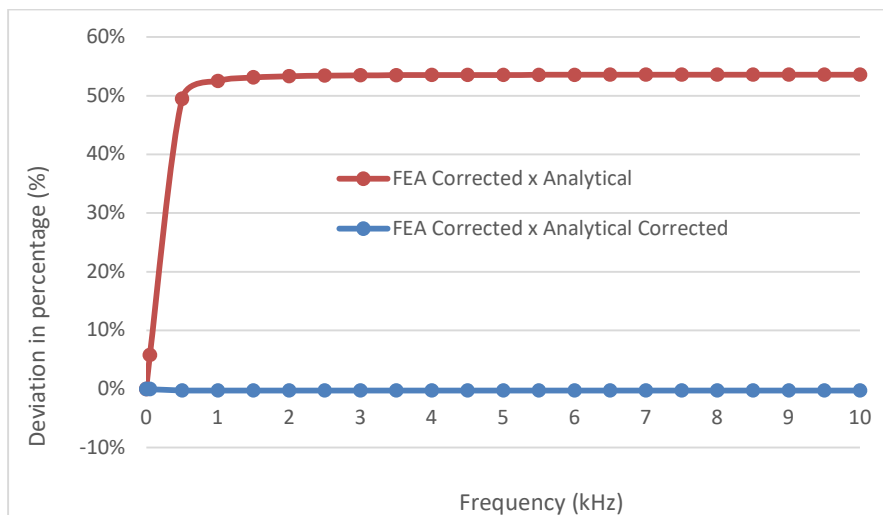


Figure 3.69 - Winding power losses percent deviation before and after correction - ACR52.

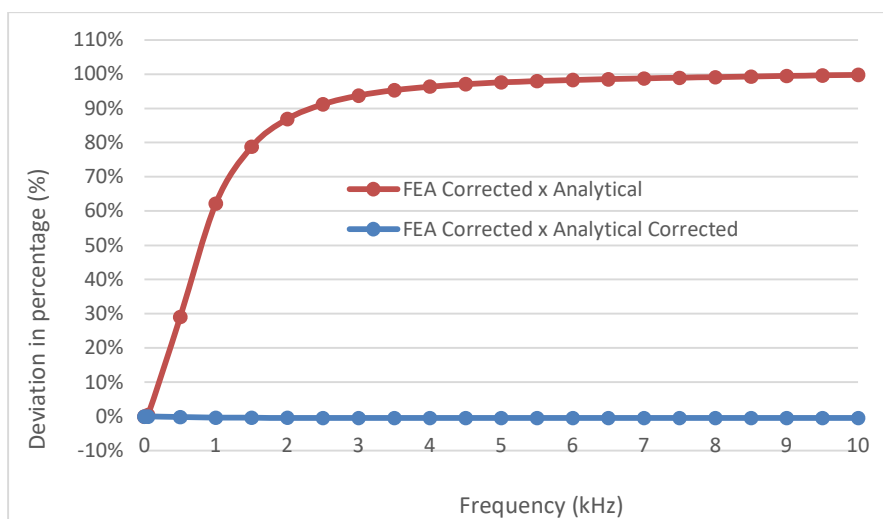


Figure 3.70 - Winding power losses percent deviation before and after correction - ACR55.

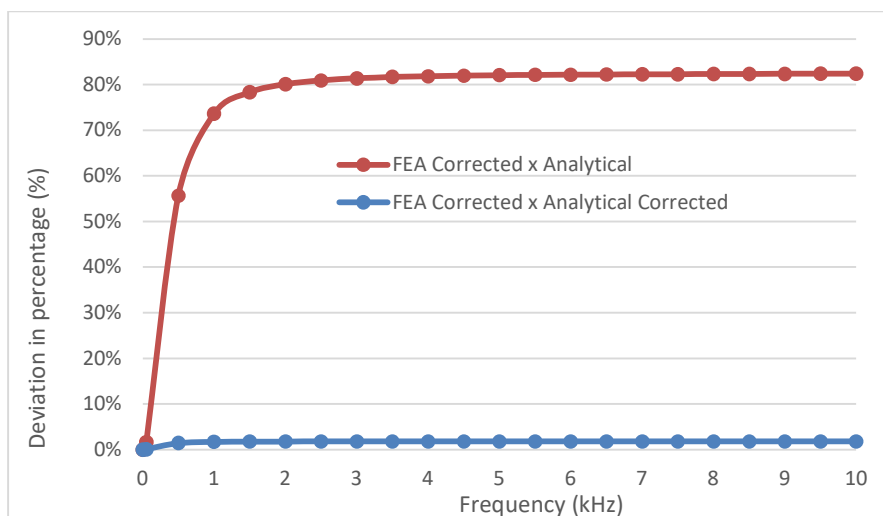


Figure 3.71 - Winding power losses percent deviation before and after correction - ACR67.

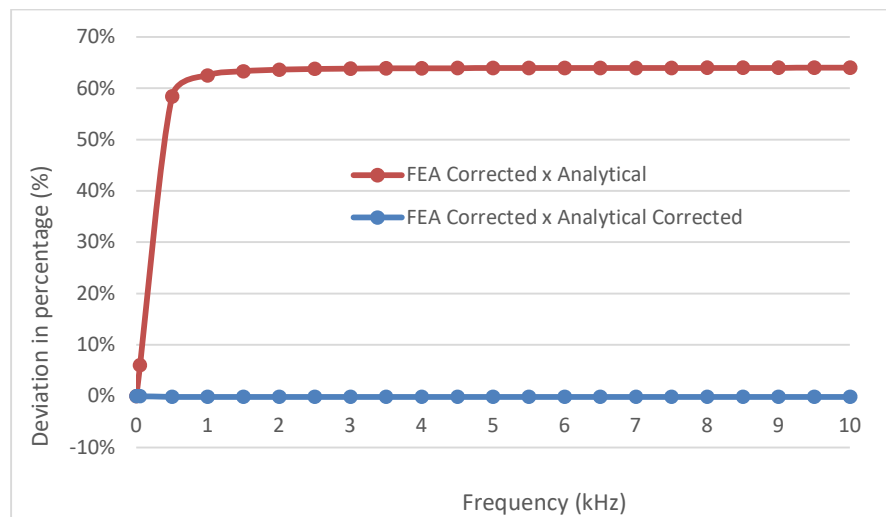


Figure 3.72 - Winding power losses percent deviation before and after correction - ACR79.

The final percent deviations of the 81 experiments for the total winding losses between the FEA corrected and the analytical corrected model, considering the correction factors extracted from the Equation 3.2 are registered in Table 3.6.

Table 3.6 - Total corrected winding power losses percent deviations.

Reference	% Total corrected losses deviation	Reference	% Total corrected losses deviation	Reference	% Total corrected losses deviation
ACR1	1.14	ACR28	1.14	ACR55	-0.37
ACR2	0.62	ACR29	0.67	ACR56	-0.50
ACR3	0.14	ACR30	0.13	ACR57	-0.24
ACR4	0.52	ACR31	0.35	ACR58	-1.62
ACR5	0.60	ACR32	0.56	ACR59	-1.03
ACR6	0.32	ACR33	0.41	ACR60	-0.36
ACR7	-0.58	ACR34	-0.83	ACR61	-3.34
ACR8	0.59	ACR35	0.38	ACR62	-1.85
ACR9	0.85	ACR36	0.75	ACR63	-0.72
ACR10	-1.26	ACR37	-0.05	ACR64	0.98
ACR11	-1.36	ACR38	-0.33	ACR65	0.66
ACR12	-0.70	ACR39	-0.36	ACR66	0.17
ACR13	-1.09	ACR40	0.64	ACR67	1.62
ACR14	-1.26	ACR41	0.10	ACR68	1.13
ACR15	-1.04	ACR42	-0.14	ACR69	0.64
ACR16	-0.57	ACR43	2.31	ACR70	3.05
ACR17	-0.59	ACR44	1.50	ACR71	2.27
ACR18	-0.94	ACR45	0.22	ACR72	0.97
ACR19	0.76	ACR46	-0.90	ACR73	-0.43
ACR20	0.70	ACR47	-0.68	ACR74	-0.12
ACR21	0.56	ACR48	-0.08	ACR75	0.25
ACR22	0.56	ACR49	-0.79	ACR76	-0.42
ACR23	0.66	ACR50	-0.76	ACR77	-0.29
ACR24	0.70	ACR51	-0.25	ACR78	0.24
ACR25	0.05	ACR52	-0.26	ACR79	-0.12
ACR26	0.31	ACR53	-0.74	ACR80	-0.59
ACR27	0.32	ACR54	-1.03	ACR81	-0.77

3.8 Inductance evaluation

Assuming the analytical model presented in this study as the reference for the calculation of the total inductances of windings without magnetic core, another way of verifying the agreement with the FEM calculation is to perform a capability analysis, which consists basically on the comparison of the dataset against predefined spec limits, lower spec limit (LSL) and upper spec limit (USL), that in this case were set to be equal to the accuracy of the inductance calculation method from the analytical model, with a mean target value of zero. This analysis is illustrated in the Fig. 3.73, extracted from *Minitab*. Indeed, the mean value of the dataset was -0.05186 %, which is in line with the observation of the run chart earlier presented. Although the mean value is different from the target of zero, all the experiment values remained within the spec limits. For typical applications of air core reactors in power systems the required inductance tolerance can be $\pm 1\%$ from the rated value, which means that either the analytical model or the FEM would be able to provide reliable results based on that criteria.

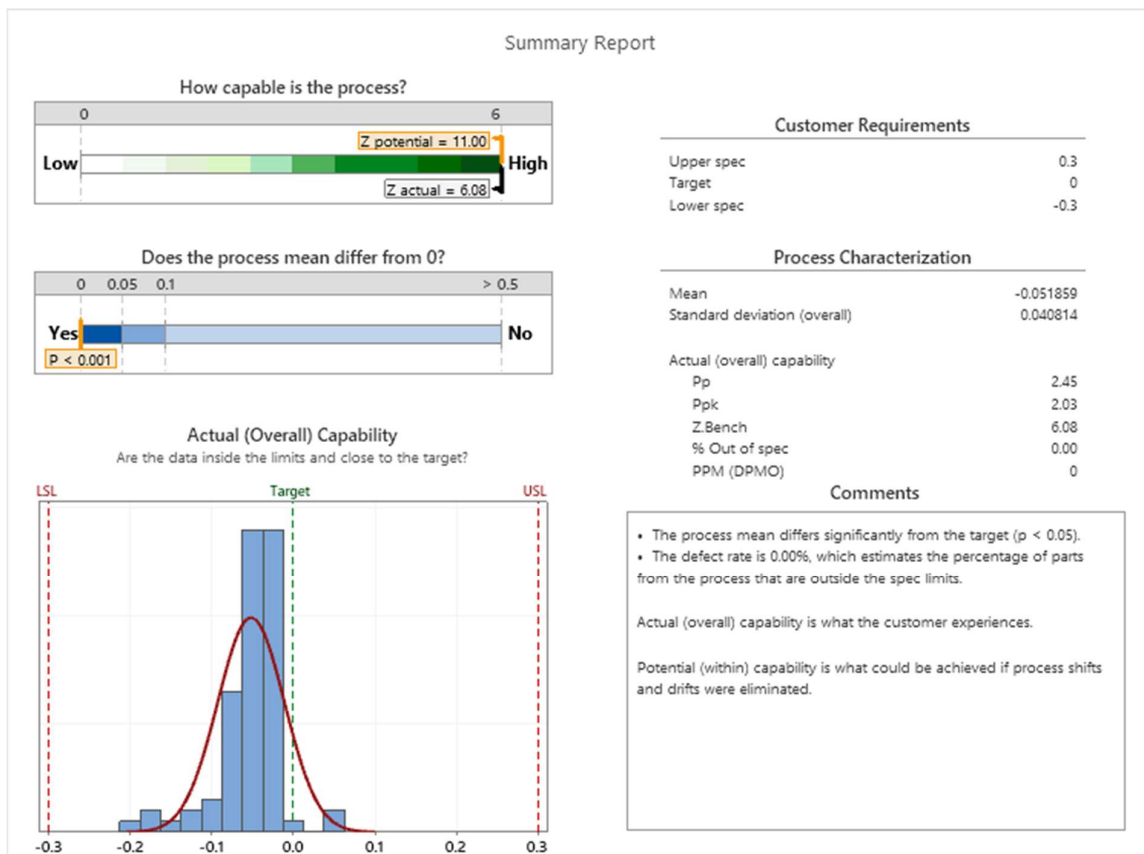


Figure 3.73 - Capability analysis for inductance calculation using FEM.

3.9 Winding power losses evaluation

After the correction of the calculation of the proximity effect winding losses a remaining verification would be a comparison between the capability of the calculation process before and after the changes. This can be done, for example, by using the before and after process capability comparison tool available in *Minitab*. This comparison can be verified in Fig. 3.74.

Before the change the calculation of the total losses carried a high percent deviation for the reasons exposed in this study. Comparing those deviations to a maximum tolerance of $\pm 5\%$, used as LSL and USL, this would mean that 99.12% of the dataset would lie out of the spec limits. The mean value of the process was 44.6%.

After the change, the process presented no values out of the spec limits, with a mean value of 0.015%. This means that the accuracy of the calculation would be sufficient for the mentioned tolerance and for the typical standard requirements for the tolerance for power losses of air core reactors applied in power systems which is about 10%, according to the IEC 60076-6 [36], the IEEE C57.21 [37] and the NBR 5356-6 [38], which are the basic standards for the air core reactors.

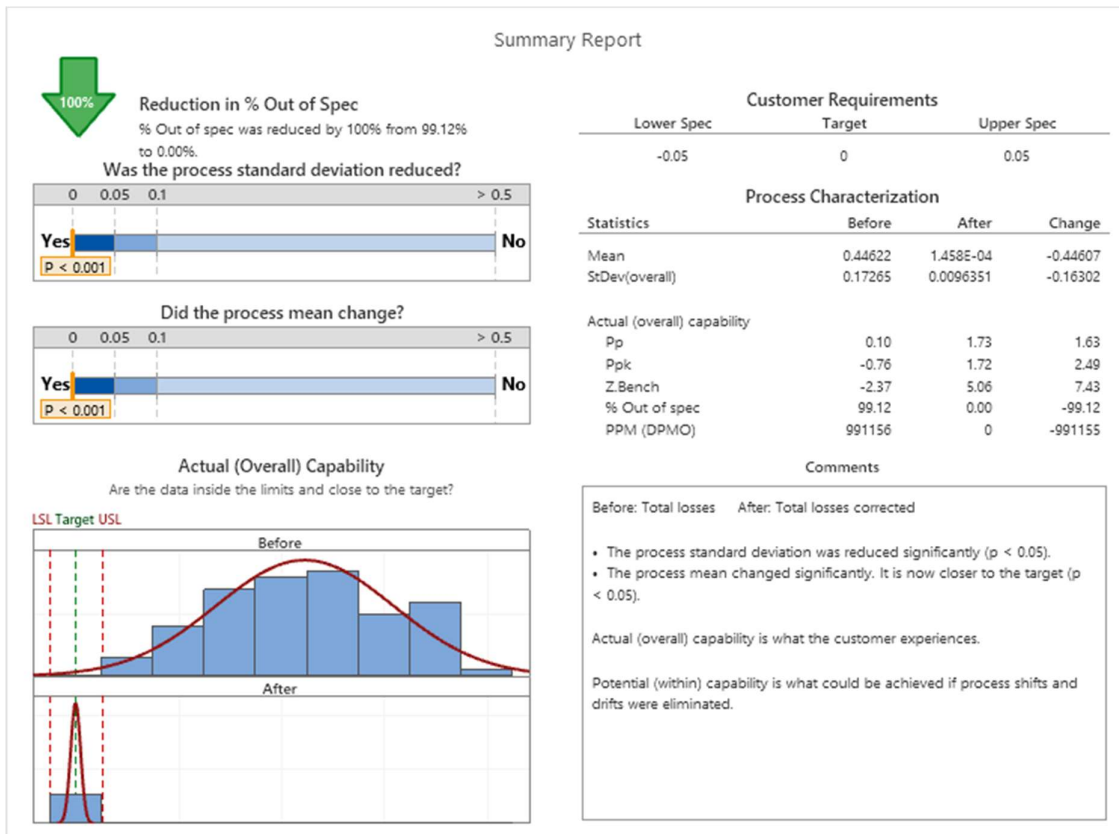


Figure 3.74 - Before/after process capability comparison for winding total losses.

4. CONCLUSIONS

The use of the software based on finite element models was explored in this study to simulate the winding design characteristics of the air core reactors, inductance and power losses, aiming to create a solid basis which would allow for future developments in the area.

Due to the challenges faced when using a strand-by-strand simulation, being either related to drawing the geometries properly and assigning the right boundary conditions, or even the fact that most of the common computers would not be able to handle huge simulations with complex geometries, a finite element model using a 2-D equivalent geometry approach is proposed and verified throughout the comparison of the total inductance values (which is the ACRs' most important design characteristic) provided by this model and the analytical model that carries very accurate formulation, used in the industry as the basic calculation for some decades. An excellent agreement between the models was obtained in terms of inductance calculation.

When performing the complete simulation of the windings, aiming to obtain the values of the total winding power losses it was noticed that it would be necessary to add some corrections in the FEM, as the 2-D equivalent geometry was not presenting proper results for the DC winding losses. It was also evidenced that the imbedded calculation model of the FEM software for the total AC power losses would have some constraints depending on the ratio between the magnetic field penetration and the radius of the strands. Both points were improved by adding the formulae of the analytical model to the FEM. By doing that, the results were more consistent as the remaining difference between the models would be only the magnetic field distribution along the geometry of the windings (internal and external).

A statistical approach was considered to the design of 81 experiments in a way to represent a large range of the design parameters, where it would be expected that the corrections proposed by running a few experiments would be representative of the total range.

Along the process, the calculation of the proximity effect losses was confirmed as the main responsible for the discrepancies between the models and the proposition of the study was to cover for that effect by adding correction factors stemming from the equation of the response surface drawn over the dataset related to those discrepancies.

The fitting of the response surface was excellent, leading to a reduction of the percent deviations of the total losses from an average of 45 % to 0.01 % after the corrections are made.

5. FUTURE WORKS

In this work the ACRs composed by only one winding were studied. A reasonable and important future work would be extrapolating such a study to equipment with multi-cylinders as they are the most common design found for the application that equipment in power systems.

In the construction of the ACR there are not only the windings but other metallic structures that were not part of the present study. To further explore the good results of the 2-D equivalent geometry approach a future work would be considering the equivalent geometry in a 3-D simulation with FEM so any other metallic structure can be added and have their induced power losses evaluated. This would reduce considerably the simulation time as meshing of the windings would be smaller compared to the complete simulation.

Another possible work is to use the approach mentioned above to simulate other phenomenon like temperature distribution in the windings and in the additional structures surrounding the reactors, like fences, cables, and busbars. In software based in FEM, bulk thermal conductivity can be assigned to materials to represent the thermal conductivity of the equivalent system (conductor and insulation) so thermal conduction, convection and radiation can be properly simulated, being an important tool for the development of the thermal calculation models for the ACRs.

A third possible work also takes benefit of the 3-D equivalent geometry to explore the audible noise simulation of the ACRs. As the inductance and the power losses of the ACRs simulated with the FEM had a good agreement with the analytical calculations, it is expected that both magnetic field and current distributions are alike and so would be the Lorentz forces that ultimately will generate the main component of the ACRs audible noise. Such a study would be important to the enhancement of noise calculation models as well as to develop noise mitigating solutions, like acoustic chambers.

Last but not least, the understanding that the calculation method has a good agreement with another software or methodology enhances its reliability and sets the basis for further developments on manufacturing process, as the probability of occurrence of a deviation caused by a mistake on the calculation method is reduced.

6. BIBLIOGRAPHY

- [1] Alstom Grid, "Power Transformers - Fundamentals," 2012.
- [2] GE Grid Solutions, "Air Core Reactors," [Online].
Available: <https://www.gegridsolutions.com/app/resources.aspx?prod=ACR&type=1>
- [3] Trench Group, "High Voltage Reactors," [Online].
Available: <https://www.trench-group.com/coils/>
- [4] Coil Innovation, "Air-Core Dry-Type Reactors," [Online].
Available: <https://www.coilinnovation.com/products/?lang=en>
- [5] J. Lammeraner and M. Stafl, "Eddy Currents," London: Hiffe Books, 1966.
- [6] P. L. Dowell, "Effects of eddy currents in transformer windings," Proceedings of the IEE, vol. 113, no. 8, pp. 1387–1394, Aug. 1966.
- [7] R. L. Stoll, "The analysis of eddy currents," Oxford: Clarendon Press, 1974.
- [8] A. M. Urling, V. A. Niemela, G. R. Skutt, and T. G. Wilson, "Characterizing high-frequency effects in transformer windings-A guide to several significant articles," in Proc. APEC'89, pp. 373–385, Mar. 1989.
- [9] J. A. Ferreira, "Improved analytical modeling of conductive losses in magnetic components," in IEEE Transactions on Power Electronics, vol. 9, no. 1, pp. 127-131, Jan. 1994, doi: 10.1109/63.285503.
- [10] J. A. Ferreira, "Analytical computation of ac resistance of round and rectangular litz wire windings," IEE Proceedings-B Electric Power Applications, vol.139, No1, pp. 21–25,1992.
- [11] J. A. Ferreira, "Electromagnetic modeling of power electronic converters," Norwell, MA: Kluwer, 1989.
- [12] General Electric Company, "Lean Six Sigma - Book of Knowledge," ver. 5.4, Brazil, 2019.
- [13] J. C. Maxwell, "A Treatise on Electricity and Magnetism," 2nd edition, vol. I-II, London: Clarendon Press, 1881.
- [14] L. Cohen, "An exact formula for the mutual inductance of coaxial solenoids," Bulletin of Bureau of Standards, Vol. 3, No. 2, pp. 295-303, 1907.
- [15] G. R. Olshausen, "Note on absolute formulae for the mutual inductance of coaxial solenoids," Phys. Rev., Vol. 35, p. 150, 1912.
- [16] E. B. Rosa and F. W. Grover, "Formulas and tables for the calculations of mutual and self-inductance," Sci. Papers Bur. Stand., No. 169, 1916.
- [17] H. A. Wheeler, "Simple Inductance Formulas for Radio Coils," Proc. IRE, vol. 16, pp. 1398-1400, 1928.
- [18] F. W. Grover, "Tables for calculation of the mutual inductance of any two coaxial single layer coils", Proc. IRE, Vol. 21, No. 7, pp. 1039-1049, 1933.
- [19] K. Foelsch, "Magnetfeld und Induktivität einer zylindrischen Spule", Archiv für Elektrotechnik, XXX Band, 1936.
- [20] H. B. Dwight, "Electrical Coils and Conductors – Their Electrical Characteristics and Theory," 1st edition, New York, McGraw Hill, 1945.
- [21] F. W. Grover, "Inductance Calculations – Working Formulas and Tables," 1st edition, New York, Dover Publications, 1946.
- [22] T. H. Fawzi and P. E. Burke, "The Accurate Computation of Self and Mutual Inductances of Circular Coils," in IEEE Transactions on Power Apparatus and Systems, vol. PAS-97, no. 2, pp. 464-468, March 1978, doi: 10.1109/TPAS.1978.354506.
- [23] S. J. Salon, "Finite element analysis of electrical machines," 1st edition, New York, Springer Science, 1995.
- [24] Ansys® Maxwell, Release 20.1, help system, ANSYS, Inc, Canonsburg, 2020.
- [25] M. A. Horace Lamb, "On Electrical Motions in a Spherical Conductor," London, Philosophical Transactions of the Royal Society of London, Vol. 174, pp 519-549, 1883.

- [26] M. Abramowitz and I. A. Stegun, "Handbook of Mathematical Functions," New York: Dover Publications, 1970.
- [27] M. P. Perry, "Multiple Layer Series Connected Winding Design for Minimum Losses," in IEEE Transactions on Power Apparatus and Systems, vol. PAS-98, no. 1, pp. 116-123, Jan. 1979, doi: 10.1109/TPAS.1979.319520.
- [28] P. E. Burke and T. H. Fawzi, "Effect of eddy losses on the design and modelling of air-cored reactors," in IEEE Transactions on Magnetics, vol. 27, no. 6, pp. 5001-5003, Nov. 1991, doi: 10.1109/20.278720.
- [29] C. R. Sullivan, "Computationally efficient winding loss calculation with multiple windings, arbitrary waveforms, and two-dimensional or three-dimensional field geometry," in IEEE Transactions on Power Electronics, vol. 16, no. 1, pp. 142-150, Jan. 2001, doi: 10.1109/63.903999.
- [30] X. Nan and C. R. Sullivan, "An improved calculation of proximity-effect loss in high-frequency windings of round conductors," IEEE 34th Annual Conference on Power Electronics Specialist, 2003. PESC '03., 2003, pp. 853-860 vol.2, doi: 10.1109/PESC.2003.1218168.
- [31] X. Nan and C. R. Sullivan, "Simplified high-accuracy calculation of eddy-current loss in round-wire windings," 2004 IEEE 35th Annual Power Electronics Specialists Conference (IEEE Cat. No.04CH37551), 2004, pp. 873-879 Vol.2, doi: 10.1109/PESC.2004.1355533.
- [32] J. Acero, R. Alonso, J. M. Burdio, L. A. Barragan and C. Carretero, "A model of losses in twisted-multistranded wires for planar windings used in domestic induction heating appliances," APEC 07 - Twenty-Second Annual IEEE Applied Power Electronics Conference and Exposition, 2007, pp. 1247-1253, doi: 10.1109/APEX.2007.357674.
- [33] A. Roßkopf, E. Bär and C. Joffe, "Influence of Inner Skin- and Proximity Effects on Conduction in Litz Wires," in IEEE Transactions on Power Electronics, vol. 29, no. 10, pp. 5454-5461, Oct. 2014, doi: 10.1109/TPEL.2013.2293847.
- [34] J. Islam, "Finite-Element Analysis of Eddy Currents in the Form-Wound Multi-Conductor Windings of Electrical Machines," TKK Dissertation 211, Espoo 2010, Available: <https://aaltodoc.aalto.fi/handle/123456789/4734>
- [35] General Electric Company, "Design for Six Sigma - DMADOV Book of Knowledge," ver. 3.0, New York, 2007.
- [36] International Electrotechnical Commission, "IEC 60076-6 Power Transformers - Part 6: Reactors," IEC, Geneva, Switzerland, 2007.
- [37] IEEE, "IEEE Std C57.21 Standard Requirements, Terminology, and Test Code for Shunt Reactors Rated Over 500kVA," IEEE, New York, NY, 2008.
- [38] ABNT, "NBR 5356-6 Transformadores de Potência Parte 6: Reatores," Brazil, 2014.